

Argonne National Laboratory

REACTOR DEVELOPMENT PROGRAM PROGRESS REPORT

December 1969

The facilities of Argonne National Laboratory are owned by the United States Government. Under the terms of a contract (W-31-109-Eng-38) between the U. S. Atomic Energy Commission, Argonne Universities Association and The University of Chicago, the University employs the staff and operates the Laboratory in accordance with policies and programs formulated, approved and reviewed by the Association.

MEMBERS OF ARGONNE UNIVERSITIES ASSOCIATION

The University of Arizona
Carnegie-Mellon University
Case Western Reserve University
The University of Chicago
University of Cincinnati
Illinois Institute of Technology
University of Illinois
Indiana University
Iowa State University
The University of Iowa

Kansas State University
The University of Kansas
Loyola University
Marquette University
Michigan State University
The University of Michigan
University of Minnesota
University of Missouri
Northwestern University
University of Notre Dame

The Ohio State University
Ohio University
The Pennsylvania State University
Purdue University
Saint Louis University
Southern Illinois University
University of Texas
Washington University
Wayne State University
The University of Wisconsin

LEGAL NOTICE

This report was prepared as an account of Government sponsored work. Neither the United States, nor the Commission, nor any person acting on behalf of the Commission:

A. Makes any warranty or representation, expressed or implied, with respect to the accuracy, completeness, or usefulness of the information contained in this report, or that the use of any information, apparatus, method, or process disclosed in this report may not infringe privately owned rights; or

B. Assumes any liabilities with respect to the use of, or for damages resulting from the use of any information, apparatus, method, or process disclosed in this report.

As used in the above, "person acting on behalf of the Commission" includes any employee or contractor of the Commission, or employee of such contractor, to the extent that such employee or contractor of the Commission, or employee of such contractor prepares, disseminates, or provides access to, any information pursuant to his employment or contract with the Commission, or his employment with such contractor.

Printed in the United States of America
Available from

Clearinghouse for Federal Scientific and Technical Information
National Bureau of Standards, U. S. Department of Commerce
Springfield, Virginia, 22151

Price: Printed Copy \$3.00; Microfiche \$0.65

ARGONNE NATIONAL LABORATORY
9700 South Cass Avenue
Argonne, Illinois 60439

REACTOR DEVELOPMENT PROGRAM
PROGRESS REPORT

December 1969

Robert B. Duffield, Laboratory Director
Stephen Lawroski, Associate Laboratory Director

<u>Division</u>	<u>Director</u>
Chemical Engineering	R. C. Vogel
EBR-II Project	M. Levenson
Metallurgy	P. G. Shewmon
Reactor Engineering	L. J. Koch
Reactor Physics	R. Avery

Report coordinated by
A. Glassner and A. D. Rossin

Issued January 29, 1970

FOREWORD

The Reactor Development Program Progress Report, issued monthly, is intended to be a means of reporting those items of significant technical progress which have occurred in both the specific reactor projects and the general engineering research and development programs. The report is organized in accordance with budget activities in a way which, it is hoped, gives the clearest, most logical overall view of progress. Since the intent is to report only items of significant progress, not all activities are reported each month. In order to issue this report as soon as possible after the end of the month editorial work must necessarily be limited. Also, since this is an informal progress report, the results and data presented should be understood to be preliminary and subject to change unless otherwise stated.

The issuance of these reports is not intended to constitute publication in any sense of the word. Final results either will be submitted for publication in regular professional journals or will be published in the form of ANL topical reports.

The last six reports issued
in this series are:

June 1969	ANL-7581
July 1969	ANL-7595
August 1969	ANL-7606
September 1969	ANL-7618
October 1969	ANL-7632
November 1969	ANL-7640

REACTOR DEVELOPMENT PROGRAM

Highlights of Project Activities for December 1969

EBR-II

Operation of the reactor at 50 MWt, was resumed in mid-December. The reactor had been shut down since October 16 for scheduled maintenance, for installation of the instrumented subassembly, and for reactor modifications. The fueled Test-2 Instrumented Subassembly is in the reactor and is operating satisfactorily. Between startup and December 20 the reactor was operated for 170 MWd, bringing its cumulative operational total to 30,210 MWd.

The maximum allowable burnup limit of low-swelling (high-silicon) EBR-II driver fuel was increased from 1.5 to 1.8 at. %. Earlier in 1969 the limit had been increased from 1.2 to 1.5 at. %.

The air cell of the Fuel Cycle Facility was closed up and returned to normal operation on December 9. All work in the cell, including direct cleanup, was completed in 30 working days.

ZPR-3

The series of characterizing experiments in the uranium-reflected Assembly 58 has been completed, and the reflector has been changed to lead for Assembly 59. The core radius was simultaneously reduced to 23.83 cm, and the critical loading was reduced to 76 kg fissile plutonium.

Reactivity effects due to the decay of Pu-241 in Assemblies 51 and 56B have been studied and accounted for; however, since these effects cannot always be isolated from concurrent temperature effects, it is believed that reference cores should be repeated periodically when experiments are made over an extended period of time.

ZPR-6

Experimental work with Assembly 6A continues. Proton-recoil determination of neutron spectra at core center with and without sodium in the central region has been completed. Doppler-effect measurements of natural UO_2 in the central, sodium-free region have been made, and several types of reaction rate studies carried out at various locations in the core.

ZPR-9

Approval to operate ZPR-6 and -9 with plutonium-fueled cores has been received, and for the first time plutonium in amounts greater than

1 kg was loaded into ZPR-9 on December 11, 1969. The core (Assembly 26) had been preloaded with FTR-3 core materials to the extent possible, and the first plutonium fuel cans were loaded into ten dual-purpose control-rod drawers. The approach to critical is continuing with the core now loaded to more than 30% of the estimated critical mass.

ZPPR

Radial variations in reaction rates of B-10 capture, U-238 fission, and Pu-239 fission were measured at three axial elevations in the ZPPR/FTR-2 assembly in its shield configuration and the data compared with computations using neutron fluxes obtained from a DIFF2D solution. Central fission ratios were made comparing the fission cross sections of six uranium and plutonium isotopes to that of U-235. With the ZPPR/FTR-2 program completed the facility is now being readied for the first demonstration reactor benchmark experiment.

TABLE OF CONTENTS

	<u>Page</u>
I. LIQUID METAL FAST BREEDER REACTORS--CIVILIAN	1
A. Physics Development--LMFBR	1
1. Theoretical Reactor Physics	1
2. Experimental Reactor Physics	4
3. ZPR-6 and -9 Operations and Analysis	9
4. ZPR-3 and ZPPR Operations and Analysis	13
B. Component Development--LMFBR	43
1. Instrumentation and Control	43
2. Fuel Handling, Vessels and Internals	48
C. Sodium Technology	49
1. Sodium Chemistry	49
2. Sodium Analytical Development	49
3. On-line Monitors	51
4. Materials Compatibility	53
D. EBR-II--Research and Development	54
1. Equipment--Fuel Related	54
2. New Subassemblies and Experimental Support	54
3. Instrumented Subassemblies	57
4. Coolant Chemistry	59
5. Experimental Irradiation and Testing	62
6. Materials-Coolant Compatibility	62
7. Systems Engineering	65
8. Reactor Analysis, Testing and Methods Development	66
9. Driver Fuel Development	76
E. EBR-II--Fuel Fabrication	78
1. Cold Line Operations	78
F. EBR-II--Operations	79
1. Reactor Plant	79
2. Fuel Cycle Facility	80
PUBLICATIONS	82

TABLE OF CONTENTS

	<u>Page</u>
II. OTHER FAST REACTORS--OTHER FAST BREEDER REACTORS--FUEL DEVELOPMENT	87
A. Irradiation Effects, Mechanical Properties and Fabrication	87
1. Mechanical Properties of Cladding Materials	87
2. Void-formation Modeling	87
PUBLICATION	89
III. GENERAL REACTOR TECHNOLOGY	90
A. Applied and Reactor Physics Development	90
1. Theoretical Reactor Physics--Research and Development	90
2. Nuclear Data--Research and Development	97
B. Reactor Fuels and Materials Development	101
1. Fuels and Claddings--Research and Development	101
2. Techniques of Fabrication and Testing--Research and Development	104
C. Engineering Development--Research and Development	108
1. Instrumentation and Control	108
2. Heat Transfer and Fluid Flow	110
3. Engineering Mechanics	115
D. Chemistry and Chemical Separations	115
1. Fuel Cycle Technology--Research and Development	115
2. General Chemistry and Chemical Engineering--Research and Development	120
PUBLICATIONS	124
IV. NUCLEAR SAFETY RESEARCH AND DEVELOPMENT	128
A. LMFBR Safety--Research and Development	128
1. Accident Analysis and Safety Evaluation	128
2. Coolant Dynamics	128
3. Fuel Meltdown Studies with TREAT	131

TABLE OF CONTENTS

	<u>Page</u>
4. Materials Behavior and Energy Transfer	134
5. Violent Boiling	135
B. Effluent Control--Environmental Studies--Research and Development	136
1. Thermal-Plume Transport in the Great Lakes	136
PUBLICATIONS	138

I. LIQUID METAL FAST BREEDER REACTORS--CIVILIAN

A. Physics Development--LMFBR

1. Theoretical Reactor Physics

a. General Reactor Physics

(i) Reactor Dynamics (D. A. Meneley)

Last Reported: ANL-7632, pp. 1-2 (Oct 1969).

(a) QX1--Group-structure Studies. The example of coolant voiding (see ANL-7632) provides a convenient basis for illustrating some of the effects of group structure on calculated transient behavior, because both the voiding that initiates the transient and the Doppler feedback are very sensitive to the spectrum. As an illustration of the effects of various collapsed-group structures on calculated parameters, four different nine-group sets have been prepared from the 26-group microscopic cross section library which was used to calculate the sodium-voiding case in ANL-7632. One six-group set was also prepared for comparison. The group boundaries of four of the five collapsed sets are shown in Fig. I.A.1 relative to the

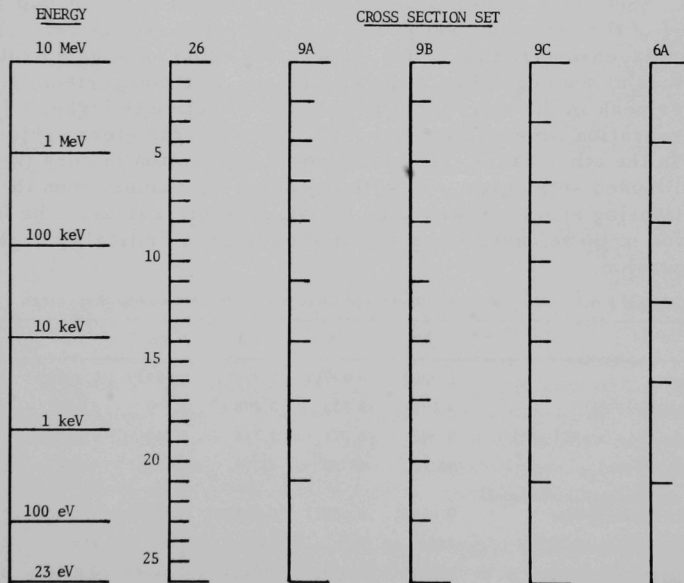


Fig. I.A.1. Group Boundaries of the 26-group Microscopic Cross-section Library and of Four Collapsed Sets Prepared from It

26-group structure. (Exact energies at these boundaries may be obtained by reference to the equal half-lethargy width of the 26-group set, with zero lethargy at 10 MeV.) A variant of Set 9C, labelled 9D, was produced by moving the boundary between group 1 and group 2 of 9C down one-half lethargy unit.

The single flux spectrum which was used to collapse the microscopic cross sections was the centerline spectrum from the initial steady state in the 26-group problem. Standard linear flux weighting was used for all cross sections with the exception of the transport cross section.* The microscopic collapsed-group values in this case were obtained by means of Travelli's Eq. 42.* This prescription requires a set of macroscopic transport cross sections; these were taken from the composition at the centerline of the 26-group problem, as were the fluxes.

Complete sets of collapsed microscopic cross sections were produced by this procedure; then the QX1 code was rerun with each of the sets, using virtually the same problem specifications as in ANL-7632. (The emission spectrum of delayed neutrons was altered slightly relative to that case.) Some parameters which were obtained from the runs using the various collapsed-group sets are shown in Table I.A.1. The column labels identify the various sets relative to the group structures given in Fig. I.A.1. (Set 9D is identical to 9C with the exception that group 1 includes groups 1-4 of the reference set and group 2 includes groups 5-6.) The effective delayed-neutron fractions, generation times, and ramp rates are initial values at the beginning of the excursion. For comparison, at the first power peak in the reference case, the β -effective is higher by 0.5% and the generation time was lower by 2%. These parameters exhibit similar behavior in the other cases. The relative multiplication factors (k -effective) for the collapsed sets agree well with the 26-group values, even though a single collapsing spectrum was used for all reactor regions. The initial composition in these cases were adjusted to achieve criticality at the start of the excursion.

TABLE I.A.1. Results for Coolant-void Case with Different Group Structures

	26	9A	9B	9C	9D	6A
k -effective	1.0000	0.99961	0.99983	0.99949	0.99957	0.99956
β -effective ($\times 10^{-3}$)	3.291	3.333	3.408	3.399	3.329	3.400
Generation time ($\times 10^{-7}$ sec)	4.308	4.274	4.315	4.249	4.240	4.324
Ramp rate (\$/sec)	41.74	41.50	42.69	49.39	42.14	38.72
Doppler coefficient (isothermal) -T(dk/dT)(1300-1800°K)	0.00861	0.00811	0.00825	0.00808	0.00808	0.00804
Power rise to first peak ^a	226	245	257	333	255	232
Time of first peak (sec)	0.0295	0.0297	0.0290	0.0254	0.0293	0.0317

^aRatio of power at first peak to initial power.

*Travelli, A., in Reactor Physics Division Annual Report, July 1, 1967 to June 30, 1968, Paper VI-5, pp. 413-421; see especially equations 7, 9, 10, and 11.

Set 9A, which has several groups concentrated toward the higher energy end, predicts the initial ramp rate rather well but underestimates the Doppler coefficient; the first power peak is overestimated by 8% at 2 ms later than the reference. Set 9B is quite evenly distributed in the original group structure, as is 6A. These two sets show little or no advantage over 9A (excepting, of course, the economy advantage of 6A). Set 9C is particularly poor, even though its group structure is not markedly different than that of 9A. The results using 9D illustrate the main reason for this. Set 9C does not have a group boundary near the U-238 fission threshold, so does not predict the sodium void worth very well. Set 9D, on the other hand, has a group boundary at 1.35 MeV. This gives a better prediction of sodium worth and therefore of the power trace.

The only conclusion of this very limited study, namely, that there should be a group boundary at the U-238 fission threshold, has been known for many years. From the beginning of fast reactor analysis, much attention has been given to appropriate procedures for cross-section weighting and the selection of group structures. The requirements of a "good" group structure for prediction of static reactivity coefficients, such as control worth, coolant-void worth, and resonance-absorption changes, are identical to the requirements for dynamic analysis. All of the considerable experience which has been accumulated in the statics area can be applied to dynamics. Simple spatial kinetics calculations such as those described above can, however, provide direct indication of the adequacy of a given collapse set. Various insertions and feedback functions which are expected to be encountered in the actual dynamics studies can be run in simplified problems to test a given collapsed set. A group-collapsing routine has been inserted as a subroutine of the QX1 code in order to facilitate this process.

(b) Two-dimensional Kinetics Development. Efforts to determine the interfaces between the two-dimensional kinetics module and the SAS1B system have been completed for heat-transfer calculations. The heat-transfer routines in SAS1B will supply temperatures and material compositions for each heat-transfer node to a mesh overlay system. The system allows the heat-transfer and coolant-dynamics routines to use more than one channel at the same radial location to represent different refueling batches in the same ring of subassemblies. Since material regions can overlap or coincide, the mesh overlay system will accumulate material densities in a particular neutronics cell, with the final result being a set of mesh-dependent atom densities and fuel temperatures.

The heat-transfer mesh cells tend to be larger than the neutronics mesh cells; consequently, there is a set of neutronics cells that is completely interior to a heat-transfer region. All "interior" cells have the same isotope densities, and consequently some computing-speed advantage can be gained by designing the interpolation routine to proceed over these groups of "interior" cells rather than interval by interval.

In places where the heat-transfer regions overlap, the mesh overlay system will average the temperatures to obtain a suitable average temperature for each neutronics cell.

When the neutronics module is called by the heat-transfer routines, the spatial average of the neutron flux will be returned for each energy group for each heat-transfer node. In addition, the average power, the maximum power, and the minimum power in each heat transfer node will be returned.

2. Experimental Reactor Physics

a. Fast Critical Experiments--Experimental Support--Illinois

(i) Neutron Spectrum Measurements (E. F. Bennett and R. C. Doerner)

Last Reported: ANL-7595, pp. 12-14 (July 1969).

(a) Response Functions Associated with Proportional Counter Fields. The observation that only a very slight "bowing" of field lines occurs in an ordinary coaxial cylinder proportional counter design (see ANL-7595) permits a relatively direct method of converting the observed variation of the axial field at the anode to a distribution in pulse amplitude where the initial ionization is of point extension and is uniformly distributed.

By an initial calibration, made with a source of known ionization, one can relate gas gain A to voltage V . The location of the peak of the calibration distribution is not, in effect, very sensitive to the end-associated distortion.

For example, in Fig. I.A.2 is shown a pulse-height distribution from ^{37}A betas (of 3-keV energy) in the test counter. The location of the peak, in spite of the large statistical broadening and the low energy tail (due partly to field effects), is not difficult to ascertain.

Gas multiplication occurs only in the immediate vicinity of the anode in proportional counters. If the electric-field variation along the anode is known and if a calibration relating gas multiplication to voltage is also available, it is an easy matter to derive a response function for the counter at any particular voltage. This is done by replacing the calibration voltage with the calculated anode field (a function of axial distance z) normalized such that for large z the function equals V . The resulting expression then relates gas multiplication to axial distance.

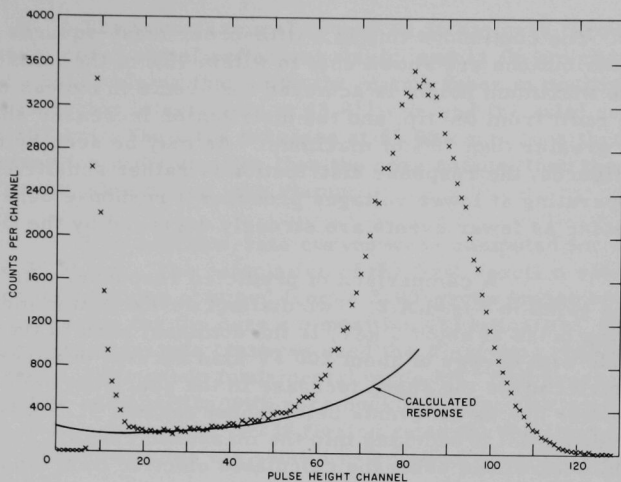


Fig. I.A.2. Pulse Amplitude Distribution for ^{37}A β Particles

The density of events (per cm of anode) will be uniform across the whole anode region where field bowing is insignificant. In order to derive an amplitude distribution of events, one only has to transform from the (constant) density per unit anode length to the corresponding density per unit multiplication. The actual prescription for expressing A versus V is plainly irrelevant to the transformation from events per unit anode length to events per unit amplitude.

The computed amplitude distributions will be voltage sensitive. Figures I.A.3 and I.A.4 show the calculated distribution at 3050 and at 4500 V using the test counter described in ANL-7595 and its

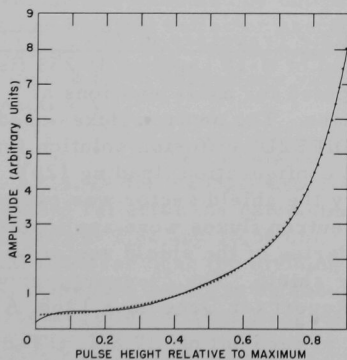


Fig. I.A.3. Response Distribution at 3050 V

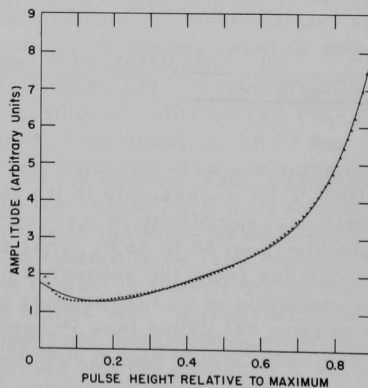


Fig. I.A.4. Response Distribution at 4500 V

calibration. The continuous line is a fifth-order least-squares polynomial fit. The distributions are shown only to within 90% of the maximum pulse height. The maximum height is achieved for events in excess of about 1500 anode radii from the tip, and the distribution increases sharply for amplitudes greater than 70% of maximum. As may be seen by comparison of the two figures, the response distribution is rather sensitive to counter voltage. Operating at lower voltages produces a response behavior closer to ideal insofar as fewer events are strongly degraded by the field.

A comparison of predicted response, with that actually observed, is given in Fig. 1.A.2. Two distinct de-excitation modes occur: one, involving betas at about 3 keV, is the dominant peak in the figure; another mode with energy of about 200 eV also occurs, however, and it is this line which causes the sharp increase in the spectrum below channel 20. A discriminator blocks all events below about channel 7. Statistical effects introduce substantial broadening into the measured result. The pulse-height distribution, determined using the calculated electric field (and the observed gain-voltage relationship), was area normalized to the experimental distribution of Fig. 1.A.2 in the region above channel 20. The mean value of multiplication was determined from the calculated distribution (it was 0.87 of the asymptotic multiplication reached at a large distance from the tip). This mean value was set equal to the pulse-height channel corresponding to the peak of the observed spectrum and the calculated low energy tail (the solid line in Fig. 1.A.2) was then drawn. The calculated distribution agrees well with the measured results within the limited region between contamination from the soft beta decay at low channels and statistical broadening effects at high channels.

b. FFTF Critical Assembly Experiments--Planning and Evaluation
(A. Travelli)

Last Reported: ANL-7640, pp. 18-20 (Nov 1969).

(i) Calculation of Reactor Rate Traverses in ZPPR/FTR-2 Shield Configuration. The radial variation of B-10 capture, U-238 fission, and Pu-239 fission rates have been computed for axial positions at 7.62, 35.56, and 55.88 cm from the dividing plane. The neutron fluxes used in the computations were obtained from a DIFF2D* diffusion solution for the ZPPR/FTR-2 assembly in its shield configuration (loading 120). For computational simplicity in r,z-geometry the shield sector was extended azimuthally from 80 to 360°. Thus the neutron fluxes were applicable only along radii far from the azimuthal boundaries of the shield sector and only for the condition of no fuel storage in the shield. The 29-energy-group cross-section set 29004 (see Progress Report for December 1968, ANL-7527, p. 9) was used, giving $k_{\text{eff}} = 0.9946$.

*Toppel, B. J., ANL-7332 (1967).

The traverses at 7.62 and 35.56 cm pass through the depleted zone, core, radial reflector, shield, and 11.06 cm of iron which simulate the heavy clamp that holds the matrix tubes in position. The core-axial reflector interface is at 45.811 cm, and the axial reflector ends at 76.302 cm. Thus, the traverse at 55.88 cm passes through the axial reflector for radii smaller than the core radius, then through the radial reflector, shield, and iron clamp.

Two reaction-rate curves were computed for each traverse at 7.62 and 35.56 cm. The calculation of the first reaction rate used the 29-group cross sections obtained from a 2100-group fundamental mode MC²* flux averaging for the core composition at criticality. Calculation of the second reaction-rate traverse used the 29-group cross sections obtained from a 2100-group fundamental mode MC² flux averaging for the radial reflector composition with zero buckling. The flux was normalized so that the B-10 capture and U-238 fission rates for the first calculation and the Pu-239 fission rate for the second calculation were unity at zero radius.

Two reaction-rate curves were also computed for each traverse at 55.88 cm. The calculation of the first reaction rate used cross sections averaged for the axial reflector composition with zero buckling rather than for core composition. The flux normalization was again chosen to obtain a reaction rate of unity at zero radius for the first calculation. The calculation of the second reaction-rate traverse used cross sections averaged for the core composition. The same flux, with the same normalization, was used as in the calculation of the first reaction rate traverse.

The computed reaction rates are compared in Figs. I.A.5, I.A.6, and I.A.7 with the experimental values reported in Sect. I.A.4.d. The experimental data for no fuel stored in the shield are indicated by crosses, reaction rates obtained by core spectrum averaging are indicated by dotted curves labeled "1," reaction rates obtained by radial reflector spectrum averaging are indicated by dotted curves labeled "2," and reaction rates obtained by axial reflector spectrum averaging are indicated by dotted curves labeled "3." Thus, type-1 curves are valid close to the core center, and type-2 or -3 curves are valid well inside the radial or axial reflectors, respectively.

The calculated B-10 capture reaction rate, shown in Fig. I.A.5, is not strongly dependent on the averaging of cross sections. In the radial reflector the calculated capture is too large by about 20% for the traverses at 7.62 and 35.56 cm. The calculated B-10 capture rate along a radial traverse near the dividing plane in ZPR-3 Assembly 56B was found by S₄ transport theory to be about 12% higher than the measured value in the radial reflector (see Progress Report for August 1969, ANL-7606, p. 16, Fig. I.B.7). In the case of Assembly 56B the boundary of the problem was at the outer edge of the reflector rather than at the outer edge of the matrix tube clamp.

*Toppel, B. J., *et al.*, ANL-7318 (1967).

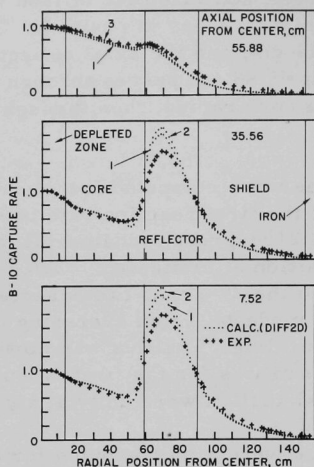


Fig. I.A.5. Radial Variation of B-10 Capture Rate in ZPPR/FTR-2 Shield Configuration

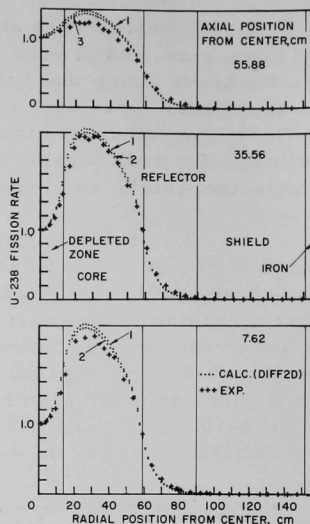


Fig. I.A.6. Radial Variation in U-238 Fission Rate in ZPPR/FTR-2 Shield Configuration

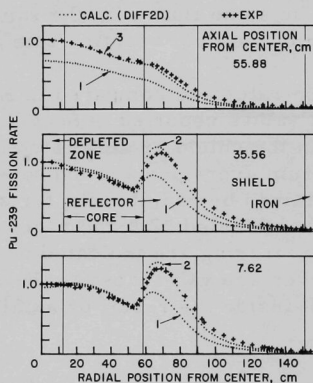


Fig. I.A.7
Radial Variation of Pu-239 Fission Rate in ZPPR/FTR-2 Shield Configuration

The calculated U-238 fission reaction rate also does not depend strongly on the cross-section averaging. The measured fission reaction rate, shown in Fig. I.A.6, exhibits local depressions associated with the two-drawer cell.

The calculated Pu-239 fission reaction rate (see Fig. I.A.7) does depend strongly on the averaging of the cross sections in the spectrum of the radial reflector. The calculated rate using reflector-averaged cross

sections is higher than the measured one by about 8% in the radial reflector for the 7.62- and 35.56-cm traverses. This compares to a value of about 6% for Assembly 56B, mentioned previously.

Note that the Pu-239 fission reaction-rate curve in the 55.88-cm traverse (type 3, axial reflector averaged) which is normalized to unity at zero radius, has a shape quite similar to but a magnitude quite different from the type-1 curve (core averaged). The difference between type 2 and 3 for any traverse is negligible.

The fluxes from the DIFF2D solution were also used to calculate each of the three reaction rates at zero radius and axial distances of 35.56 and 55.88 cm from the dividing place when the reaction rate at an axial distance of 7.62 cm was unity. These rates are compared with measured values in Table I.A.2.

TABLE I.A.2. Relative Reaction Rates at Zero Radius

Axial Position:	7.62 cm		35.56 cm		55.88 cm	
	Calc	Meas	Calc	Meas	Calc	Meas
B-10 capture	1.00	1.00	0.821	0.847	1.599	1.377
U-238 fission	1.00	1.00	0.639	0.619	0.221	0.216
Pu-239 fission	1.00	1.00	0.767	0.808	1.064	1.093

The shielding calculations reported above are preliminary and do not take into account several factors that might affect the results considerably. More complete analysis of the shielding experiments will be reported in the future.

3. ZPR-6 and -9 Operations and Analysis

a. Clean Critical Experiments (W. Y. Kato)

Not previously reported.

(i) ZPR-6 Assembly 6A. ZPR-6 Assembly 6A, the rebuilt version of Assembly 6, went critical in mid-November. ZPR-6 Assembly 6, the 4000-liter UO₂ core, was shut down prior to the completion of the experimental program so that the modifications could be made for the plutonium conversion. The main difference between Assemblies 6 and 6A is that the concentration of ²³⁵U in the region outside a radius of 77 cm in Assembly 6* was different from the central composition. The ²³⁵U concentration in Assembly 6A is essentially uniform throughout the system.

*Karam, R. A., et al., "A 4000-liter UO₂ Fast Core ZPR-6 Assembly 6," ANL-7410, pp. 75-80 (1969).

The material arrangement in Assembly 6A beyond a radius of 77 cm, however, is different from that in the central region, the difference being that 1/8-in.-thick ^{235}U plates were used in the outer region in every other 2- or 3-in. segments of the unit-cell drawer instead of the 1/16-in.-thick continuous column.

The critical mass of Assembly 6A, corrected for excess reactivity, but not for the difference in material arrangement in the outer region, was 1760 kg of ^{235}U .

The central neutron spectrum in Assembly 6A was measured, with the proton-recoil method, with the sodium present throughout the core and again after the sodium was removed from a 30-cm-radius central region. Calculations showed that at the center of this region the neutron spectrum above 1 keV was the same as the asymptotic spectrum for the sodium-free case. The proton-recoil method is suitable to measure neutron energies in the range between 1 MeV and 1 keV. For measurements such as reaction rates and Doppler effect, neutrons below 1 keV play a significant role and the minimum-size sodium-free region should be, according to calculations, at least 40 cm in radius. The Doppler effect at the center of this region was calculated to be 2.5% different from that obtained in a fully voided core.

The Doppler effect of a natural UO_2 sample was measured at the center of a 40-cm-radius, sodium-free region. The results are being analyzed.

The full unit-cell reaction rates (and ratios) of ^{235}U and ^{238}U were measured at the center of the 40-cm, sodium-free region at the core-reflector interface of the axial center, and at the radial "sodium-in" and "sodium-out" interface about the midplane of the core. The reaction rates as a function of depth within the plates were also measured.

Additionally, axial and radial traverses of ^{238}U fissions and captures and ^{235}U fissions were made for the purpose of extracting material buckling for the sodium-free core.

The reactivity worth of the sodium in the 40-cm central region (319 drawers) was -239.87 Ih or -0.524% $\Delta k/k$.

b. Mockup Experiments (J. W. Daughtry)

Last Reported: ANL-7640, pp. 20-21 (Nov 1969).

(i) Loading and Approach to Critical for the FTR-3 Homogeneous Reference Configuration. Upon completion of the FTR-2 experiments with ZPPR, the nickel and boron carbide used in those experiments were removed from ZPPR and transferred to ZPR-9 for the FTR-3 experiments. The critical assembly in which the FTR-3 experiments are to be performed

(designated ZPR-9 Assembly 26) had been preloaded to the extent possible with the available materials. With the additional materials from ZPPR, the loading of the reflector regions was completed and the sixteen peripheral control zones were loaded. Figures I.A.8 and I.A.9 show the estimated matrix-loading pattern for this assembly. Drawer loading patterns are shown in Figs. I.A.9-I.A.15. Some minor deviations from the piece-size distributions shown will be required due to inventory limitations.

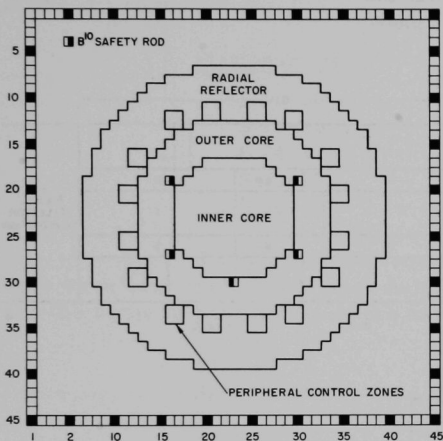


Fig. I.A.8. Stationary Half of FTR-3
Matrix-loading Pattern

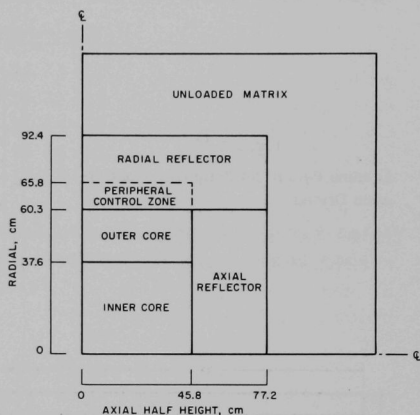


Fig. I.A.9. Side View of FTR-3 in ZPR-9

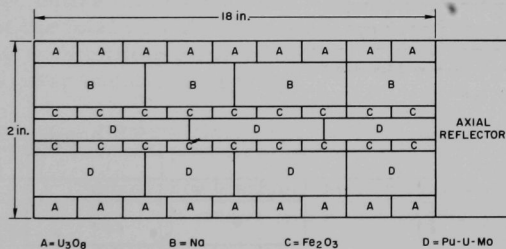


Fig. I.A.11
Loading Pattern for Inner-
core Drawer-type B

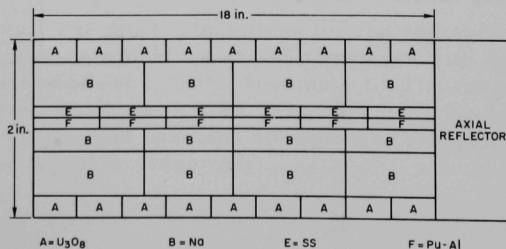


Fig. I.A.10

Loading Pattern for Inner-
core Drawer-type A

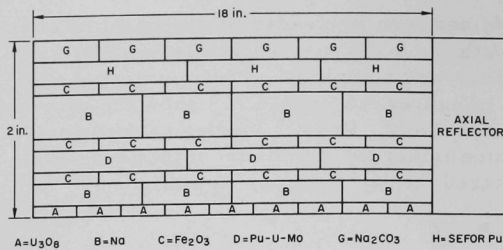


Fig. I.A.12
Loading Pattern for Outer-core Drawer

Fig. I.A.13
Loading Pattern for Peripheral Control-zone Drawer

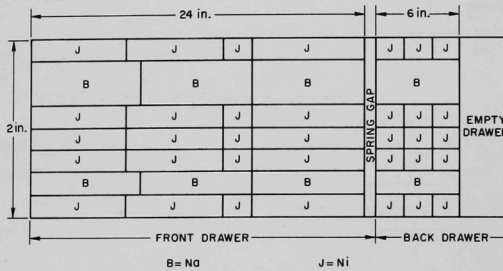
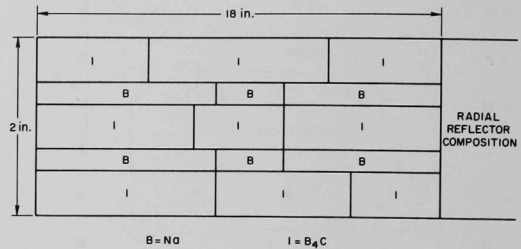
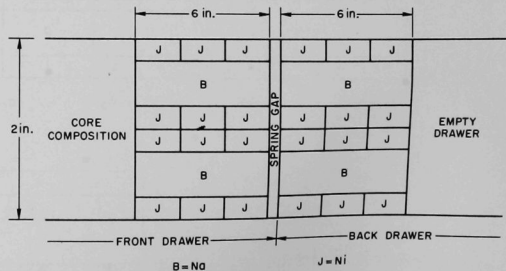


Fig. I.A.14
Loading Pattern for Radial-reflector Drawer

Fig. I.A.15
Loading Pattern for Axial-reflector Drawer



For the approach to critical two fission chambers were installed near the center of the core: one in the stationary half at matrix position S 22-24, and one in the movable half in matrix position M 24-22. The axis of the core is at location 23-23.

In the first fuel-loading step, plutonium fuel cans were loaded into the ten dual-purpose (DP) control-rod drawers. The locations of the DP rods are:

<u>Stationary Half</u>	<u>Movable Half</u>
S 16-20	M 21-21
S 16-26	M 21-25
S 24-27	M 24-19
S 30-19	M 24-23
S 30-26	M 24-27

To provide an adequate shutdown margin, five boron safety rods have been installed in each half. The locations of these boron rods are the same in both halves of the assembly:

S/M 19-16
 S/M 19-30
 S/M 27-16
 S/M 27-30
 S/M 30-23

After the safety and control rods were loaded and checked out, the entire inner core zone was loaded with fuel. This amounted to about 30% of the total calculated critical mass. The approach to critical is continuing with loading steps in the outer core zone and multiplication measurements after each loading step.

4. ZPR-3 and ZPPR Operations and Analysis

- a. Support for Routine Operation of the Critical Facilities
 (P. I. Amundson and R. G. Matlock)

Last Reported: ANL-7632, pp. 11-12 (Oct 1969).

(i) Pu-241 Decay. The final calculations for the reactivity effects due to Pu-241 decay have been performed and compared with data from ZPR-3 Assemblies 51 and 56B, and ZPPR Assembly 1. The results are illustrated in Figs. I.A.16, I.A.17, and I.A.18. The data from Assembly 56B appear to be unreasonable; this has been attributed to changes in cell air temperature over the life of the assembly.

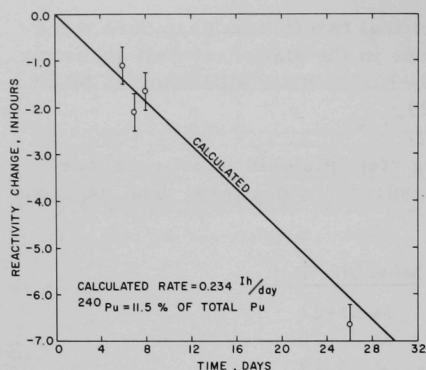


Fig. I.A.16. Reference-core Reactivity Loss, ZPPR Assembly 1

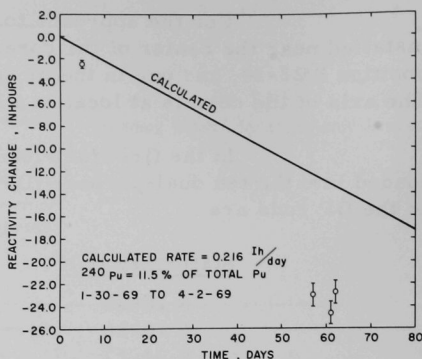


Fig. I.A.17. Reference-core Reactivity Loss, ZPR-3 Assembly 56B

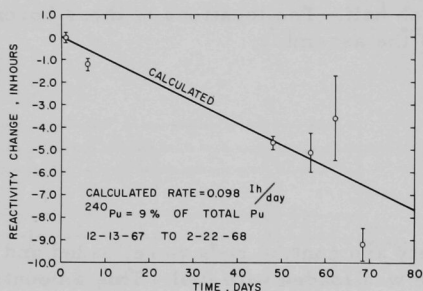


Fig. I.A.18
Reference-core Reactivity Loss, ZPR-3 Assembly 51

Recorded reactor temperatures for Assembly 56B show an 8-10°C temperature rise from the initial to the final reference core. This difference appeared primarily in the reflector and outer core regions. If we consider a temperature coefficient of 1 $\text{1h}/^\circ\text{C}$, about half that of the entire reactor, this would account for all of the discrepancy. Although this is not a rigorous correction, it is significant that a reasonable estimate of the temperature effect can conceivably eliminate the majority of the deviation between calculated and measured losses.

Since it is apparent that the effects of Pu-241 decay can be severe for experiments requiring references widely spaced in time (e.g., sodium-voiding), it is recommended that measurements with reference cores be repeated periodically throughout the life of an assembly in order to provide experimental corrections. Due to uncertainties in cross sections for the isotopes concerned, experimental values should prove more reliable than calculated values for the rate of reactivity loss.*

*Matlock, R. G., Kaiser, R. E., and Gasidlo, J. M., Reactivity Effects in Critical Facilities Due to Fissile Isotope Decay, Trans. Am. Nucl. Soc. 12(2) (Nov 1969).

b. Clean Critical Experiments (P. I. Amundson)

Last Reported: ANL-7640, pp. 21-23 (Nov 1969).

The short series of experiments with ZPR-3 Assembly 58 has been completed and the reflector changed from depleted uranium to lead for Assembly 59. A new critical approach was made, and the worths of the control and safety rods measured.

In Assembly 58 the total worth of the autorod (the usual polyethylene wedge between 1/4-in. pieces of boral in position 0-22) was determined by inverse kinetics analysis of five complete oscillations to be 0.00972% or 10.35 lh. The differential worth of the rod was measured by oscillating in and out a steel sample equal to about 10% of the autorod worth, and finding the change in rod position corresponding to this sample worth as a function of rod position. This change varied from 9.4 to 10.7 length units. The results for dp/dx along the length of the rod were fitted to various polynomial functions of x , the position. The best fit was a quadratic function, although a linear variation fitted almost as well.

In Assembly 58, radial reaction-rate traverses were carried with the Pu-239 and U-238 cylindrical fission chambers with a 1-in.-long fissile coating. The measurements were made in a 0.5-in.-dia tube, close to the axial core center line. The special core drawers are shown in Fig. I.A.19. The results are shown in Table I.A.3. Higher fission rates were obtained for the Pu-239 counter in between the drawers, and for the U-238 counter at the centers of the drawers.

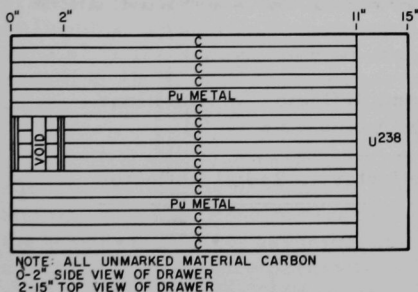


Fig. I.A.19. Core-drawer Loading for
 Radial Traverse in ZPR-3
 Assembly 58

TABLE I.A.3. Radial Fission Rate Distributions from ZPR-3 Assembly 58

Position	U-238		Pu-239	
	Rel Count	Error (%)	Rel Count	Error (%)
P-19	0.7154	0.6	0.7553	0.6
P-18-19	0.7730	0.6	0.8385	0.5
P-18	0.8680	0.5	0.8979	0.5
P-17-18	0.8997	0.5	0.9584	0.5
P-17	0.9568	0.5	0.9710	0.5
P-16-17	0.9631	0.5	1.0147	0.5
P-16	1.000	-	1.000	-
P-15-16	0.9615	0.5	1.0149	0.5
P-15	0.9672	0.5	0.9708	0.5
P-14-15	0.9037	0.5	0.9588	0.5
P-14	0.8695	0.5	0.8961	0.5
P-13-14	0.7879	0.6	0.8484	0.5
P-13	0.7187	0.6	0.7549	0.6
P-12-13	0.6059	0.6	0.6780	0.6
P-12	0.5049	0.6	0.5640	0.6
P-11-12	0.3380	0.8	0.4463	0.7
P-11	0.1852	1.1	0.3238	0.8
P-10	0.0628	1.3	0.1726	1.1
P-9	0.0231	1.5	0.0939	1.2
P-8	0.0093	1.7	0.0516	1.1
P-7	0.00351	2.2	0.0267	1.5
P-6	0.00131	3.6	0.0129	1.5

Horizontal matrix pitch is 2.1833 in.; core center is P-16.

Radial reactivity traverses were also measured using depleted uranium and Pu-239 samples, and central reactivity measurements were made with nine samples (U-235, Pu-239, U-238, and B-10). The results are being analyzed.

The core drawers in Assembly 58 were removed from the lattice, and the radial and axial reflectors replaced by lead blocks. A new approach to critical was initiated. The critical loading is shown in Fig. I.A.20, and contained 75.89 kg Pu-239 and 0.20 kg Pu-241. Control Rod 5 was removed 1.83 in. The core-drawer numbers refer to their slightly different contents and were detailed in ANL-7640. The half-drawer type 2 in position S-19 in Half 2 was used to prevent too much excess reactivity in this loading. The average core and blanket compositions are given in Table I.A.4. The equivalent cylindrical loading is exactly as given in ANL-7640 except that the equivalent core radius is 23.830 cm.

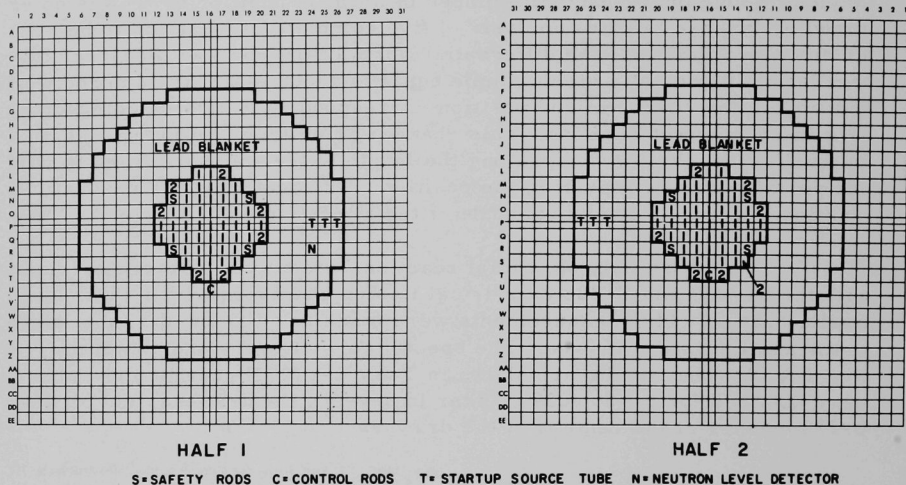


Fig. I.A.20. Critical Loading for ZPR-3 Assembly 59

TABLE I.A.4. Average Core and Reflector Compositions for ZPR-3 Assembly 59 (Atoms/cc $\times 10^{-21}$)

Isotope	Core	Axial Reflector	Radial Reflector
Pu-239	2.1030	-	-
Pu-240	0.1003	-	-
Pu-241	0.0056	-	-
Al	0.217	-	-
C	59.02	-	-
Fe	7.717	5.593	4.540
Cr	1.919	1.391	1.129
Ni	0.875	0.609	0.494
Mn	0.0801	0.0581	0.0471
Si	0.0941	0.0682	0.0553
Pb	-	28.16 ^a	28.24 ^a

^aPreliminary values.

The worth of the safety and control rods were measured by the usual method. The results are shown in Table I.A.5. Rods 3 and 7 will be the lowest of the safeties in their respective halves so the total safety rod worth will be more than 3.16%.

TABLE I.A.5. Safety and Control Rod Worths
for ZPR-3 Assembly 59

Rod	Worth ($\% \Delta k/k$)
Safety Rod 3, Half 2	0.37
Safety Rod 7, Half 1	0.42
Control Rod 5, Half 2	0.33
Control Rod 6, Half 1	0.12
Total 8 Safety Rods	>3.16

Erratum. In the September report of work done at ZPR-3 under this detail (ANL-7618, p. 14) the captions for Figs. I.A.7 and I.A.8, showing the axial reaction rate traverses for B-10 and Pu-239 in Assembly 57, were interchanged.

c. Doppler Experiments (R. E. Kaiser)

Last Reported: ANL-7632, pp. 13-14 (Oct 1969).

Analysis of the natural UO_2 Doppler experiments in ZPR-3 Assembly 53 with the ENDF/B cross section set has been completed. The procedure included RABBLE calculations of the change in σ_a of U-238 due to Doppler broadening, two-dimensional diffusion calculations of fluxes and adjoints in the sample, and two-dimensional perturbation calculations of the resulting $\Delta k/k$. No expansion corrections have been made, as this has been shown to be negligible for samples of this type.

Resolved resonance parameters and appropriate statistical parameters for the unresolved resonances were obtained from Schmidt,* and the cross sections for the nonresonant materials were obtained from the ENDF/B library, assuming homogeneous shielding in an Assembly 53 spectrum. Resonance parameters in the unresolved region for U-238 were obtained statistically, using a chi squared ($\nu=1$) distribution for selection of neutron widths, and a Wigner distribution for the energy spacing. Radiation widths were assumed constant. P-wave resonances were included, but contributed only a few percent of the total effect. One group of 30 resonances was used to determine average broad-group cross sections from the resolved limit (3.91 keV) up to 24.8 keV. Estimates based on the calculated

*Schmidt, J. J., Neutron Cross Sections for Fast Reactor Materials, KFK 120 (Feb 1966).

$\delta\Sigma_a$ and weighted by $\phi\phi^*$ at the center of the reactor indicated that groups above 24.8 keV would contribute less than one percent of the total change in k .

Cross sections for U-238, U-235, and oxygen for the sample configuration were obtained from an MC² run, and the U-238 values were then modified according to the RABBLE results to give cross sections at 300, 500, 800, and 1100°K. The initial 24-group ENDF/B cross-section set was then collapsed to 15 groups. Only those groups in which the Doppler effect was insignificant were collapsed. The resulting 15-group cross-section set was then used in a two-dimensional diffusion problem and the reactivity differences evaluated from perturbation theory. The results of the calculations and the experimental values are given in Table I.A.6.

TABLE I.A.6. Calculated and Measured Reactivity Change in Natural UO₂ Doppler Experiment in ZPR-3 Assembly 53

T (°K)	Measured $\Delta k/k$	Calculated $\Delta k/k$	% Dev ^a
300-500	$-(5.05 \pm 0.05) \times 10^{-6}$	-6.13×10^{-6}	21.4
300-800	$-(1.09 \pm 0.05) \times 10^{-5}$	-1.27×10^{-5}	16.5
300-1100	$-(1.55 \pm 0.05) \times 10^{-5}$	-1.76×10^{-5}	13.5

^aExperimental value as standard.

d. Mockup Critical Experiments (W. P. Keeney)

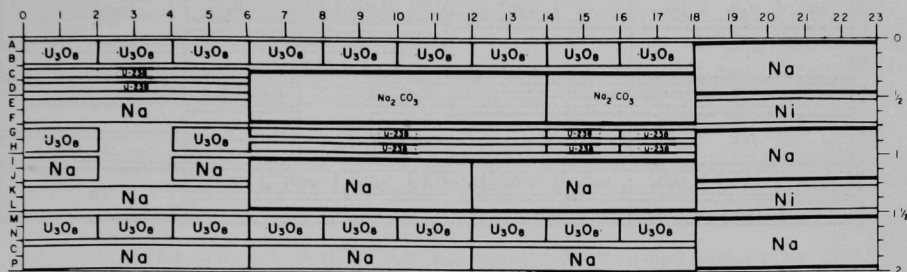
Last Reported: ANL-7640, p. 24 (Nov 1969).

At the conclusion of experiments with Assembly 2 of the FTR Resumed Phase-B Critical Experiments Program for ZPPR, all of the materials necessary to construct the FTR-3 on ZPR-9 were transferred to Argonne, Ill.

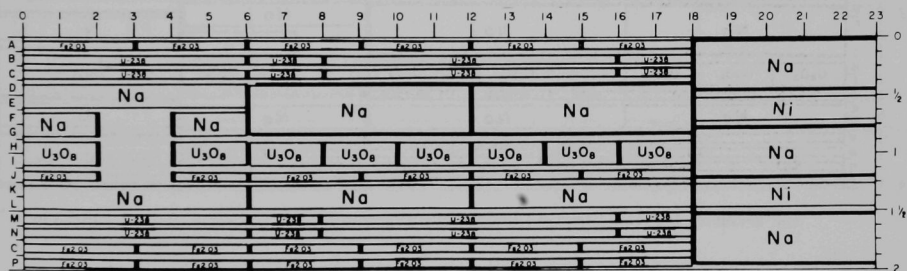
This report includes the data for the radial reaction-rate counter traverses, the normalization of the counter traverses at the various axial elevations, additional subcritical counts on the PNL fission counters, and preliminary results of the central fission ratios. The final fission-ratio results are awaiting a reconfirmation of the thermal calibration of the counters. All of the activation measurements will be reported after the intercalibration of the three counter systems has been completed. This calibration has been delayed due to a magnetic tape readout malfunction.

(i) Radial Reaction-rate Counter Traverses. Radial reaction-rate traverses at 3-, 14-, and 22-in. axial elevations through the 137 row were made with U-238, Pu-239, and B-10 counters in the FTR-2 shield configuration, both with and without fuel in the fuel storage region (see Progress Report for October 1969, ANL-7632, pp. 14-22). The loading

diagrams of the drawers in each zone of the assembly are shown in Figs. I.A.21 to I.A.30. Figure I.A.31 shows the physical construction of the ZPPR Traverse Fission Counters which were described in the Progress Report for August 1969, ANL-7606, p. 28, along with the BF_3 counter used in these traverses. The normalized tabulated data are plotted in Figs. I.A.32 to I.A.49.

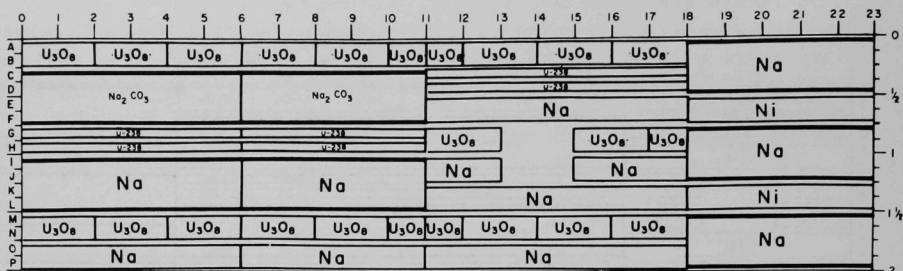


(a) 1-column Depleted Uranium Drawer

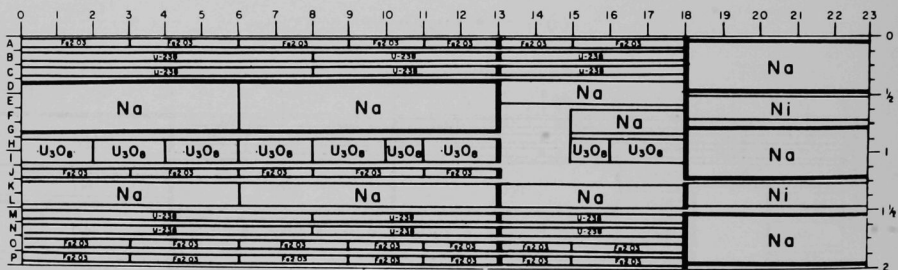


(b) 2-column Depleted Uranium Drawer

Fig. I.A.21. Depleted-core-zone Drawers Accommodating Radial Traverse at 3-in. Axial Position in ZPPR/FTR-2 Shield Configuration. Side View: 0-6 in. Top View: 6-23 in.



(a) 1-column Depleted Uranium Drawer. Side View: 11-18 in. Top View: 0-11 in., 18-23 in.



(b) 2-column Depleted Uranium Drawer. Side View: 13-18 in. Top View: 0-13 in., 18-23 in.

Fig. I.A.22. Depleted-core-zone Drawers Accommodating Radial Traverse at 14-in. Axial Position in ZPPR/FTR-2 Shield Configuration

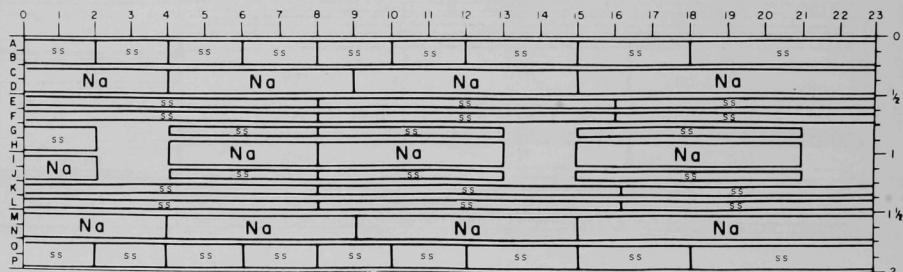
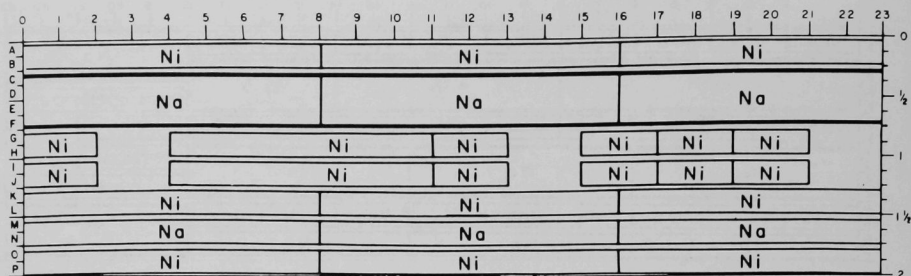


Fig. I.A.24

	0	1	2	3	4	5	6	7	8	9	10	11	12	13	14	15	16	17	18	19	20	21	22	23	
A	U ₃ O ₈	U ₃ O ₈	U ₃ O ₈	U ₃ O ₈	U ₃ O ₈	U ₃ O ₈	U ₃ O ₈	U ₃ O ₈	U ₃ O ₈	U ₃ O ₈	U ₃ O ₈	U ₃ O ₈	U ₃ O ₈	U ₃ O ₈	U ₃ O ₈	U ₃ O ₈	U ₃ O ₈	U ₃ O ₈	Na						0
B	Pu (ZPPR)		Na ₂ CO ₃		Na ₂ CO ₃		Na ₂ CO ₃		Na ₂ CO ₃		Na ₂ CO ₃		Na ₂ CO ₃		Na ₂ CO ₃		Na ₂ CO ₃		Na		Na		Na		
C	Na		Na		Na		Na		Na		Na		Na		Na		Na		Na		Na		Na		1/2
D	U ₃ O ₈	U ₃ O ₈	U ₃ O ₈	U ₃ O ₈	U ₃ O ₈	U ₃ O ₈	U ₃ O ₈	U ₃ O ₈	U ₃ O ₈	U ₃ O ₈	U ₃ O ₈	U ₃ O ₈	U ₃ O ₈	U ₃ O ₈	U ₃ O ₈	U ₃ O ₈	U ₃ O ₈	U ₃ O ₈	Na						
E	Na	Na	Na	Na	Na	Na	Na	Na	Na	Na	Na	Na	Na	Na	Na	Na	Na	Na	Na						
F	U ₃ O ₈	U ₃ O ₈	U ₃ O ₈	U ₃ O ₈	U ₃ O ₈	U ₃ O ₈	U ₃ O ₈	U ₃ O ₈	U ₃ O ₈	U ₃ O ₈	U ₃ O ₈	U ₃ O ₈	U ₃ O ₈	U ₃ O ₈	U ₃ O ₈	U ₃ O ₈	U ₃ O ₈	U ₃ O ₈	Na						
G	Na	Na	Na	Na	Na	Na	Na	Na	Na	Na	Na	Na	Na	Na	Na	Na	Na	Na	Na						
H	U ₃ O ₈	U ₃ O ₈	U ₃ O ₈	U ₃ O ₈	U ₃ O ₈	U ₃ O ₈	U ₃ O ₈	U ₃ O ₈	U ₃ O ₈	U ₃ O ₈	U ₃ O ₈	U ₃ O ₈	U ₃ O ₈	U ₃ O ₈	U ₃ O ₈	U ₃ O ₈	U ₃ O ₈	U ₃ O ₈	Na						
I	Na	Na	Na	Na	Na	Na	Na	Na	Na	Na	Na	Na	Na	Na	Na	Na	Na	Na	Na						
J	U ₃ O ₈	U ₃ O ₈	U ₃ O ₈	U ₃ O ₈	U ₃ O ₈	U ₃ O ₈	U ₃ O ₈	U ₃ O ₈	U ₃ O ₈	U ₃ O ₈	U ₃ O ₈	U ₃ O ₈	U ₃ O ₈	U ₃ O ₈	U ₃ O ₈	U ₃ O ₈	U ₃ O ₈	U ₃ O ₈	Na						
K	Na	Na	Na	Na	Na	Na	Na	Na	Na	Na	Na	Na	Na	Na	Na	Na	Na	Na	Na						
L	U ₃ O ₈	U ₃ O ₈	U ₃ O ₈	U ₃ O ₈	U ₃ O ₈	U ₃ O ₈	U ₃ O ₈	U ₃ O ₈	U ₃ O ₈	U ₃ O ₈	U ₃ O ₈	U ₃ O ₈	U ₃ O ₈	U ₃ O ₈	U ₃ O ₈	U ₃ O ₈	U ₃ O ₈	U ₃ O ₈	Na						
M	Na	Na	Na	Na	Na	Na	Na	Na	Na	Na	Na	Na	Na	Na	Na	Na	Na	Na	Na						
N	U ₃ O ₈	U ₃ O ₈	U ₃ O ₈	U ₃ O ₈	U ₃ O ₈	U ₃ O ₈	U ₃ O ₈	U ₃ O ₈	U ₃ O ₈	U ₃ O ₈	U ₃ O ₈	U ₃ O ₈	U ₃ O ₈	U ₃ O ₈	U ₃ O ₈	U ₃ O ₈	U ₃ O ₈	U ₃ O ₈	Na						
O	Na	Na	Na	Na	Na	Na	Na	Na	Na	Na	Na	Na	Na	Na	Na	Na	Na	Na	Na						
P	Na	Na	Na	Na	Na	Na	Na	Na	Na	Na	Na	Na	Na	Na	Na	Na	Na	Na	Na						

(a) 1-column Pu Drawer

	0	1	2	3	4	5	6	7	8	9	10	11	12	13	14	15	16	17	18	19	20	21	22	23	
A	U ₃ O ₈	U ₃ O ₈	U ₃ O ₈	U ₃ O ₈	U ₃ O ₈	U ₃ O ₈	U ₃ O ₈	U ₃ O ₈	U ₃ O ₈	U ₃ O ₈	U ₃ O ₈	U ₃ O ₈	U ₃ O ₈	U ₃ O ₈	U ₃ O ₈	U ₃ O ₈	U ₃ O ₈	U ₃ O ₈	Na						0
B	Pu (ZPPR)		Pu (ZPPR)		Pu (ZPPR)		Pu (ZPPR)		Pu (ZPPR)		Pu (ZPPR)		Pu (ZPPR)		Pu (ZPPR)		Pu (ZPPR)		Na		Na		Na		
C	Na		Na		Na		Na		Na		Na		Na		Na		Na		Na		Na		Na		1/2
D	Na	Na	Na	Na	Na	Na	Na	Na	Na	Na	Na	Na	Na	Na	Na	Na	Na	Na	Na						
E	Na	Na	Na	Na	Na	Na	Na	Na	Na	Na	Na	Na	Na	Na	Na	Na	Na	Na	Na						
F	Na	Na	Na	Na	Na	Na	Na	Na	Na	Na	Na	Na	Na	Na	Na	Na	Na	Na	Na						
G	U ₃ O ₈	U ₃ O ₈	U ₃ O ₈	U ₃ O ₈	U ₃ O ₈	U ₃ O ₈	U ₃ O ₈	U ₃ O ₈	U ₃ O ₈	U ₃ O ₈	U ₃ O ₈	U ₃ O ₈	U ₃ O ₈	U ₃ O ₈	U ₃ O ₈	U ₃ O ₈	U ₃ O ₈	U ₃ O ₈	Na						
H	U ₃ O ₈	U ₃ O ₈	U ₃ O ₈	U ₃ O ₈	U ₃ O ₈	U ₃ O ₈	U ₃ O ₈	U ₃ O ₈	U ₃ O ₈	U ₃ O ₈	U ₃ O ₈	U ₃ O ₈	U ₃ O ₈	U ₃ O ₈	U ₃ O ₈	U ₃ O ₈	U ₃ O ₈	U ₃ O ₈	Na						
I	Na	Na	Na	Na	Na	Na	Na	Na	Na	Na	Na	Na	Na	Na	Na	Na	Na	Na	Na						
J	Na	Na	Na	Na	Na	Na	Na	Na	Na	Na	Na	Na	Na	Na	Na	Na	Na	Na	Na						
K	Na	Na	Na	Na	Na	Na	Na	Na	Na	Na	Na	Na	Na	Na	Na	Na	Na	Na	Na						
L	Na	Na	Na	Na	Na	Na	Na	Na	Na	Na	Na	Na	Na	Na	Na	Na	Na	Na	Na						
M	Pu (ZPPR)	Pu (ZPPR)	Pu (ZPPR)	Pu (ZPPR)	Pu (ZPPR)	Pu (ZPPR)	Pu (ZPPR)	Pu (ZPPR)	Pu (ZPPR)	Pu (ZPPR)	Pu (ZPPR)	Pu (ZPPR)	Pu (ZPPR)	Pu (ZPPR)	Pu (ZPPR)	Pu (ZPPR)	Pu (ZPPR)	Pu (ZPPR)	Na						
N	U ₃ O ₈	U ₃ O ₈	U ₃ O ₈	U ₃ O ₈	U ₃ O ₈	U ₃ O ₈	U ₃ O ₈	U ₃ O ₈	U ₃ O ₈	U ₃ O ₈	U ₃ O ₈	U ₃ O ₈	U ₃ O ₈	U ₃ O ₈	U ₃ O ₈	U ₃ O ₈	U ₃ O ₈	U ₃ O ₈	Na						
O	Na	Na	Na	Na	Na	Na	Na	Na	Na	Na	Na	Na	Na	Na	Na	Na	Na	Na	Na						
P	Na	Na	Na	Na	Na	Na	Na	Na	Na	Na	Na	Na	Na	Na	Na	Na	Na	Na	Na						

(b) 2-column Pu Drawer

Fig. I.A.25. Core Drawers Accommodating Radial Traverse at 3-in. Axial Position in ZPPR/FTR-2 Shield Configuration. Side View: 0-4 in. Top View: 4-23 in.

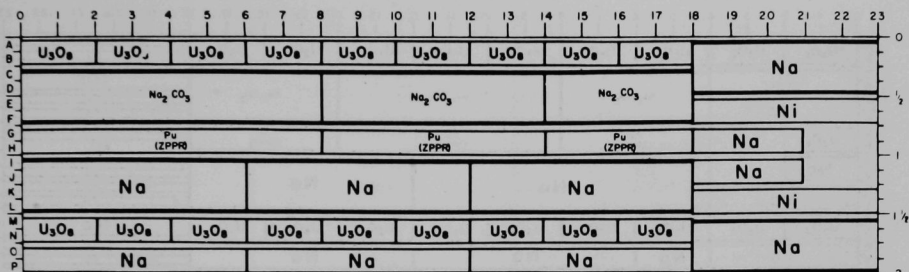
0	1	2	3	4	5	6	7	8	9	10	11	12	13	14	15	16	17	18	19	20	21	22	23
A	U ₃ O ₈	U ₃ O ₈	U ₃ O ₈	U ₃ O ₈	U ₃ O ₈	U ₃ O ₈	U ₃ O ₈	U ₃ O ₈	U ₃ O ₈	U ₃ O ₈	U ₃ O ₈	U ₃ O ₈	U ₃ O ₈	U ₃ O ₈	U ₃ O ₈	U ₃ O ₈							
B	Na ₂ CO ₃							Na ₂ CO ₃					Pu (ZPPR)					Na					
C																							
D													Na					Ni					
E																							
F	Pu (ZPPR)							Pu (ZPPR)															
G																							
H																							
I	Na							Na															
J																							
K													Na					Ni					
L																							
M	U ₃ O ₈	U ₃ O ₈	U ₃ O ₈	U ₃ O ₈	U ₃ O ₈	U ₃ O ₈	U ₃ O ₈	U ₃ O ₈	U ₃ O ₈	U ₃ O ₈	U ₃ O ₈	U ₃ O ₈	U ₃ O ₈	U ₃ O ₈	U ₃ O ₈	U ₃ O ₈		Na					
N	Na							Na					Na										
O																							

(a) 1-column Pu Drawer

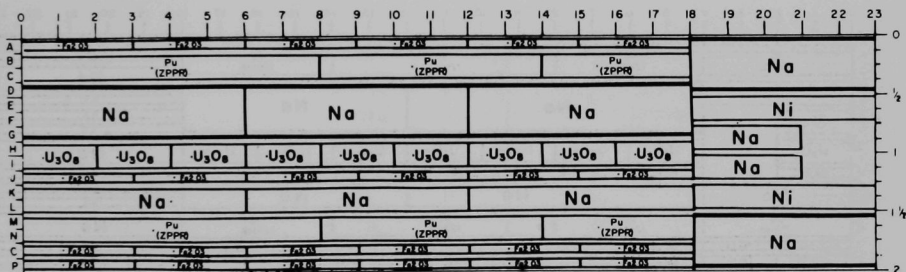
0	1	2	3	4	5	6	7	8	9	10	11	12	13	14	15	16	17	18	19	20	21	22	23
A	Pu (ZPPR)		Pu (ZPPR)		Pu (ZPPR)		Pu (ZPPR)		Pu (ZPPR)		Pu (ZPPR)		Pu (ZPPR)		Pu (ZPPR)		Pu (ZPPR)						
B	Pu (ZPPR)		Pu (ZPPR)		Pu (ZPPR)		Pu (ZPPR)		Pu (ZPPR)		Pu (ZPPR)		Pu (ZPPR)		Pu (ZPPR)		Pu (ZPPR)		Na				
C																							
D																							
E	Na		Na		Na		Na		Na		Na		Na		Na		Na		Ni				
F																							
G																							
H	U ₃ O ₈	U ₃ O ₈	U ₃ O ₈	U ₃ O ₈	U ₃ O ₈	U ₃ O ₈	U ₃ O ₈	U ₃ O ₈	U ₃ O ₈	U ₃ O ₈	U ₃ O ₈	U ₃ O ₈	U ₃ O ₈	U ₃ O ₈	U ₃ O ₈	U ₃ O ₈	U ₃ O ₈		Na				
I	Pu (ZPPR)		Pu (ZPPR)		Pu (ZPPR)		Pu (ZPPR)		Pu (ZPPR)		Pu (ZPPR)		Pu (ZPPR)		Pu (ZPPR)		Pu (ZPPR)						
J																							
K																							
L	Na		Na		Na		Na		Na		Na		Na		Na		Na		Ni				
M																							
N	Pu (ZPPR)		Pu (ZPPR)		Pu (ZPPR)		Pu (ZPPR)		Pu (ZPPR)		Pu (ZPPR)		Pu (ZPPR)		Pu (ZPPR)		Pu (ZPPR)						
O																							
P																							

(b) 2-column Pu Drawer

Fig. I.A.26. Core Drawers Accommodating Radial Traverse at 14-in. Axial Position in ZPPR/FTR-2 Shield Configuration. Top View: 0-13 in., 18-23 in. Side View: 13-18 in.



(a) 1-column Pu Drawer



(b) 2-column Pu Drawer

Fig. I.A.27. Core Drawers Accommodating Radial Traverse at 22-in. Axial Position in ZPPR/FTR-2 Shield Configuration. Top View: 0-18 in, Side View: 18-23 in.

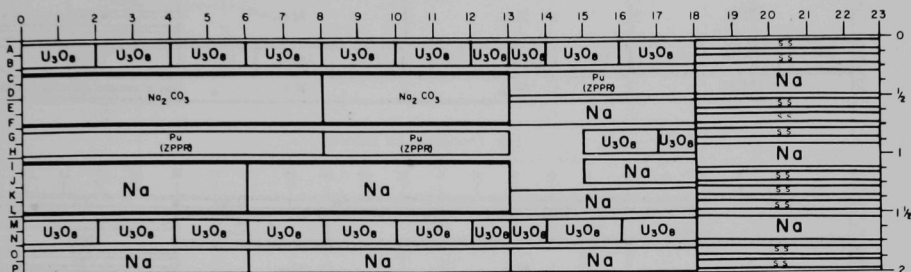
	0	1	2	3	4	5	6	7	8	9	10	11	12	13	14	15	16	17	18	19	20	21	22	23	
A	U ₃ O ₈	U ₃ O ₈			U ₃ O ₈	U ₃ O ₈	U ₃ O ₈	U ₃ O ₈	U ₃ O ₈	U ₃ O ₈	U ₃ O ₈	U ₃ O ₈	U ₃ O ₈	U ₃ O ₈	U ₃ O ₈	U ₃ O ₈	U ₃ O ₈								0
B																									
C																									
D																									
E																									
F																									
G																									
H																									
I																									
J																									
K																									
L																									
M																									
N																									
O																									
P																									

(a) 1-column Pu Drawer

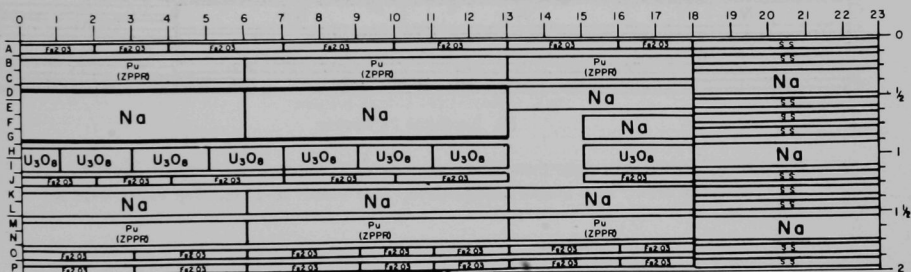
	0	1	2	3	4	5	6	7	8	9	10	11	12	13	14	15	16	17	18	19	20	21	22	23	
A																									0
B																									
C																									
D																									
E																									
F																									
G																									
H																									
I																									
J																									
K																									
L																									
M																									
N																									
O																									
P																									

(b) 2-column Pu Drawer

Fig. I.A.28. Fuel-storage-zone Drawers Accommodating Radial Traverse at 3-in. Axial Position in ZPPR/FTR-2 Shield Configuration. Side View: 0-4 in. Top View: 4-23 in.



(a) 1-column Pu Drawer



(b) 2-column Pu Drawer

Fig. I.A.29. Fuel-storage-zone Drawers Accommodating Radial Traverse at 14-in. Axial Position in ZPPR/FTR-2 Shield Configuration, Side View: 13-18 in. Top View: 0-13 in., 18-23 in.

O	1	2	3	4	5	6	7	8	9	10	11	12	13	14	15	16	17	18	19	20	21	22	23
A	U ₃ O ₈	U ₃ O ₈	U ₃ O ₈	U ₃ O ₈	U ₃ O ₈	U ₃ O ₈	U ₃ O ₈	U ₃ O ₈	U ₃ O ₈	U ₃ O ₈	U ₃ O ₈	U ₃ O ₈	U ₃ O ₈	U ₃ O ₈	U ₃ O ₈	U ₃ O ₈	U ₃ O ₈	U ₃ O ₈	U ₃ O ₈	U ₃ O ₈	U ₃ O ₈	U ₃ O ₈	U ₃ O ₈
B	Na ₂ CO ₃												Na										0
C	Na ₂ CO ₃												Na										1/2
D	Na ₂ CO ₃												Na										1
E	Pu (ZPPR)												Pu (ZPPR)										1 1/4
F	Pu (ZPPR)												Pu (ZPPR)										2
G	Na												Na										2
H	Na												Na										2
I	Na												Na										2
J	Na												Na										2
K	Na												Na										2
L	Na												Na										2
M	Na												Na										2
N	Na												Na										2
O	Na												Na										2
P	Na												Na										2

(a) 1-column Pu Drawer

O	1	2	3	4	5	6	7	8	9	10	11	12	13	14	15	16	17	18	19	20	21	22	23
A	U ₃ O ₈	U ₃ O ₈	U ₃ O ₈	U ₃ O ₈	U ₃ O ₈	U ₃ O ₈	U ₃ O ₈	U ₃ O ₈	U ₃ O ₈	U ₃ O ₈	U ₃ O ₈	U ₃ O ₈	U ₃ O ₈	U ₃ O ₈	U ₃ O ₈	U ₃ O ₈	U ₃ O ₈	U ₃ O ₈	U ₃ O ₈	U ₃ O ₈	U ₃ O ₈	U ₃ O ₈	U ₃ O ₈
B	Pu (ZPPR)												Pu (ZPPR)										0
C	Pu (ZPPR)												Pu (ZPPR)										1/2
D	Na												Na										1
E	Na												Na										1 1/4
F	Na												Na										2
G	Na												Na										2
H	Na												Na										2
I	Na												Na										2
J	Na												Na										2
K	Na												Na										2
L	Na												Na										2
M	Na												Na										2
N	Na												Na										2
O	Na												Na										2
P	Na												Na										2

(b) 2-column Pu Drawer

Fig. I.A.30. Fuel-storage-zone Drawers Accommodating Radial Traverse at 22-in. Axial Position in ZPPR/FTR-2 Shield Configuration. Side View: 18-23 in. Top View: 0-18 in.

Pu-239: COUNTER NO. 76

COMPOSITION: 94.452% Pu-239
 5.263% Pu-240
 0.272% Pu-241
 0.013% Pu-242

LOADING: 107.7 μ g

ACTIVE LENGTH: 2.173 in.

U-238: COUNTER NO. 114

COMPOSITION: 99.9986% U-238

LOADING: 1214.8 μ g

ACTIVE LENGTH - 2.173 in.

SKETCH OF Pu-239 OR U-238 COUNTER:

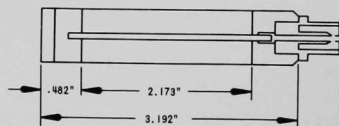


Fig. I.A.31

ZPPR Traverse Fission Counters

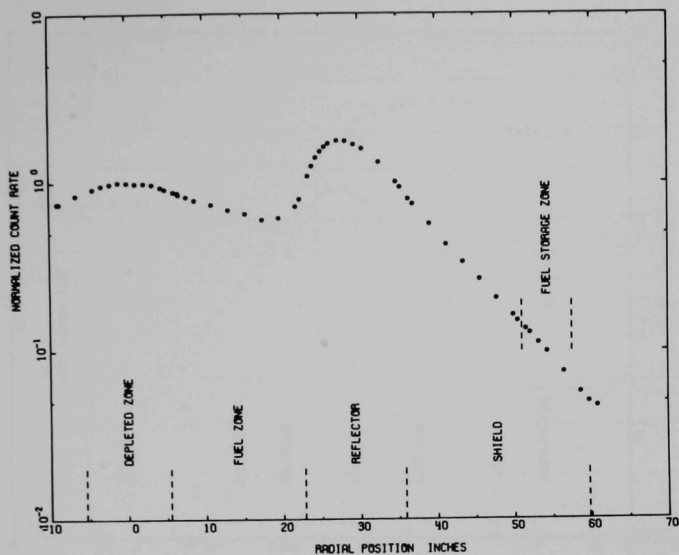


Fig. I.A.32. Traverse with BF_3 Counter at 3-in. Axial Position without Fuel in Fuel-storage Area

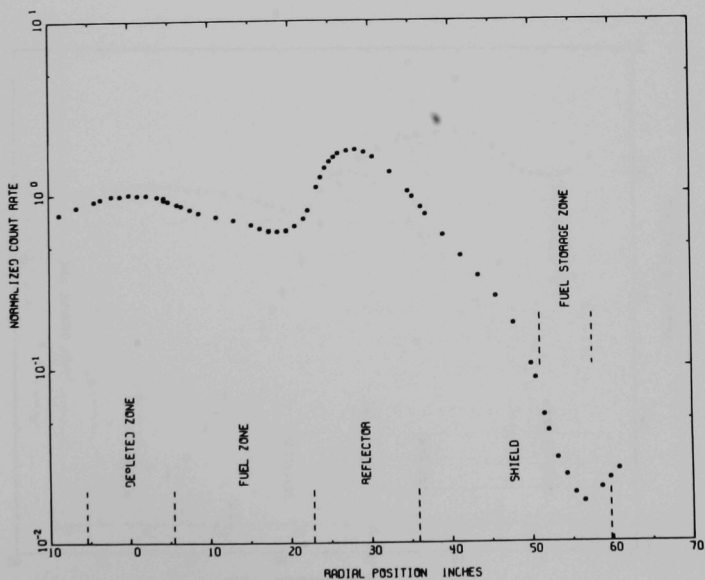


Fig. I.A.33. Traverse with BF_3 Counter at 3-in. Axial Position with Fuel in Fuel-storage Area

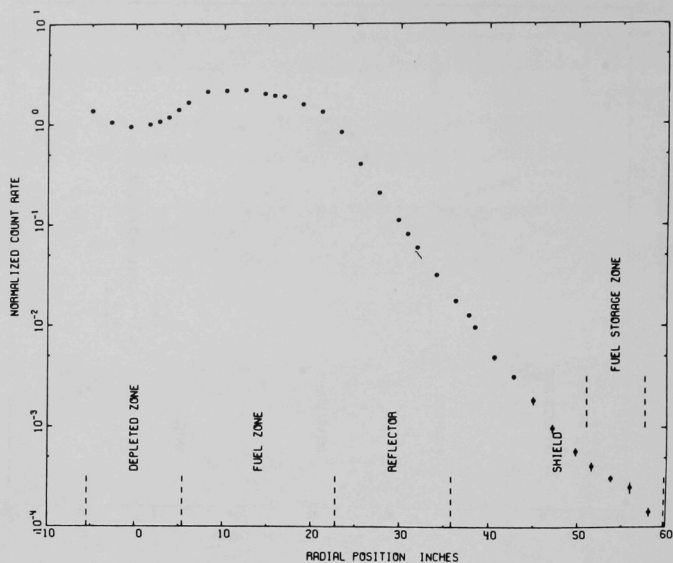


Fig. I.A.34. Traverse with U-238 Counter at 3-in. Axial Position without Fuel in Fuel-storage Area.

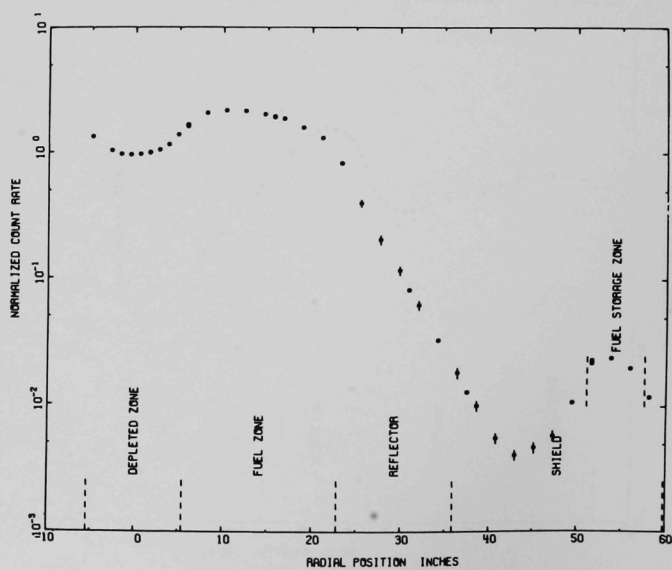


Fig. I.A.35. Traverse with U-238 Counter at 3-in. Axial Position with Fuel in Fuel-storage Area

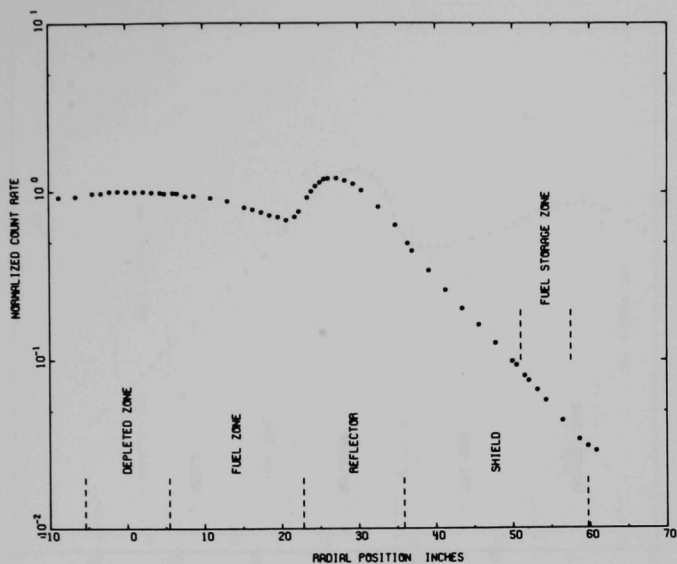


Fig. I.A.36. Traverse with Pu-239 Counter at 3-in. Axial Position without Fuel in Fuel-storage Area

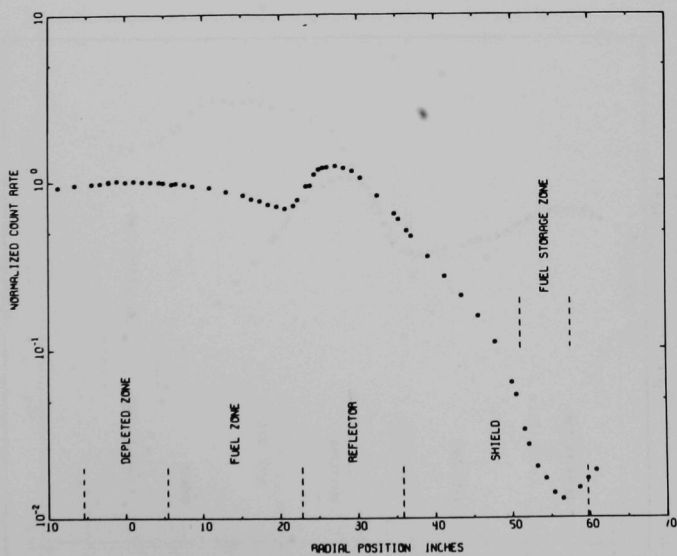


Fig. I.A.37. Traverse with Pu-239 Counter at 3-in. Axial Position with Fuel in Fuel-storage Area

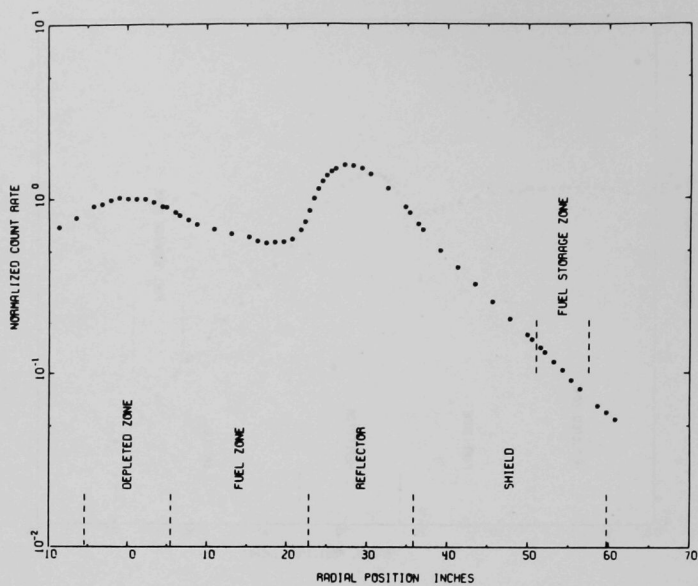


Fig. I.A.38. Traverse with BF_3 Counter at 14-in. Axial Position without Fuel in Fuel-storage Area

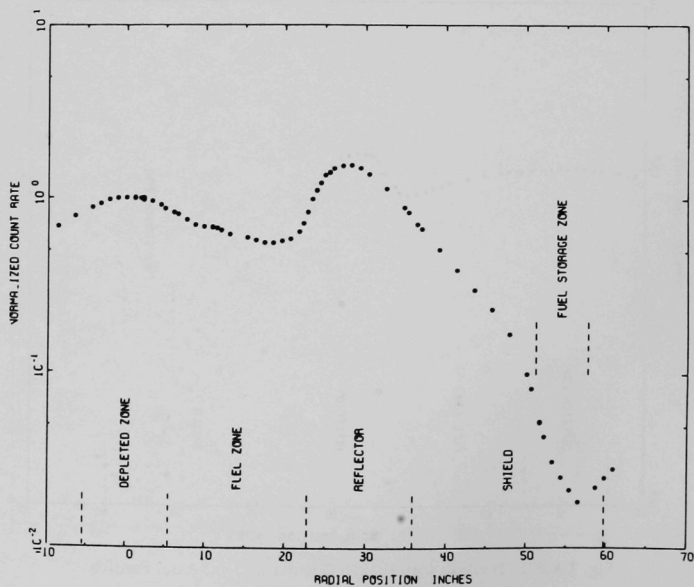


Fig. I.A.39. Traverse with BF_3 Counter at 14-in. Axial Position with Fuel in Fuel-storage Area

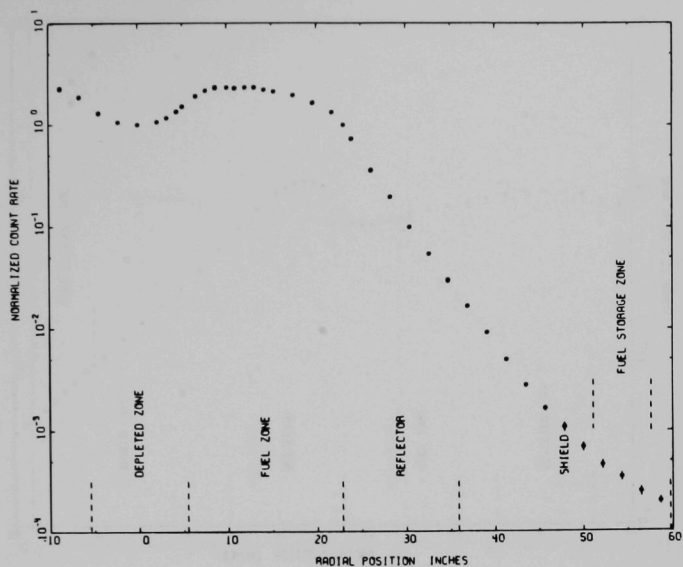


Fig. I.A.40. Traverse with U-238 Counter at 14-in. Axial Position without Fuel in Fuel-storage Area

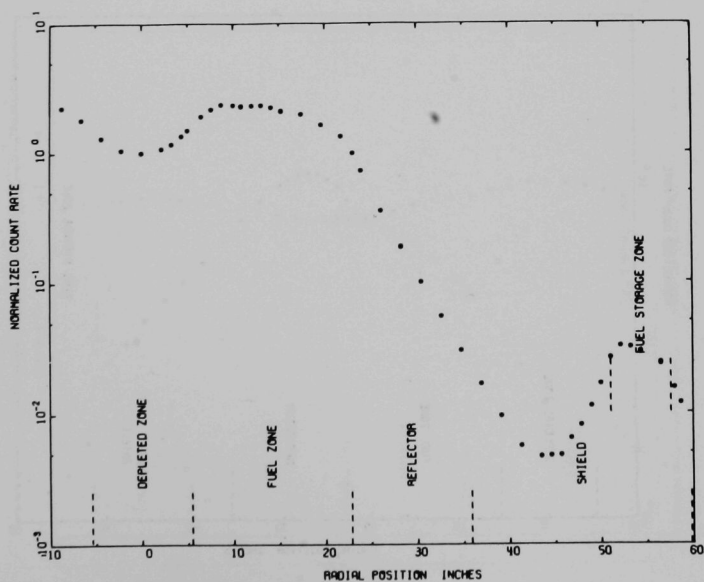


Fig. I.A.41. Traverse with U-238 Counter at 14-in. Axial Position with Fuel in Fuel-storage Area

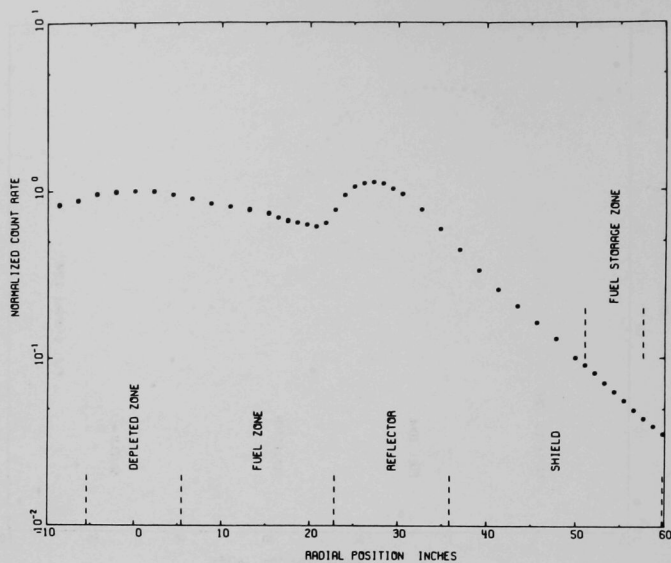


Fig. I.A.42. Traverse with Pu-239 Counter at 14-in. Axial Position without Fuel in Fuel-storage Area

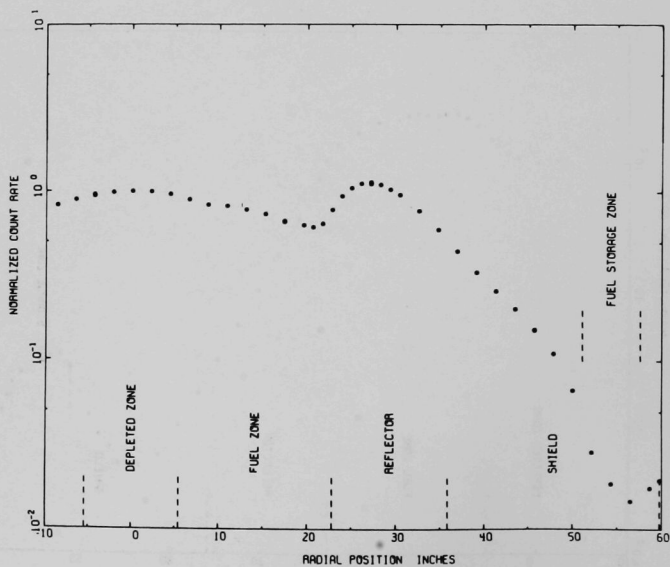


Fig. I.A.43. Traverse with Pu-239 Counter at 14-in. Axial Position with Fuel in Fuel-storage Area

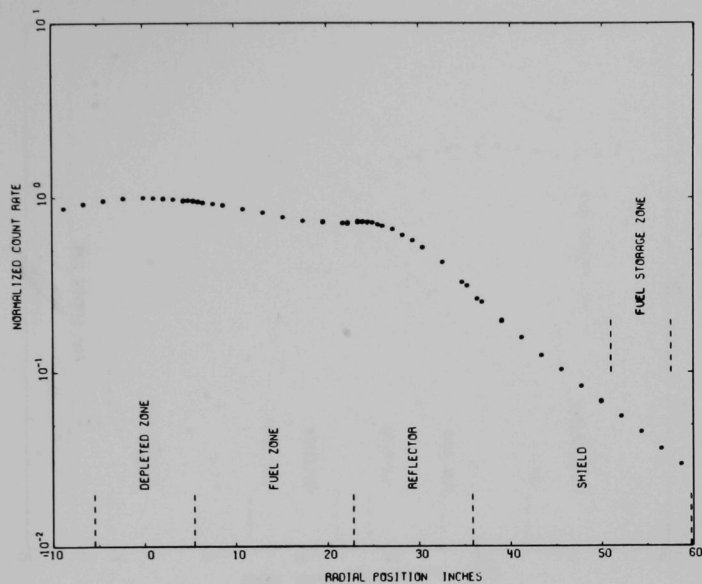


Fig. I.A.44. Traverse with BF_3 Counter at 22-in. Axial Position without Fuel in Fuel-storage Area

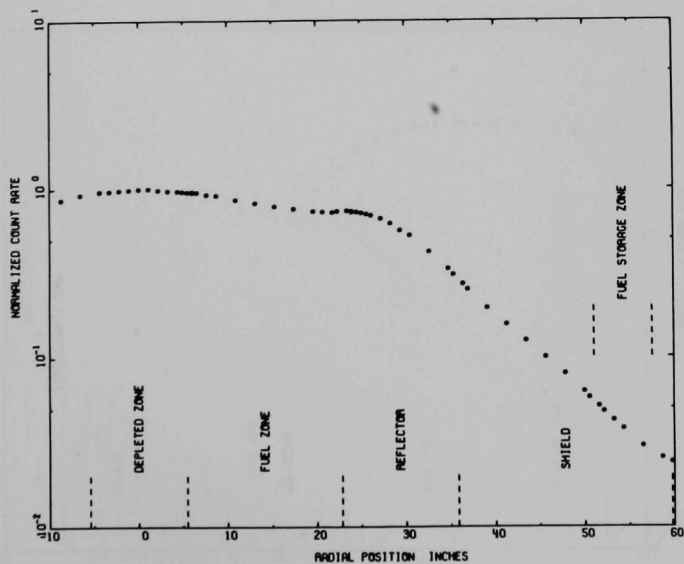


Fig. I.A.45. Traverse with BF_3 Counter at 22-in. Axial Position with Fuel in Fuel-storage Area

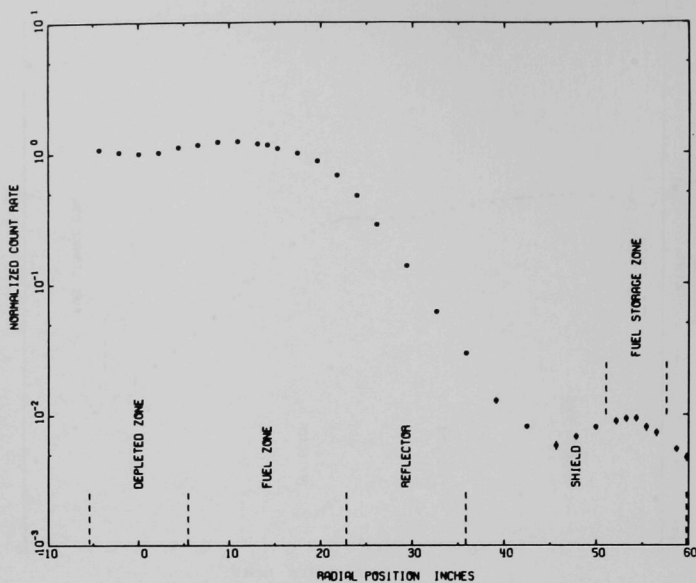


Fig. I.A.46. Traverse with U-238 Counter at 22-in. Axial Position
with Fuel in Fuel-storage Area

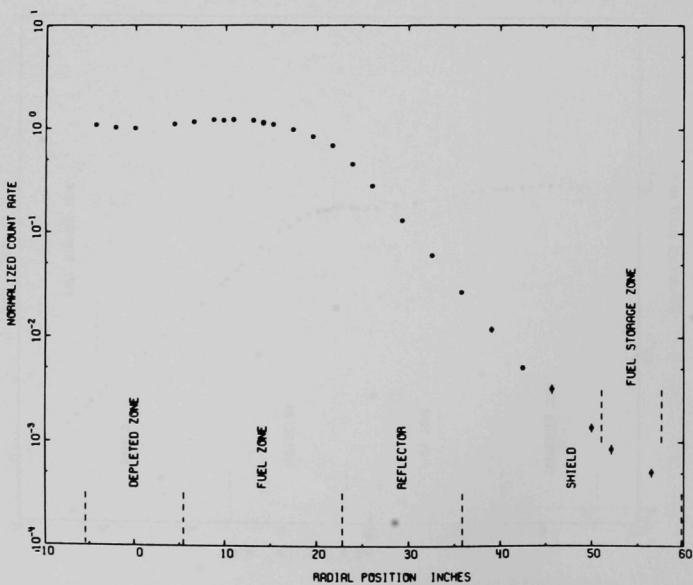


Fig. I.A.47. Traverse with U-238 Counter at 22-in. Axial Position
without Fuel in Fuel-storage Area

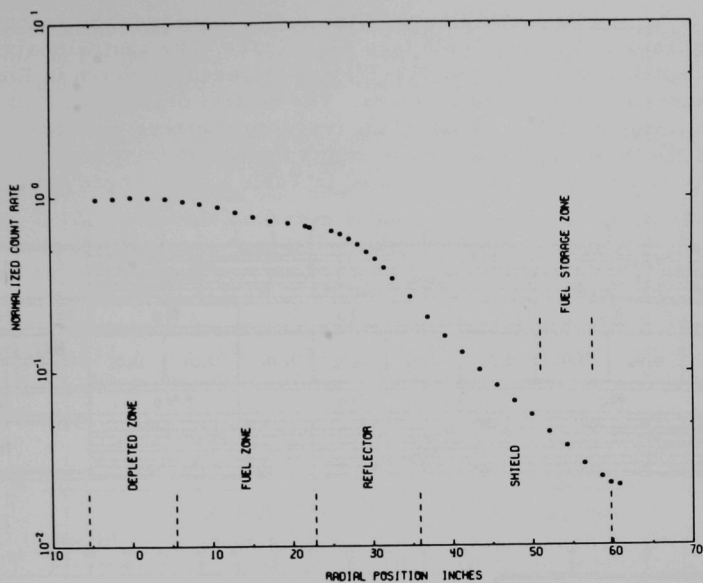


Fig. I.A.48. Traverse with Pu-239 Counter at 22-in. Axial Position without Fuel in Fuel-storage Area

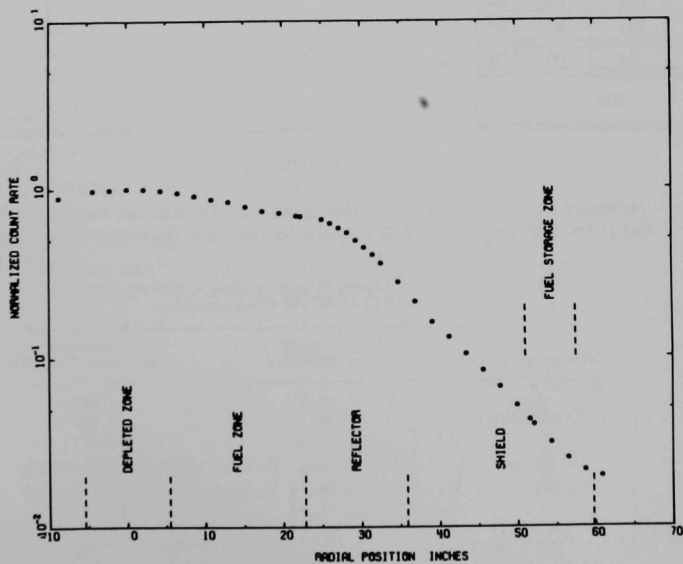
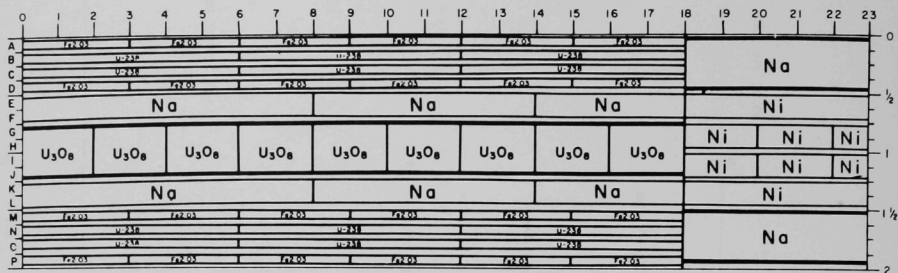
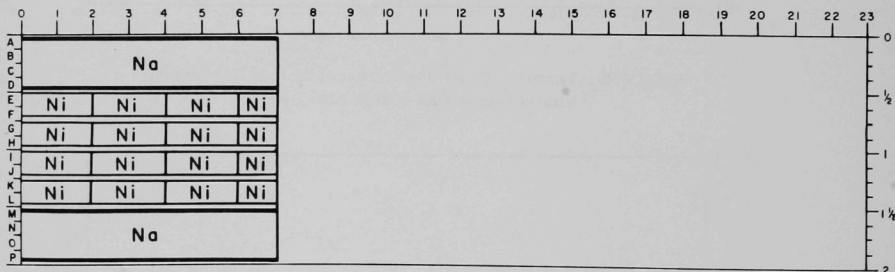


Fig. I.A.49. Traverse with Pu-239 Counter at 22-in. Axial Position with Fuel in Fuel-storage Area

Upon completion of the radial traverses the reactor loading was returned to Loading 1-120 (see ANL-7632). The central matrix element in the depleted zone (137 and 237-37) was reloaded as shown in Fig. I.A.50 to accommodate the traverse counters. The central drawers in Half 2 were the mirror image of Half 1. Each of the traverse counters was then loaded at each of the three axial positions at which the radial traverses were made. The "Axial Traverse" data are listed in Table I.A.7. These data, to provide



(a) Front Drawer



(b) Back Drawer

Fig. I.A.50. Depleted-core-zone Central Drawers Accommodating Traverse Counters for Axial Normalization of Radial Traverse Data in ZPPR/FTR-2 Shield Configuration. Columns G-J contain 1-in.-high material.

TABLE I.A.7. Axial Traverse with Radial Traverse Counters
(ZPPR/FTR-2 Shield Configuration)

Traverse Counter	r, Z^a (in.)	Normalized Count Rate ($\pm 0.6\%$)
BF ₃ (RSN 210S)	0, 3	1.000
	0, 14	0.847
	0, 22	1.377
Pu-239 (No. 76)	0, 3	1.000
	0, 14	0.808
	0, 22	1.093
U-238 (No. 114)	0, 3	1.000
	0, 14	0.619
	0, 22	0.216

^a r = radial distance from center of core; Z = axial distance from axial centerplane of core.

an axial normalization, were considered necessary due to the extended time period over which the radial traverses were run and because changes in the traverse counter electronics had been made within this period.

(ii) Shield Counter Experiment. To provide the analyst with data concerning the origin of the neutron flux in the outer region of the shield, the effect of replacing the outer shield column (the number 10 column in Loading 1-120, with void) and then replacing the shield column (for an axial depth of 18.036 in.) in both halves with B_4C was measured by determining the change in the count rate of a Pu-239 spherical fission counter (BTB) located 1 in. from the axial midplane in 137-11. The composition of the Pu-239 counter was Pu-239, 94.414 wt %; Pu-240, 5.264 wt %; Pu-241, 0.307 wt %; Pu-242, 0.016 wt %. Table I.A.8 gives the composition of the substitutions and the results.

TABLE I.A.8. Composition for
Shield Counter Experiment

Nuclide	B_4C Substitution ^a (atoms/b-cm)	Shield Removed ^b (atoms/b-cm)
C	0.01795	
Fe	0.008709	0.004107
Ni	0.001146	0.0005130
Cr	0.002501	0.001183
Mn	0.0002002	0.0001065
Mo	0.0000168	0.0000118
B-10	0.01387	
B-11	0.05624	

^a B_4C substituted for ± 18.036 in., measured from assembly midplane. The remaining matrix tube loaded with shield composition. This represents 14.8 vol % SS, 64.87 vol % B_4C , and 20.33 vol % void.

^bEntire matrix tube voided. Composition represents that of matrix tube alone.

Results

<u>Condition</u>	<u>Normalized Count Rate</u>
Shield material in column 137-10	1.000
Shield material out of column 137-10	0.932
B_4C substituted for shield material in column 137-10	0.447

(iii) Subcritical Count Data. Starting with Loading 1-120 the boron control ring was installed in the reactor. Plutonium plates were then substituted for the depleted-uranium plates in the center depleted zone of the reactor. The subcritical counter data given in Table I.A.9 was obtained as the loading changes of Table I.A.10 were made. The resulting loading, 1-154, is shown in Fig. I.A.51.

(iv) Central Fission Ratios. Central fission ratios were measured in Loading 1-154 in Position 136-37 and/or 238-37, corresponding to the heavily loaded drawer measurements of Assembly 56B (see Progress Report for April-May 1969, ANL-7577, p. 35). The preliminary data, pending reconfirmation of the thermal calibration of the back-to-back fission counters, are listed in Table I.A.11. The drawer loadings for the counter are shown in Fig. I.A.52.

TABLE I.A.9. Subcritical Count Data for Return to Loading 1-70 + Shield (Loading 1-154)

Loading No.	k_{ex} (%Δk/k)	Fission-chamber Data ^a (c/sec)			Operational-chamber Data ^b				
		132-22	126-47	137-52	Ch. 7 (A)	Ch. 8 (A)	Pico (A)	BF3-2 (c/sec)	BF3-3 (c/sec)
150	-	117.1	106.0	86.5	0.295 (-10)	0.410 (-10)	0.113 (-10)	573.8	108.0
151	-	160.1	147.7	119.9	0.410 (-10)	0.550 (-10)	0.152 (-10)	818.4	150.4
152	-	247.0	232.9	185.3	0.645 (-10)	0.850 (-10)	0.237 (-10)	1318	237.5
153	-	721.0	672.0	545.6	0.192 (-9)	0.268 (-9)	0.688 (-10)	3854	695.8
154 ^c	-0.004	93070	87248	36375	0.350 (-7)	0.480 (-7)	0.127 (-7)	-	-
	-0.523	968.5	906.8	717.7	0.259 (-9)	0.349 (-9)	0.908 (-10)	-	-

^aU-235 fission chambers manufactured by Westinghouse. Model 6376 located in matrix positions 132-22 ($r = 87.68$ cm) and 126-47 ($r = 84.14$ cm). Model 6376A located in 137-52 ($r = 82.79$ cm). Front of chambers aligned with reactor axial midplane. Data monitored for time intervals yielding $\leq 1\%$ counting statistics.

^bThe Pico, Ch. 7 and Ch. 8 are B-10-lined ionization chambers. The Pico is located in matrix position 136-55 ($r = 99.52$ cm), and Ch. 7 and 8 located at the corners of the halves at a radius of 161.49 cm. The front of all three chambers are aligned with the reactor axial midplane. The BF₃ chambers are located in the assembly immediately behind the axial reflector: BF₃-2 in matrix position 137-37 and BF₃-3 in 148-48.

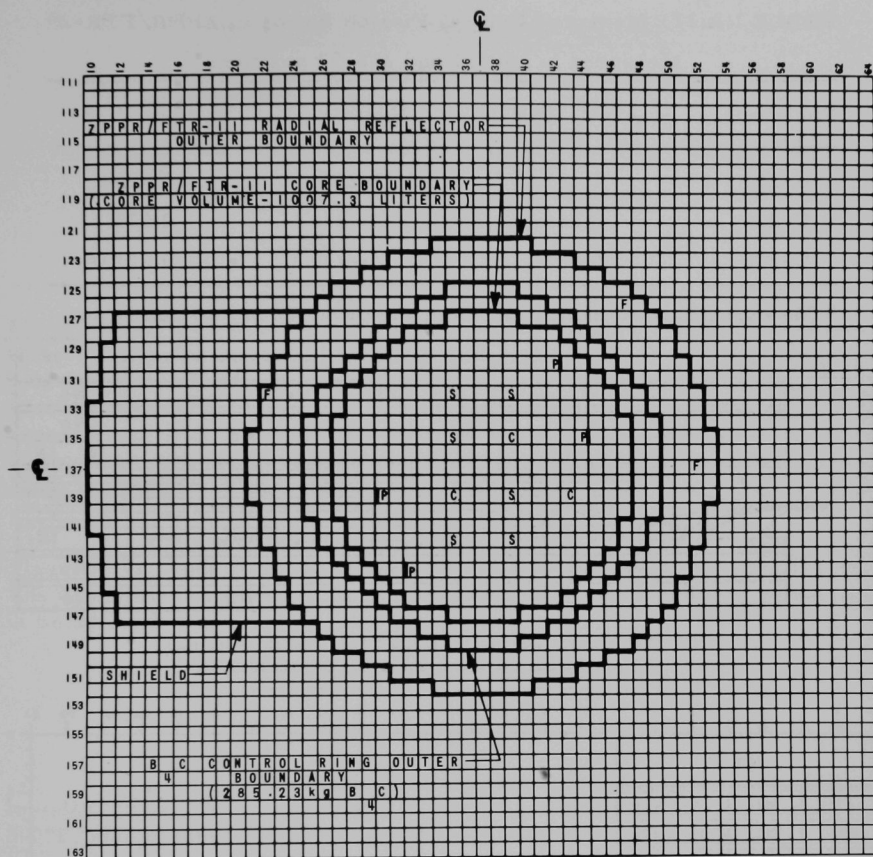
^cCriticality was achieved on Loading No. 154. The two degrees of subcriticality were achieved by manipulation of the control rods.

TABLE I.A.10. Return to Loading 1-70 + Shield
(Loading 1-154)

Loading No.	Substituted Pu for Depleted Uranium ^a (Matrix Position)	Total Fissile Mass ^b in Assembly (kg)
150	Reference (B ₂ C control ring installed)	498.073
151	136-35, 136-39, 138-35, 138-39 & 139-38	507.063
152	135-37, 137-35, 137-39 & 139-37	515.054
153	136-36, 136-37, 136-38, 138-36, 138-37 & 138-38	522.799
154	137-36, 137-37 & 137-38	527.041

^aOnly Half-1 positions are listed. Substitutions were made in the mirror-image positions of Half 2 on each loading.

^bPu-239 + Pu-241 + U-235.



ZPPR HALF I

(HALF 2 IS A MIRROR IMAGE OF HALF 1)

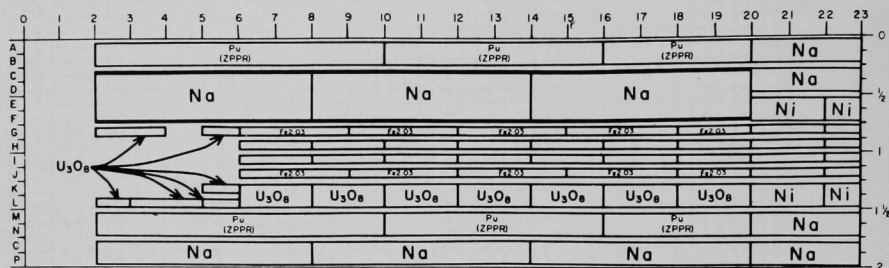
S = SAFETY ROD C = CONTROL ROD P = DRAWER ADJACENT TO POISON SAFETY ROD
 I = POISON SAFETY ROD (WITHDRAWN DURING OPERATION)
 F = U-235 FISSION CHAMBER (FRONT OF CHAMBER AT REACTOR MIDPLANE. NO F'S IN HALF 2)

Fig. I.A.51. ZPPR/FTR-2 Loading 1-154. (Ldg 1-154 equals ZPPR/FTR-2 Reference Ldg 1-70 plus Shield.)

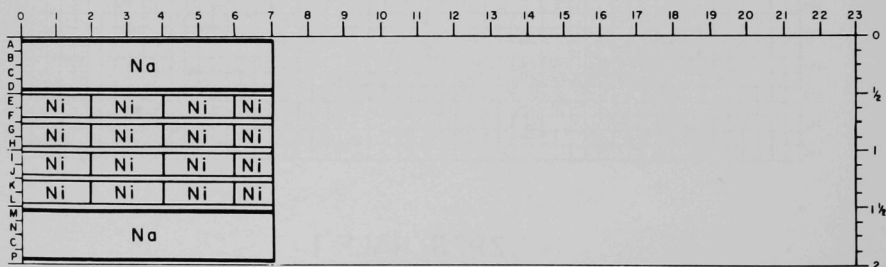
TABLE I.A.11. Measured Central Fission Ratios in ZPPR/FTR-2^a
Measured in 136-37 and 238-37 positions

Nuclide (i)	$\bar{\sigma}_f^{(i)} / \bar{\sigma}_f^{(U-235)}$	Nuclide (i)	$\bar{\sigma}_f^{(i)} / \bar{\sigma}_f^{(U-235)}$
U-233	1.465	U-238	0.0294
U-234	0.204	Pu-239	0.973
U-236	0.0621	Pu-240	0.227

^aThe experimental uncertainty is in the order of $\pm 1\%$ for all ratios.



(a) Front Drawer. Columns H and I, 6-23 in., Contain 1-in. High 45% Al. Columns G and J, 20-23 in., Contain 100% Al.



(b) Back Drawer. Columns G-J Contain 1-in. High Material.

Fig. I.A.52. Central Core Drawers Accommodating Fission Chambers for Central-fission-ratio Measurements in ZPPR/FTR-2 Reference Loading plus Shield (Ldg 1-154).

B. Component Development--LMFBR

1. Instrumentation and Control

a. Instrumentation Development for Instrumented Subassembly

(i) Instrumented-Subassembly Flowmeters (G. A. Forster)

Last Reported: ANL-7632, p. 31 (Oct 1969).

(a) Procurement of Mark-III (Sodium-calibratable)

Flowmeters. Two contracts have been negotiated, one for four flowmeters with delivery due August 21, 1970, the other for two units with delivery due July 27, 1970. Both contracts will be monitored according to the quality assurance plan developed to ensure delivery of quality instruments. ANL experienced no difficulty in fabricating one EBR-II Mark-III flowmeter in accordance with the specifications, drawings, and detailed assembly procedures that are part of the two contracts.

(b) Modifications of Calibration Loop for Mark-III

Flowmeters. Modifications are complete, and the system is being tested. The operating temperature is limited to 800°F because an older dump tank is being used temporarily.

(c) Calibration of Mark-III Flowmeters

Not previously reported.

The Mark-III flowmeter fabricated at ANL has been installed in the calibration loop. It will be calibrated at temperatures to 800°F, then cleaned for use in the EBR-II Instrumented Subassembly Test 3.

b. FFTF Instrumentation (R. A. Jaross)

(i) In-Core Flowmeter (T. P. Mulcahey)

Last Reported: ANL-7640, pp. 25-30 (Nov 1969).

(a) Tests of Model Probe-type Eddy-current Flowsensors.

Stability tests have been performed in an oven with Probes X-3, X-4, X-5, SSX-6, X-7, and X-8. Table I.B.1 gives the coil details for these probes, all of which have one primary coil and two secondary coils. The use of a Type 304 stainless steel bobbin in Probe SSX-6 is to show that Inconel-600 exhibits a transition region near 380°F.

The quality factor, Q_f = Instability in mV rms/
Sensitivity in mV rms-ft/sec, defined as the ratio of instability to sensitivity

or the percent of sensitivity that represents instability, is a term used to compare the various probes. The following data from a set of three test runs for each probe show the comparison:

$$\text{X-3: } Q_f = \frac{0.1}{0.771} \times 100 = 13\%;$$

$$\text{X-4: } Q_f = \frac{0.1}{0.44} \times 100 = 22.8\%;$$

$$\text{X-5: } Q_f = \frac{0.021}{0.041} \times 100 = 51.3\%;$$

$$\text{X-7: } Q_f = \frac{0.75}{0.442} \times 100 = 170\%;$$

$$\text{X-8: } Q_f = \frac{0.1}{0.27} \times 100 = 37\%.$$

TABLE I.B.1. Details of Coils Tested

Coil No.	Size of Primary Coil	Size of Each Secondary Coil	No. of Primary Turns/Coil	No. of Secondary Turns/Coil	Wire Type and Size	Bobbin Material
X-3	1/8 in. deep 1/2 in. wide	1/8 in. deep 1/2 in. wide	235	232	Copper-Fiberglass, AWG #30	Inconel-600
X-4	1/8 in. deep 1/2 in. wide	1/8 in. deep 1/2 in. wide	138	137	Copper-Fiberglass, AWG #26	Inconel-600
X-5	1/8 in. deep 1/2 in. wide	1/8 in. deep 1/2 in. wide	55	55	Copper-heavy Formvar, AWG #20	Inconel-600
SSX-6	1/8 in. deep 1/2 in. wide	1/8 in. deep 1/2 in. wide	239	239	Copper-Fiberglass, AWG #30	Type 304 SS
X-7	1/8 in. deep 1/2 in. wide	1/8 in. deep 1/4 in. wide	240	119	Copper-Fiberglass, AWG #30	Inconel-600
X-8	1/8 in. deep 1/4 in. wide	1/8 in. deep 1/4 in. wide	117	117	Copper-Fiberglass, AWG #30	Inconel-600

From these results it appears that X-3, with the smallest wire and largest coil cross section, makes the best combination; however, when one considers the nature of the fiberglass insulation, a definite conclusion cannot be formed at this time. All the bobbins except X-5 will now be rewound with the appropriate size of heavy Formvar-insulated copper wire. It recently has been proven, with X-5, that short-term tests with Formvar can be made to 600 or 700°F. Later tests will probably include several bobbins rewound with ceramic-coated nickel-clad silver wire at 1200 or 1400°F.

Bobbin SSX-6 proved the anomaly of the Inconel-600 bobbins. This probe compares physically with X-3 and exhibited approximately

the same stability as X-3. Because of precipitation at the surface at elevated temperatures, Type 304 stainless steel was ruled out early.

(b) Tests of Model Probe-type Permanent-magnet Flowsensors. Major effort was placed on preparation of specifications for procurement of a Type-A flowsensor from a commercial source for testing in the CAMEL Loop.

Flowsensor A-4-0 was made using an Alnico-8 magnet (see Progress Report for October 1969, ANL-7632, p. 32). Although this flowsensor exhibits better sensitivity than Flowsensor A-4, we believe that an appreciable amount of magnetic flux is lost in the gaps formed by the slots in the magnet. Therefore, a compromise between the shape of the magnets of Flowsensors A-4 and A-4-0 is being included in the procurement specifications.

Test results for Flowsensor A-4-0 are shown in Fig. I.B.1. Figures I.B.2 and I.B.3 show data from tests of Flowsensor A-4 in the CAMEL Loop at 325 and 1200°F after the Alnico-8 flowsensor magnet had been temperature-stabilized at 1300°F for operation at 1200°F. For a sodium-flow velocity of ~8.2 ft/sec, the output signal at 1200°F decreased ~11.5% from what it was at 325°F. Extrapolation of the data in Fig. I.B.3 indicates that an output signal of ~7.75 mV at a flow velocity of 16.2 ft/sec at 1200°F will be produced by Flowsensor A-4.

c. EBR-II In-Core Instrument Test Facility (E. Hutter)

(i) Preliminary Study of Various Schemes (O. S. Seim and R. H. Olp)

Last Reported: ANL-7640, pp. 31-32 (Nov 1969).

Two types of handling containers--the straight type and the reel type--for installing and removing test sensors from the reactor core region have been considered. The straight type of handling container would be used to install and remove the 36-ft-long, rigid, inner sensor thimble assembly. It consists of a 42-in.-long, lower shielded coffin section, a straight 10-ft-long center section, and a straight 21-ft-long upper section. The reel type of handling container would be used with the flexible sensor leads. It consists of the 42-in.-long, lower shielded coffin section and a reel assembly which would loop the leads into a coil as they are withdrawn from the thimble for periodic recalibration and subsequent reinsertion into the core for continued testing. With the reel type of container, a rather complex operational procedure is required when inserting flexible sensor leads into the core.

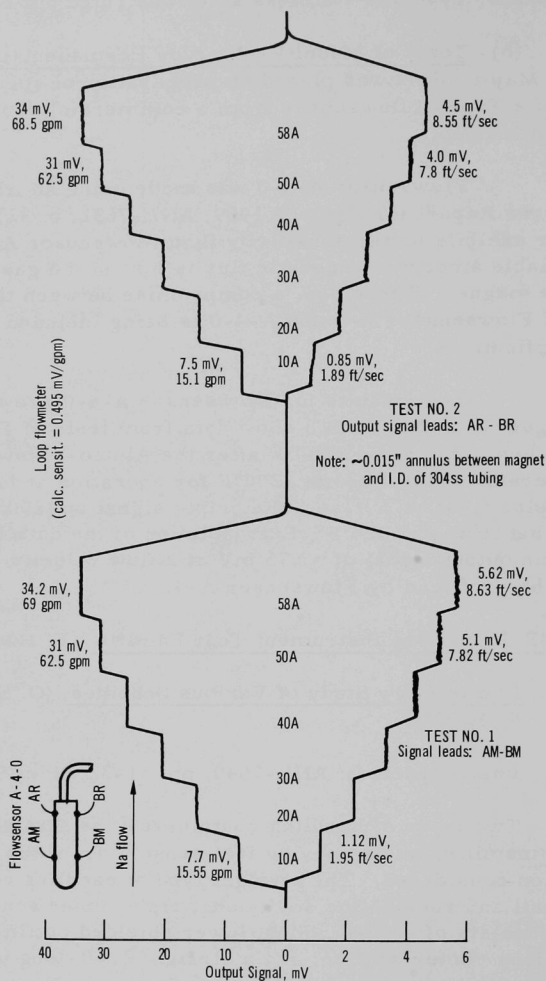


Fig. I.B.1. Tests of Permanent-magnet Flowsensor A-4-0 at 390°F in the 2-in. Schedule-40 Pipe Test Section of the Modified Annular Induction Pump Loop

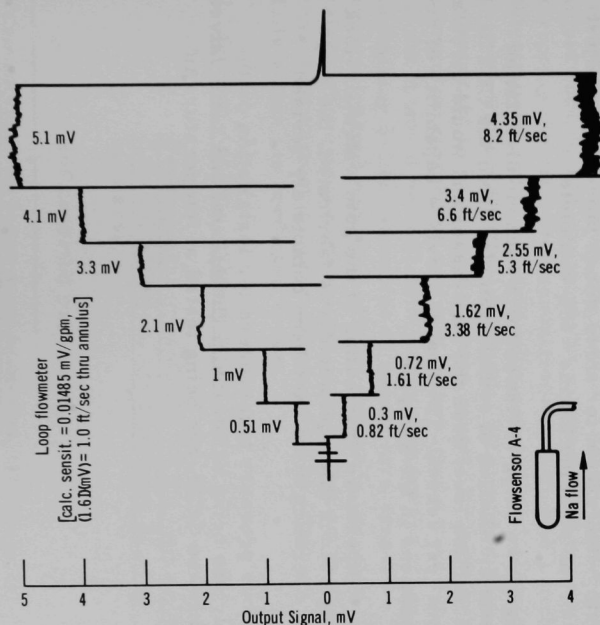


Fig. I.B.2. Test of Permanent-magnet Flowsensor A-4 at 325°F in the 4-in. Schedule-10 Pipe Test Section of the CAMEL Loop. The magnet was temperature-stabilized at 1300°F for operation at 1200°F.

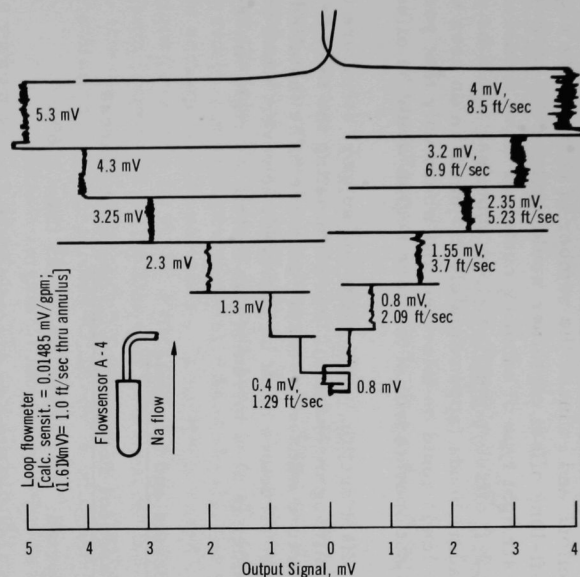


Fig. I.B.3. Test of Permanent-magnet Flowsensor A-4 at 1200°F in the 4-in. Schedule-10 Pipe Test Section of the CAMEL Loop. The magnet was temperature-stabilized at 1300°F for operation at 1200°F.

A new concept has evolved which simplifies the conversion between handling functions and reduces the number of components required. In this concept, a 10-ft-long offset container would replace the 10-ft-long center section of the straight type of handling container when flexible leads are to be handled. A 2-ft offset in the 10-ft-long container would be provided by two large-radius bends (approximately 25° each) in an area where bending of the sensor leads could be tolerated and where only that portion of the leads which do not operate within the core region would be affected.

The offset section would clear the support structure of the reactor-vessel cover-lifting mechanism, thus eliminating the need to remove the support structure whenever sensor leads are to be installed or removed. (The support structure must be removed, however, when the straight type of container is used to remove or install the rigid inner-thimble assembly.)

2. Fuel Handling, Vessels and Internals

a. Core Component Test Loop (CCTL) (R. A. Jaross)

Last Reported: ANL-7640, pp. 32-33 (Nov 1969).

(i) Loop Modifications to Accommodate Second FFTF Subassembly. Work on the pump-bypass piping and the 4-in.-flowtube installation has been completed except for some minor pipe-hanger adjustments. Modification of the plugging loop is ~40% complete.

Designs are being reviewed for a vacuum-distillation sampler for the on-site distillation of sodium samples from the CCTL. The unit would be located at floor level near the test vessel and would circulate sodium from and to the test vessel. The design provides capability of exposing materials specimens in the sampler.

High-temperature dry-testing of the gate-valve air-lock assembly is continuing. Since this equipment was fabricated, the valve-support structure and operating stem have been completely revised.

The four pressure transducers for installation on the Mark-II fuel assembly are being calibrated. The 1/2-in. and 2-in. valves of the types installed in the CCTL are being tested at temperature in sodium.

C. Sodium Technology

1. Sodium Chemistry

- a. Determination of the Solubility of Gases in Liquid Sodium
(F. Cafasso and E. Veleckis)

Last Reported: ANL-7618, pp. 21-22 (Sept 1969).

(i) Xenon Solubility in Sodium. The inclusion of isotopic mixtures* of xenon in gas-bonded fuel elements is being evaluated at EBR-II as a means of locating fuel failures in LMFBRs (see Progress Report for November 1969, ANL-7640, pp. 53-57). Xenon escaping from failed fuel passes through the sodium coolant and enters the cover gas, which can be analyzed by a mass spectrometer. Accordingly, the solubility of xenon in liquid sodium is of importance. Calculations based on a solution model developed recently by H. M. Feder and E. C. Schynders under a different program (supported by the Division of Research) indicate that this solubility is so low that it will not limit the sensitivity of the proposed detection method. Substantiation of the predicted solubility is being sought by experiment.

Measurements of xenon solubility in liquid sodium will be made with existing apparatus. The technique to be used proved successful in our previous determinations of the solubilities in sodium of argon and helium (see ANL-7618, pp. 21-22). The technique involves saturating liquid sodium with xenon gas at a preselected temperature and pressure, stripping the dissolved xenon from sodium with a helium sparge, trapping the stripped xenon on liquid-nitrogen-cooled Molecular Sieves, transferring it to a bulb, and finally assaying it. The amount of xenon in the gas sample is expected to be in the nanomole range. Because gas chromatography is a convenient method of analysis, experiments were run to determine whether or not it would be sufficiently sensitive for the xenon analyses. Gas samples containing 5-100 nanomoles of xenon were assayed with a Beckman GC-5 gas chromatograph equipped with an ionization detector. Elution peaks were obtained whose area varied linearly with xenon concentration. Thus, it appears that gas-chromatographic analysis will be adequate if the xenon solubility falls within the predicted range.

2. Sodium Analytical Development

- a. Development of Methods for the Determination of Oxygen, Carbon, Nitrogen, and Hydrogen Species (R. J. Meyer and M. Barsky)

Not reported previously.

*Chemical Engineering Division Annual Report--1968, ANL-7575, pp. 105-111 (April 1969).

The purpose of this work is the development of standard chemical and instrumental methods for determining oxygen, carbon, nitrogen, and hydrogen species in sodium, as well as the total content of each of these so-called interstitial elements.

(i) Evaluation of Ion Microprobe Mass Analyzer. Applied Research Laboratories (ARL) has developed the Ion Microprobe Mass Analyzer (IMMA), an instrument with potential application for the microanalysis of contaminant species in sodium. Sample atoms are ionized by a finely focused ion beam that impinges on the surface of the solid sample. The sample ions are collected and mass analyzed in a mass spectrometer.

The applicability of the IMMA to sodium is being examined. Two samples were submitted to ARL: one was EBR-II secondary sodium, the other sodium containing sodium cyanide. The results from these samples enable evaluation of the IMMA.

(ii) Techniques for Sodium Removal. Species of the interstitial elements in sodium are generally present in the ppm to ppb range. To simplify their identification by chemical methods, some degree of concentration is necessary. This can be accomplished by separation of the sodium. The various techniques that have been used for sodium removal are distillation, amalgamation, reaction with water, and reaction with liquid ammonia. Of these, amalgamation is the only one that furnishes direct information about hydrogen species; it may also yield information about oxygen and carbon species. Hence, an effort is now under way to evaluate this technique for these species.

b. Analytical Methods for Metallic and Halide Impurities in Sodium
(R. J. Meyer and H. Edwards)

Not previously reported.

A knowledge of the metallic and halide impurity content of sodium systems is important in evaluating corrosion and in detecting the presence of fuel or fertile materials in sodium. The determination of trace metals in sodium by atomic absorption measurements on distillation residues* has been carried out at EBR-II with considerable success. Standardization of this method is now being undertaken at ANL-Illinois as part of our program to certify analytical methods related to sodium technology. A distillation apparatus similar to the one at EBR-II is being assembled and will be tested shortly.

Research is also under way on the development of a rapid survey method for trace metals in sodium. The atomic absorption method

*Ramachandran, T. P., and Hareland, W. E., The Determination of Trace Metallic Impurities in Reactor Sodium, presented at the 13th Conference on Analytical Chemistry in Nuclear Technology, Gatlinburg, Tennessee (Sept. 30-Oct. 2, 1969).

mentioned above is slow because only one element at a time can be analyzed. Substitution of methods such as X-ray fluorescence or emission spectroscopy would permit the simultaneous determination of many metals in the distillation residues, and so such modifications are being explored. In addition, a paper study on the feasibility of direct determination of trace metals in sodium is being made.

c. Sampling and Analysis of Cover Gas for Fission Products
(R. J. Meyer and S. Skladzien)

Not reported previously.

The objective of this work is to develop analytical techniques and on-line monitors for the identification and radioassay of fission products in the cover gas of an operating LMFBR. Surveillance of these fission products is important with respect to the detection and identification of failed fuel elements, and the release of gaseous radioelements into the atmosphere.

The methods in use at EBR-II to monitor cover gases for radioactive xenon, krypton, cesium, rubidium, iodine, bromine, and tritium are being evaluated. For tritium, this has led to the following conclusions:

(1) The primary reason for monitoring and controlling tritium is radiological safety, since tritium is not expected to be useful in or interfere with fuel-failure detection and identification.

(2) Because tritium is a weak beta emitter, it presents no radiation hazard unless ingested or inhaled. Hence, accurate assays of the contained cover gas are unnecessary. However, the tritium content of gases that may be released to the atmosphere is of utmost importance.

(3) The methods of sampling gases before releasing them to the atmosphere via the stack are judged to be reliable for EBR-II and should be applicable to FFTF and subsequent LMFBRs. Therefore, at the present time ANL plans no additional development work on tritium analysis in the EBR-II system.

3. On-line Monitors

a. Evaluation and Improvement of Oxygen-activity Meter
(J. T. Holmes)

Last Reported: ANL-7618, pp. 22-23 (Sept 1969).

A cooperative program between Brookhaven (BNL), Pacific Northwest (PNL), and Argonne (ANL) has been arranged to improve the

on-line electrochemical meter originally developed by United Nuclear Corp. (UNC) for the measurement of oxygen activity in liquid sodium. BNL has the responsibility of developing a second-generation oxygen meter, including the sensor, housing, and electronics package, to a point of commercialization. PNL has the task of developing and supplying improved electrolytes for BNL use. ANL is responsible for defining the requirements of the meter, for developing an oxygen-activity station (the station being the meter plus auxiliary on-line equipment for calibration and checking of meter response), and for planning and carrying out tests on the BNL-developed meter(s).

The improved oxygen meters prepared by BNL will be field-tested on the Radioactive Sodium Chemistry Loop (RSCL), which is now under construction at EBR-II. These tests will provide (1) the first on-line oxygen-monitoring equipment for EBR-II, (2) information on whether or not beta and gamma radiation affect operation of the meter, and (3) experience in adapting and maintaining this type of instrumentation for LMFBR conditions.

The commercially available UNC oxygen cell operates at 600 to 700°F with a solid electrolyte of thoria-15 wt % yttria and a Cu-Cu₂O reference electrode. The voltage of the cell depends on the difference in oxygen potential between the reference electrode and the oxygen-bearing contaminants in the sodium under analysis. Field tests of the UNC meter in sodium loops at many sites have indicated that it can be used to monitor oxygen in sodium continuously at concentrations above 0.1 ppm. However, there are still problems associated with its use, such as (1) uncertain lifetime, often very short (days or weeks), owing to fracture of the electrolyte, (2) low tolerance to thermal shock, (3) unstable and often nonreproducible calibration, (4) sensitivity to ambient temperatures, and (5) restriction to operation at low temperatures. The development program being carried out at BNL gives indication that most of the difficulties associated with the UNC meters can be overcome. The BNL meters will eventually have an improved solid electrolyte, a gas reference electrode, and improved electronic-readout instrumentation.

Before being installed on the RSCL at EBR-II, the BNL meters will be tested and calibrated at ANL-Illinois. A small facility with circulating sodium is now being modified for this purpose. The meters will be calibrated by correlating cell voltage with oxygen-in-sodium concentration as determined by such methods as distillation sampling and analysis of the residue, equilibration and analysis of refractory metal wires, and oxidation rate of uranium foil. The on-line calibration and response-checking procedures to be used at EBR-II will be developed during ANL's program of testing meters.

Quality assurance information on materials of construction for the meter and on fabrication procedures is now being compiled. This information will be forwarded to BNL in January 1970 for their use in making the prototype meters for the EBR-II field tests. The present schedule calls for shipment of these prototype oxygen meters to ANL-Illinois by the end of FY 1970.

4. Materials Compatibility

a. Candidacy of Vanadium-base Alloys for Cladding LMFBR Fuels (T. F. Kassner and D. L. Smith)

Last Reported: ANL-7640, pp. 37-38 (Nov 1969).

(i) Distribution Coefficients of Impurities in Sodium-Metal Systems. This work continues the investigation into the effect of chromium additions to vanadium on the activity and solubility of oxygen in vanadium. Some preliminary results have been obtained on the distribution of oxygen between liquid sodium and vanadium alloys containing 10, 15, and 20 wt % chromium. The experimental method was similar to the equilibration technique previously used to determine the solubility of oxygen in vanadium. However, the oxygen content of the sodium was insufficient to saturate the alloy. Vanadium and vanadium-alloy wires were exposed simultaneously to sodium under various conditions of temperature and oxygen concentration. The results are given in Fig. I.C.1, where the oxygen concentration in the alloys is related to the oxygen concentration in vanadium.

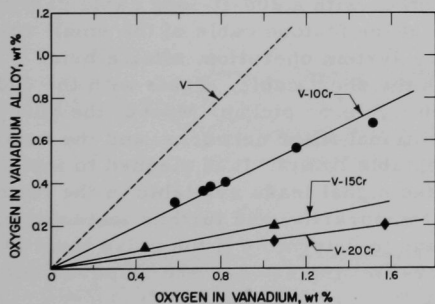


Fig. I.C.1. Oxygen Concentration in V-Cr Alloys vs Oxygen Concentration in Vanadium, after Simultaneous Exposure to Sodium

The alloys contain considerably less oxygen than the unalloyed vanadium. Moreover, the distribution coefficient for the oxygen between the alloy and sodium decreases as the chromium concentration increases. For V-20 wt % Cr, the oxygen distribution has decreased by a factor of eight. Chromium additions, therefore, would appear to improve significantly the compatibility of vanadium with cold-trapped sodium.

The effect of the chromium additions on the oxygen solubility in vanadium has not been determined yet. There is some indication that the $V_2Cr(O_{satd})$ -oxide- \underline{O}_{Na} phase boundary (i.e., the oxygen concentration in sodium at which the alloy becomes oxygen saturated) is raised. Extension of these experiments to vanadium alloys containing more than 20 wt % chromium is under way.

D. EBR-II--Research and Development

1. Equipment--Fuel Related (E. Hutter)

- a. Improved Gripper and Holddown Force-limit Devices
(W. M. Thompson, J. Pardini, and G. D. Giorgis)

Last Reported: ANL-7581, pp. 44-45 (June 1969).

The components that comprise the improved system for monitoring the forces exerted by the gripper and holddown mechanisms during fuel handling are being fabricated and tested. The improvement is being made essentially by replacing the mechanical force-calibrating components and limit switches with electronic components. In the improved system, potentiometers connected to the gripper and holddown mechanisms transmit electrical signals corresponding to the degree of spring movement resulting from applied vertical forces. An electronic-subsystem package operates in response to these signals to indicate the value of applied forces, discounting the normal force required to drive the mechanisms.

The package of electronic components for the gripper mechanism (the amplifier panel, relay panel, and combined power-supply panel) have been completed, tested, and shipped to the EBR-II site. The package was assembled completely and was tested using two linear potentiometers as input devices. Two types of tests were conducted, one with a short, direct cable from the input devices, and the other with a 200-ft-long cable carrying ac power leads to simulate conditions of the festoon cable of the small rotating plug of the reactor. Satisfactory system operation, after a brief period of debugging, was obtained with the short cable. Tests with the 200-ft cable, however, showed undesirable 60-cycle-ac pickup. Most of the 60-cycle signal was eliminated by inserting additional filter networks, and the noise conditions now seem to be within acceptable limits. It is planned to install the system using the existing unshielded signal leads available in the festoon cable. The system will be connected temporarily, and further tests during actual operating conditions will be made to determine if the noise level is acceptable before the mechanical force-limiting devices are removed and the final installation is made.

2. New Subassemblies and Experimental Support (E. Hutter)

- a. Experimental Irradiation Subassemblies (O. Seim and E. Filewicz)

Last Reported: ANL-7632, p. 46 (Oct 1969).

(i) Mark-B61B and Mark-E37A Subassemblies. The Mark-B61B and Mark-E37A subassemblies have been designed to work together as a pair

in irradiating unencapsulated fuel elements to levels at which the possibility of element failure exist. The elements can be irradiated to normal levels in the Mark B61B. Then, some of the 61 irradiated elements from the subassembly can be installed into the Mark E37A for additional irradiation to the levels of higher risk. Similar subassemblies are being designed for unencapsulated fuel elements of other diameters to extend this high-level-irradiation capability.

The Mark B61B is designed to take 40-in.-long by 0.230-in.-dia elements to normal irradiation levels. The 40-in. length was selected as the maximum for the higher-risk Mark-E37A subassembly because collection devices must be located above and below the fuel elements. The fuel elements in the Mark B61B are at the same vertical elevation as in the Mark E37A. Most other subassemblies used for normal irradiation levels use 60-in.-long elements, which occupy almost all the available space between the top end fixture and the lower adapter. One subassembly (Mark A) uses 40-in.-long elements, but they are set at the highest possible elevation in the subassembly. A few models (Mark C and the existing Mark E) use a shorter element.

Figure I.D.1 shows the general arrangement of the Mark-B61B irradiation subassembly. External dimensions are identical with those of all other driver and irradiation subassemblies. The lower adapter fits into the reactor grid-plenum assembly and accepts coolant from the high-pressure inlet plenum. An orifice plate immediately above the lower adapter is used to adjust the coolant flow to the requirements of the particular

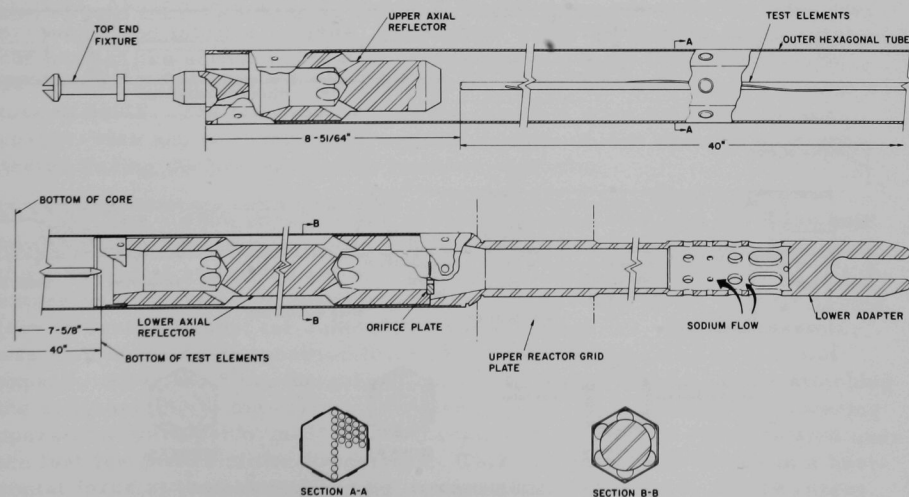


Fig. I.D.1. EBR-II Mark-B61B Irradiation Subassembly

experiment. The upper and lower axial reflectors reduce the fluence received by the permanent portions of the reactor vessel. The fuel elements extend a short distance below the core to accommodate insulating pedestals or reflector segments that may be used on fuel elements for other reactors. The top of the subassembly supports the usual end fixture used for normal fuel-handling purposes.

The Mark-E37A irradiation subassembly, shown in Fig. I.D.2, is in many respects similar to the Mark B61B. Again, the external dimensions are identical with those of all other driver and irradiation subassemblies. The lower adapter, orifice plate, outer hexagonal tube, and top end fixture are identical to those of the Mark B61B. The lower axial reflector, however, contains a collector cup to catch any element fragments which might drop downward should a minor element failure occur. Section B-B of Fig. I.D.2 shows a three-piece sectional enclosure surrounding the unencapsulated fuel elements. These sections and the surrounding filler strips direct the coolant flow through the elements and protect the outer hexagonal tube. The strips are supported on three screws, as shown in Sect. A-A. With this sectional arrangement, the interior hexagonal dimensions can be adjusted by resizing the spacer buttons prior to plug-weld fastening just above the bottom of the elements. This size adjustment, if required, would be made before the elements are inserted into the subassembly. An upper collector mounted above the elements serves as a strainer to remove particles that would obstruct reactor coolant passages if an element failed.

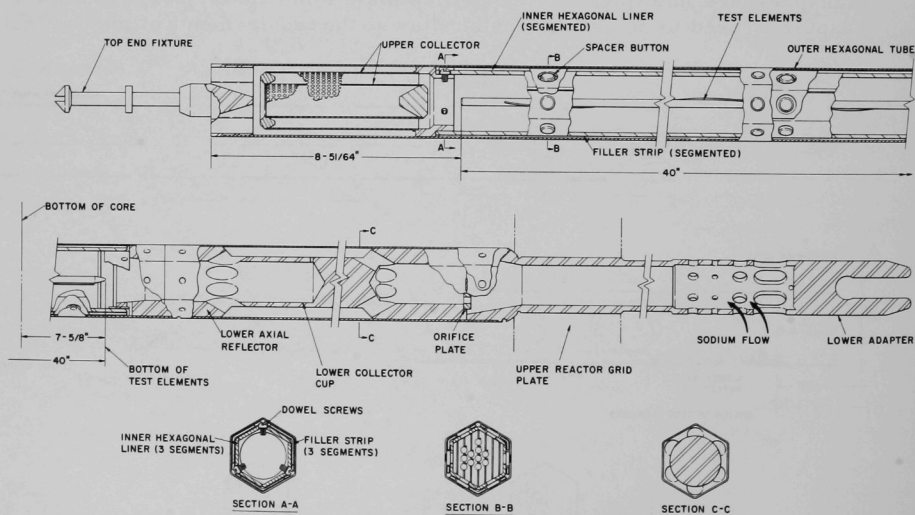


Fig. I.D.2. EBR-II Mark-E37A Irradiation Subassembly

3. Instrumented Subassemblies (E. Hutter and A. Smaardyk)

a. Test One and Two

(i) Installation (A. Smaardyk)

Last Reported: ANL-7640, p. 39 (Nov 1969).

After the leads of the Test-1 Instrumented Subassembly had been severed and its extension tube removed (while the bulk temperature of the primary sodium was 580°F), the subassembly was transferred from the reactor vessel to the fuel-unloading machine by normal fuel-handling procedures. The subassembly then was discharged from the fuel-unloading machine into an unshielded pipe for protection against the possibility of a sodium-air reaction. Subsequent examination of the severed subassembly showed that the leads had been cut cleanly and flush with the surface of the top end fitting.

The Test-2 Instrumented Subassembly, which had been shipped from Illinois to the EBR-II site in its special shipping container (see Progress Report for October 1969, ANL-7632, p. 48), was satisfactorily checked out. The lower 8 ft of the subassembly then were preheated to 600°F in a special furnace (see Progress Report for August 1969, ANL-7606, p. 42), using a prescribed preheating procedure, confirmed previously in the test-1 installation. After the preheat, the subassembly was transferred rapidly to the reactor and lowered into the sodium through the No. 6 control-rod penetration. About 4 min were required to transfer the subassembly from the preheater and into the sodium. During that time, the temperatures of the capsules in the subassembly decreased from 600°F (in the preheater) to 545°F just before entering the primary bulk sodium, which was at a temperature of 580°F. The temperatures of the capsules were indicated by four spacer-wire and two structural-capsule thermocouples that had been connected during the preheating and transfer operation.

The subassembly and its extension tube initially were held 60 in. short of the fully inserted position in the bulk sodium. At this point, the differential expansion between the internal subassembly coupling and the extension tube is compensated within the design range of the support spring (see Progress Report for June 1969, ANL-7581, p. 49). The subassembly was held at the 60-in. position for 5 hr to allow the coupling to heat and expand. After the 5 hr, the subassembly was inserted fully. After attaching the subassembly to the drive mechanism, a number of raising and lowering operations were performed. Some increase in push force was indicated over the last few inches of the downstroke. This was thought to be due to a horizontal force at the point where the upper subassembly guide sleeve enters the guide thimble.

The subassembly installation was completed, the electro-mechanical interlocks of the drive system were adjusted, and the electrical interlocks with the fuel-handling system were checked out. Approach to full reactor power of 50 MWt, conducted according to startup procedures specifically prepared for the Test-2 Instrumented Subassembly, was completed on December 18. Only one of the instrument sensors (an outlet coolant thermocouple) has failed to respond.

b. Test Three--PNL-17

(i) Hydraulic Flowtesting of the Subassembly (J. Poloncsik)

Last Reported: ANL-7618, p. 30 (Sept 1969).

Hydraulic flowtests were performed with a flow model of the Test-3 Instrumented Subassembly. Using six 0.340-in.-dia inlet orifices in the lower adapter, a flowrate of 53 gpm was obtained at a total pressure drop of 39 psig. (These values are for sodium at 800°F, and have been converted from the water measurements observed in the flow test.)

The modified grid assembly (see ANL-7618, p. 30) also was tested in the flow loop. This test ran 3 hr, and used a total pressure drop of 75 psig through the subassembly and a temperature of 150°F. After this test, visual examination showed no evidence of grid-bar deformation or weld failure, thus verifying the adequacy of the design.

(ii) Brazing the Bulkhead of the Subassembly (D. Walker)

Not previously reported.

One of three full-size sample bulkheads made to a new design was brazed with high-nickel-alloy braze (Coast Metal 60). At the brazing temperature, a gradient of 35°C was observed from one side to the other. This gradient was caused by the work not being centered in the susceptor, which had warped out of round. The susceptor must be replaced because the 35°C gradient is too great to produce a uniform brazed joint with this alloy. Coast Metal 60 has a solidus temperature of 1079°C and a liquidus temperature of 1135°C, and should be brazed at 1177°C. In the sample, the 10 sensor leads on the hot side were brazed at 1175°C and the remaining 10 on the other half of the bulkhead were brazed at 1140°C, the latter being only 5°C above the liquidus temperature. Going to a higher temperature to increase the fluidity is not practical when there is much of a gradient, because the braze alloys will become very aggressive on the hotter side and may cause failure of the sensor lead by melting through the cladding or tube wall.

Complete evaluation of this braze has not been completed; however, visually it appears very good. Figure I.D.3 shows the appearance of the sheathed thermocouples from the bottom side after brazing. Excellent braze-alloy fillets were obtained including that around the flux-monitor tube.

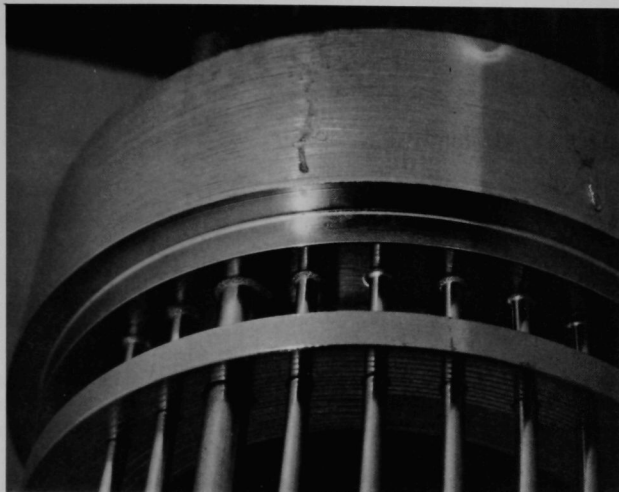


Fig. I.D.3. Closeup of Brazed Thermocouples on Bottom, or Sodium, Side of Bulkhead for Test-3 Instrumented Subassembly (2X scale)

4. Coolant Chemistry (D. W. Cissel)

a. Sodium Coolant Quality Monitoring and Control

Last Reported: ANL-7640, pp. 40-44 (Nov 1969).

(i) In-line Vacuum-distillation Sodium Sampler (W. H. Olson)

As reported in ANL-7640, pp. 43-44, a sampler designed to distill ~125 g of sodium in line has been successfully tested. The sampler is illustrated in Fig. I.D.4. The basic sections of the sampler are the still (sample cup), transfer line, condenser, and freeze trap.

The sampler is filled with sodium to some point in the freeze trap by evacuating the sampler and slowly admitting sodium at the inlet until it freezes in the trap. All internal surfaces of the still, transfer line, and condenser then are flushed thoroughly with flowing sodium while a frozen seal is maintained in the freeze trap. Sodium is drained by pressurizing with argon and melting the freeze seal. The condenser and most of the transfer line are drained to the sodium outlet line; then the remainder

of the transfer line and the upper portion of the still are drained to the inlet side. Thus, the sodium level is established in the sample cup at the tip of the inlet line. The condenser then is cooled to some temperature (210-250°F) above the melting point of sodium, the still is heated to the desired distillation temperature (650-700°F), and the sampler is evacuated to ~5 microns of mercury. After sodium has distilled to the condenser, the sampler is filled with argon. If desired, the distillate then may be drained to the outlet. The sampler is cooled to room temperature, and the sample cup is removed.

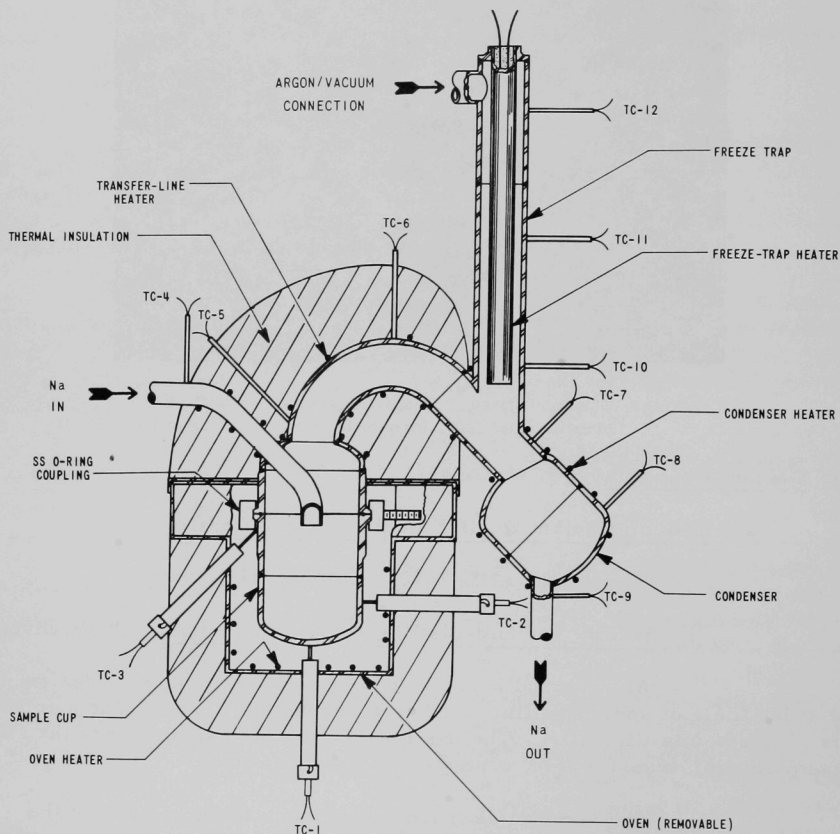


Fig. I.D.4. In-line Vacuum-distillation Sodium Sampler

(ii) Particulate Matter in the Secondary-sodium Storage Tank
(W. H. Olson)

Sodium was drained from the secondary system to the storage tank on October 19, 1969, to facilitate system maintenance and change during a scheduled shutdown of the reactor. The system was re-filled on December 6, 1969, prior to plant startup.

During the period from October 19 to December 6, several 125-g samples of sodium were taken from the storage tank and vacuum-distilled in line. The distillation residue from three of these samples was treated with aqua regia, and the acid-soluble portion was analyzed for trace metals by atomic-absorption spectrophotometry. The acid-insoluble portion of the residue was examined by emission spectrography and found to be primarily silica.

During testing of the in-line distillation unit, five samples of secondary sodium were distilled from a single cup without removing the cup between samples. At the end of the fifth distillation, the cup was removed, and the residue was examined. The residue was shiny black and rather brittle. Dispersive X-ray analysis of a portion of the residue indicated that it was amorphous. During grinding of the sample for X-ray analysis, the shiny black appearance was observed to be only on the surface. The interior of the sample appeared white. Spectrographic analysis of the residue indicated Na, Si, Mg, and Ca as major; Al and Fe as minor; and Ag, B, Cu, Mn, Pb, and Ti as trace components.

Residue of this kind has not been observed in laboratory distillation of sodium taken from the secondary system during normal operation. It is theorized that sediment in the bottom of the storage tank is stirred up in the process of draining. The sediment then slowly settles out while the sodium is stagnant in the tank. This theory is supported by the values for calcium and magnesium listed in Table I.D.1. On October 29, approximately 10 days after the secondary system had been drained to the storage tank, concentrations of calcium and magnesium were ~100 times higher than normal. By December 5, one day before the system was refilled, concentrations were nearly back to normal. The visible quantity of acid-insoluble residue from the samples also was substantially reduced between October 29 and December 5.

TABLE I.D.1. Calcium and Magnesium in Sodium
from Secondary Storage Tank

Sample Date	Ca (ppm)	Mg (ppm)
10/29/69	1.7	1.2
11/3/69	0.1	0.6
12/5/69	0.03	0.05
Normal Concentration	<0.02	0.01-0.03

Now that the secondary system has been returned to normal operation, additional samples will be taken from the system, distilled in line, and examined.

5. Experimental Irradiation and Testing (R. Neidner)

a. Experimental Irradiations

Last Reported: ANL-7640, pp. 44-46 (Nov 1969).

Table I.D.2 shows the status of the experimental subassemblies in EBR-II as of December 15, 1969.

Two new experimental subassemblies were loaded into the reactor for the Run-39A startup: XO72, containing ANL Series 0-3 mixed-oxide capsules; and XO73, containing PNL Series 6 unencapsulated mixed-oxide elements. Also loaded was XO12A, a reconstituted subassembly containing NUMEC mixed-oxide capsules.

Subassemblies XO33 and XO44, which had completed their scheduled irradiations, were removed and sent to the FCF. Subassembly XO62, which was adjacent to the instrumented subassembly, was removed to the storage basket for Run 39A only. Another experimental subassembly (XO64) was moved from a position near the instrumented subassembly to an equivalent position across the core.

b. Nondestructive Testing Methods (C. L. Livengood)

New fixtures have been designed and built for handling experimental capsules and fuel elements for neutron radiography in TREAT. The new fixtures will simplify loading and unloading in the FCF air cell. More capsules or elements can be radiographed simultaneously with the new equipment. The capability to rotate the elements or capsules while in the TREAT radiography facility was incorporated in the design to eliminate the need to return them to the FCF air cell for manual rotation.

6. Materials-Coolant Compatibility (D. W. Cissel)

a. Evaluation and Surveillance of EBR-II Materials (W. E. Ruther and S. Greenberg)

Last Reported: ANL-7640, pp. 46-49 (Nov 1969).

(i) Capsule Bodies. Specimens of GE experimental-capsule bodies FOE and FOJ were received for electron-microprobe examination. Metallography has indicated occasional grain-boundary attack to a depth of several grains.

TABLE I.D.2. Status of EBR-II Experimental Irradiations as of December 15, 1969 (start of Run 39)

Subassembly No. and (Position)	Date Charged	Capsule Content and (Number of Capsules)	Exper- imenter	Accumulated Exposure (MWd)	Estimated Goal Exposure (MWd)	Burnup ^a
XG03 (701)	7/16/65	UO ₂ -20 wt % PuO ₂ (2)	GE	24,910	28,700	6.4
XG04 (781)	7/16/65	UO ₂ -20 wt % PuO ₂ (2)	GE	26,106	45,000	6.7
X0188 (4E2)	10/2/69	Structural (3) Structural (2) Structural (1) Structural (1)	GE ANL ANL PNL	600	10,000	0.2 + 5.8 ^b + 6.0 0.2 + 5.8 ^b + 6.0 0.2 0.2
X020 (685)	1/13/67	UO ₂ -PuO ₂ (9) (U _{0.8} Pu _{0.2})C (3) Structural (4) Structural (2) Graphite (1)	GE UNC PNL ANL PNL	16,069	20,400	6.5 7.1 4.5 4.5 4.5
X0218 (201)	2/23/69	Structural (6) Structural (1)	PNL PNL	16,240 7,276	23,200 9,000	3.0 + 4.1 ^b + 7.1 3.0
X027 (483)	11/21/67	UO ₂ -25 wt % PuO ₂ (18) Structural (1)	GE PNL	13,392	16,000	7.5 5.3
X034A (2F1)	9/30/69	Structural (4) Structural (3)	ORNL ORNL	600	3,800	0.3 + 4.8 ^b + 5.1 0.3
X035 (783)	4/13/68	Structural (7)	ORNL	13,184	44,800	3.0
X036 (7E1)	7/25/68	UO ₂ -25 wt % PuO ₂ (19)	GE	10,790	43,300	2.8
X038 (7C5)	5/7/68	Structural (7)	INC	12,766	17,700	2.7
X040A (582)	9/30/69	UO ₂ -20 wt % PuO ₂ (18) UO ₂ -25 wt % PuO ₂ (16)	ANL GE	600	4,800	0.3 + 3.5 ^b + 3.8 0.3 + 3.4 ^b + 3.7
X041 (7A3)	7/24/68	Structural (7)	PNL	11,226	16,700	2.4
X043 (4D2)	2/20/69	UO ₂ -25 wt % PuO ₂ (37)	GE	6,506	11,000	3.5
X050 (4C2)	2/23/69	UO ₂ -20 wt % PuO ₂ (4) UO ₂ -28 wt % PuO ₂ (4) UO ₂ -20 wt % PuO ₂ (5) (U _{0.82} Pu _{0.18})C (2) Structural (4)	GE GE ORNL W GE	6,506	7,500	3.6 + 7.7 ^b + 11.3 3.5 3.5 3.5 2.5 + 5.3 ^b + 7.8
X051 (3A2)	12/16/68	UO ₂ -25 wt % PuO ₂ (37)	PNL	7,051	16,400	1.4
X054 (4E1)	3/31/69	UO ₂ -25 wt % PuO ₂ (37)	PNL	5,906	10,000	3.1
X055 (6A4)	2/23/69	(U _{0.85} Pu _{0.15})C (19)	UNC	7,276	20,000	2.3
X056 (5C2)	4/2/69	UO ₂ -25 wt % PuO ₂ (37)	GE	5,906	10,600	2.9
X057 (2B1)	2/23/69	Structural (7)	PNL	7,276	15,000	3.0
X058 (6F1)	4/24/69	UO ₂ -25 wt % PuO ₂ (37)	GE	5,330	16,000	2.0
X059 (4A1)	4/23/69	UO ₂ -25 wt % PuO ₂ (37)	PNL	5,330	17,500	1.8
X061 (7A5)	4/23/69	Structural (7)	INC	6,100	18,000	1.3
X062C (6F3)	5/23/69	UO ₂ -25 wt % PuO ₂ (37)	GE	4,198	13,400	1.8
X063 (7F5)	6/29/69	Magnetic Materials (7)	ANL	3,766	5,400	0.8
X064 ^d (4F2)	5/28/69	UO ₂ -25 wt % PuO ₂ (19)	GE	4,198	10,700	2.3
X069 (4F1)	10/1/69	UO ₂ -25 wt % PuO ₂ (37)	PNL	600	20,700	0.2
X072 (6E2)	12/12/69	UO ₂ -20 wt % PuO ₂ (18) Structural (1)	ANL ANL	0 0	9,200	0 0
X073 (6C3)	12/12/69	UO ₂ -25 wt % PuO ₂ (37)	PNL	0	29,600	0
X012A (4B2)	12/12/69	UO ₂ -20 wt % PuO ₂ (19)	NUMEC	0	4,200	0 + 10.3 ^b + 10.3
X001 ^e (5F3)	11/19/69	UO ₂ (16) Structural (2)	ANL ANL	0 0	2,700	0 0

^aEstimated accumulated center burnup on peak rod based on unperturbed flux (fuels, at. %; nonfuels, nvt x 10⁻²²).^bor minus exposure from another subassembly.

Only preliminary results from FOJ are available. There appears to be a very slight increase in carbon in the corroded grain boundaries but a significant increase in chromium. The scan for oxygen has not been completed. One unusual feature of the specimen is the prevalence of tiny particles rich in manganese and sulfur.

(ii) Corrosion Specimens. Spool-type corrosion specimens removed from Subassembly XO15 exhibited unusually high weight losses. For example, two samples of Type 304 stainless steel lost 15.1 and 6.3 mg/cm² in this subassembly as compared with <1 mg/cm² for other test specimens. The temperatures of the sodium contacting the samples were calculated as 469 and 455°C, respectively, and the flow rate of the sodium was 4 m/sec. The samples were in the reactor for 29 months, with 160 EFPD (effective full power days) at 45 MWt and 82 EFPD at 50 MWt.

Metallography disclosed a few areas of slight surface roughening. These areas were examined with the electron microprobe, but no change in surface composition was detected. The reason for the higher-than-normal weight losses remains unknown.

Similar spool specimens of Inconel 600, Incoloy 800, and Hastelloy-X from the same subassembly also showed unusually high weight losses.

b. Examination of Materials from EBR-II Surveillance Subassemblies (S. Greenberg)

Last Reported: ANL-7640, pp. 49-50 (Nov 1969).

Table I.D.3 summarizes the results of tensile measurements of samples cut from the Type 304 stainless steel graphite-containing cans removed from SURV-2.

TABLE I.D.3. Tensile Properties^a
of SURV-2 Graphite-can Material

	Average	Range
Yield Strength, psi	42,500	40,900-44,100
Ultimate Strength, psi	90,200	87,900-92,400
Elongation, %	41	37-44
Reduction Area, %	50	45-56

^aObtained at strain rate of 0.012 min⁻¹.

Tensile properties of the original can material have not been determined. However, comparison of the values in Table I.D.3 with typical

values for Type 304 stainless steel shows that very small changes in tensile properties resulted from the SURV-2 exposure. The material is still very ductile.

c. Effect of Interstitial Elements in EBR-II Sodium

Last Reported: ANL-7640, p. 50 (Nov 1969).

(i) Nitridation of Type 304 Stainless Steel in Sodium
(T. D. Claar)

As a conclusion to the higher-temperature nitriding experiments, 18-mil Type 304 stainless steel foils were exposed to 550 and 650°C sodium under an A-1.0% N₂ cover gas for two weeks. The weight of the foils had increased slightly ($<0.01 \text{ mg/cm}^2$). Microscopic examination of the previously electropolished surfaces, which were subsequently exposed to the sodium, revealed nitride precipitates at the grain boundaries. There were no great differences in the appearance of the surfaces of the 550 and 650°C specimens. Metallographic examination of transverse sections of the two specimens revealed slight nitridation at the grain boundaries of the surface exposed to sodium. Bulk chemical analysis of the foils indicated that the nitrogen content had not increased detectably above the 0.028 wt % found in the original material.

A 5-mil foil of Type 304 stainless steel is being exposed to 371°C (700°F) sodium under the same A-1.0% N₂ cover gas. The foil will be exposed for at least a month in an effort to determine the nitriding potential under conditions similar to those found in the EBR-II primary tank.

7. Systems Engineering (B. C. Cerutti)

a. Surveillance, Evaluation and Studies of Systems

Last Reported: ANL-7640, p. 51 (Nov 1969).

(i) Argon Cooling System of Fuel-unloading Machine

(a) Modification of Vapor-trap Filter (H. W. Buschman)

The purpose of this modification was to provide a new type of filter to improve the performance of the vapor trap in the argon cooling system (ACS) of the fuel-unloading machine (FUM). Sodium which is not caught by this filter collects as an oxide in other filters, the ACS turbines, the FUM gripper, and other system components. The original filter element became plugged frequently, long before its capacity had been reached. Only the first few inches of the 36-in. filter length plugged, restricting flow and forcing replacement of the filter element.

A new filter element has been designed, procured, and installed in the existing FUM-ACS. The new element is made of sintered stainless steel tubes and has a flow area approximately 25 times greater than that of the original filter, which was made of stainless steel mesh. A baffle is placed ahead of the filter element to act as a separator for removing suspended droplets of sodium. A sodium-catch tank is located below the vapor trap and connected to it with a 1-in. drain line. Heaters on this drain line and on the baffle section of the filter maintain temperatures above the melting point of sodium. Sodium collected by the filter should therefore drain into the catch tank.

The newly installed vapor trap was operated for the first time in December. The initial (clean) pressure drop across the assembly was negligible, as expected. Long-term operating data are now necessary to evaluate the performance of the new type of filter element.

8. Reactor Analysis, Testing and Methods Development

Last Reported: ANL-7640, pp. 58-67 (Nov 1969).

a. Flux and Power Contours in a Typical EBR-II Core Loading (L. B. Miller, R. E. Jarka, and P. Fullerton)

Comprehensive computing methods now routinely operational in the EBR-II Project have been used to produce a detailed mapping of the topology of flux and power in a typical EBR-II core.

Figure I.D.5 is a contour map of the fast flux in Run 32B as determined by an S_4 DSN calculation performed with the IBM-360/75 and the DOT-5 code. The usual detailed core geometry was used in the calculation, with the composition of each subassembly specified. The usual mesh, with four points per subassembly, and the usual cross-section set 23806 were used in the calculation.

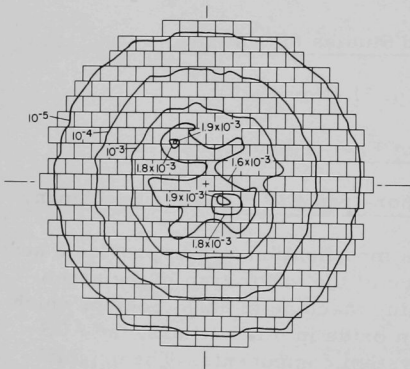


Fig. I.D.5. Contour Map of Fast Flux in
EBR-II Run 32B ($E > 2.23$ MeV)

Figure I.D.5 is oriented in the usual way, with sector B of the reactor at the top and the stainless steel drop rod at the right. Two peaks are evident in the fast flux. However, the peak at the upper left side of the core center is due to an experimental-irradiation subassembly containing unencapsulated, highly enriched fuel located at that point. The peak at the

lower right of the center of the core is more representative of the flux asymmetry in the reactor. This flux peak is about 7 cm from the center of the core. The fast flux includes all neutrons with energies greater than 2.23 MeV. The fission source is normalized to one neutron. Therefore, to obtain the flux at 50 MWt, the flux must be multiplied by 1.4×10^{17} .

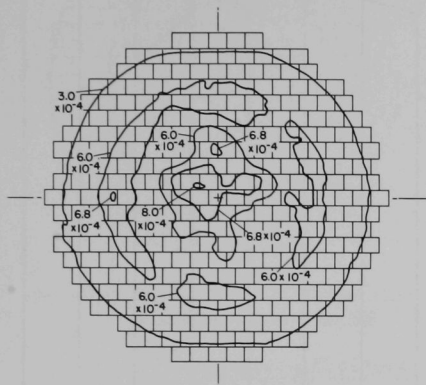


Fig. I.D.6. Contour Map of Low-energy Flux in EBR-II Run 32B ($E < 40.9$ keV)

power-distribution map, differing only because ν is a function of neutron energy of fission and is different for different fissile isotopes. The asymmetry evident in the figure is due to asymmetry of the flux and variations in the enrichment of the various experimental-irradiation subassemblies in the core. The peak above and to the left of the core center, in particular, is due to the latter effect. Except for this point, the peak power is near the center of the reactor, with the fuel element in position 2E1 producing slightly more power than the central driver subassembly.

Figure I.D.8 shows the power along the line through the center of the core from bottom to top, and Fig. I.D.9 shows the power along the line through the center of the core from left to right. Typically, corresponding subassemblies on opposite sides of the core center vary in power production by about 5%. Blanket subassemblies on opposite sides of the core vary in power between 5 and 10%.

The low-energy flux shown in Fig. I.D.6 includes all neutrons with energies below 40.9 keV. There are four regions in the core in which the low-energy flux exceeds 6×10^{-4} . With the normalization shown in the figure, there is one point about 7 cm from the center of the core where the flux exceeds 8×10^{-4} , and there are two points 15 and 35 cm from the center of the core, respectively, where the flux exceeds 6.8×10^{-4} .

Figure I.D.7 is a contour map of the neutron-emission rate. This map is very nearly the same as a

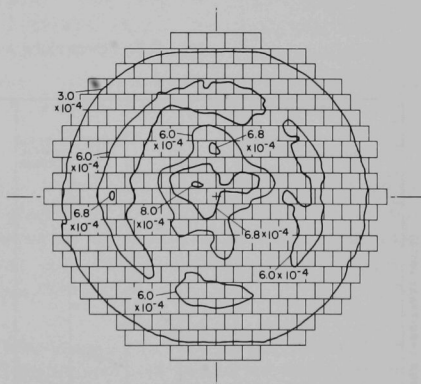


Fig. I.D.7. Contour Map of Rate of Fission-neutron Emission in EBR-II Run 32B

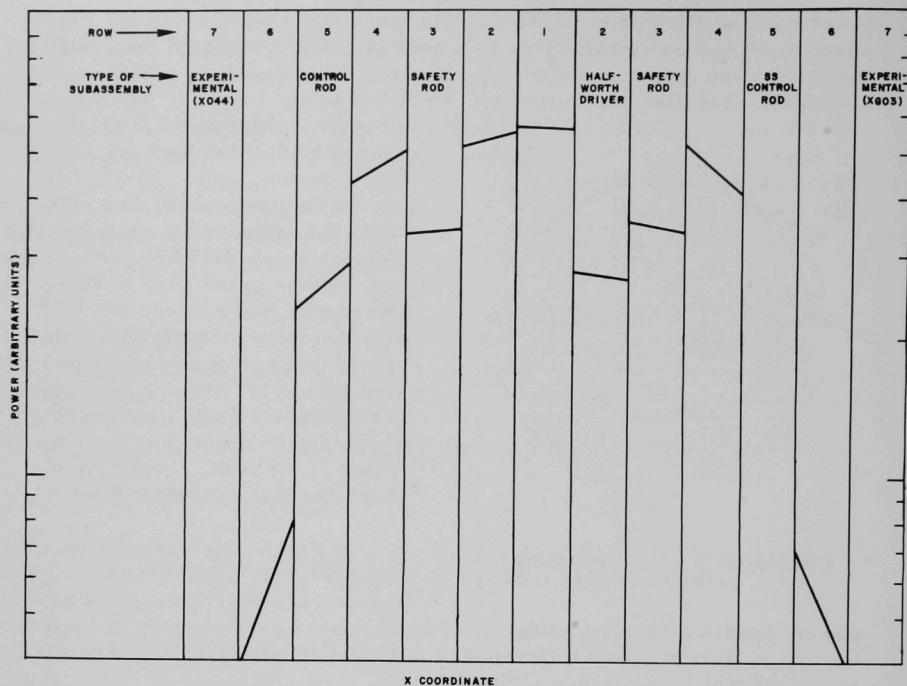


Fig. I.D.8. Power along X-coordinate 21 in EBR-II Run 32B

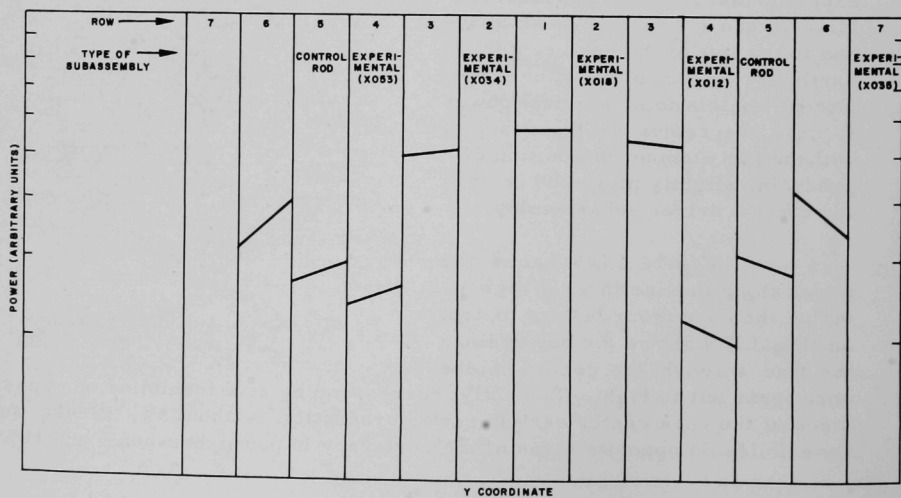


Fig. I.D.9. Power along Y-coordinate 21 in EBR-II Run 32B

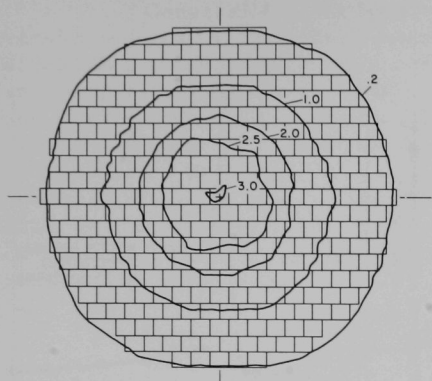


Fig. I.D.10. Contour Map of ^{235}U Microscopic Fission Rate in EBR-II Run 32B

Figure I.D.10 shows the ^{235}U microscopic-fission-rate contours. Since the microscopic fission rate is the integral of the energy-dependent flux and fission cross sections, much of the spatial fluctuation evident in the detailed group fluxes is eliminated in this integrated quantity. Some asymmetry, however, still is evident in this quantity.

The contour maps for each quantity show a tendency to be circular near the center and to assume the hexagonal shape of the core near the core-blanket interface between Rows 6 and 7.

b. Temperature Distribution in a Mechanically Mixed Oxide Fuel
(R. K. Lo)

A transient-heat-transfer computer code (THTB) was used to determine the temperature distribution in heterogeneous $\text{UO}_2\text{-PuO}_2$ fuel for the case of a power excursion following the hypothetical insertion of a central EBR-II driver-fuel subassembly into a just-critical core. The reactor was assumed to be tripped on a 7.5-sec period. The fuel rod considered was 0.25 in. in diameter, the cladding was 0.015 in. thick, the PuO_2 particles were $20\ \mu$ in size, and the UO_2 particles were $500\ \mu$. The contact conductance between PuO_2 and UO_2 particles was taken as $4000\ \text{Btu/hr-ft}^2\text{-}^\circ\text{F}$, and that between the UO_2 particles and the cladding as $1500\ \text{Btu/hr-ft}^2\text{-}^\circ\text{F}$. The linear heat generation was $16\ \text{kW/ft}$.

Assuming that the fuel was located in Row 1 and that, for conservatism, all uranium was ^{238}U , the relative power density in the plutonium was calculated to be 74.2%, and that in the uranium to be 25.8%. (The volumetric heat generation of PuO_2 particles was $4.695 \times 10^8\ \text{Btu/hr-ft}^3$, and that of UO_2 particles was $1.633 \times 10^8\ \text{Btu/hr-ft}^3$.)

By use of the power trace shown in Fig. I.D.11 (as computed with the AIROS II-A code) and physical data outlined above as input to the THTB code, the temperature distribution in the PuO_2 and UO_2 particles was obtained. The calculated volume-weighted average temperatures are shown in Fig. I.D.12. For this case, the volume-weighted temperature of PuO_2 is almost the same as that of the UO_2 .

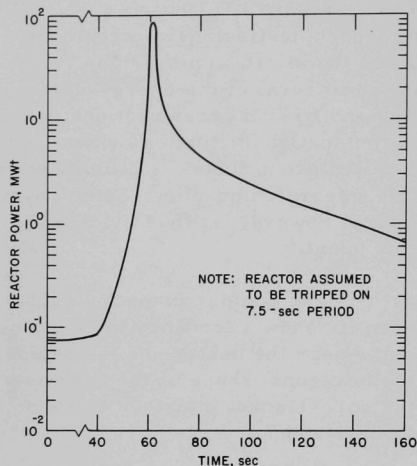


Fig. I.D.11. Power Excursion Following a Postulated Insertion of a Central Driver-fuel Sub-assembly into a Just-critical EBR-II Core

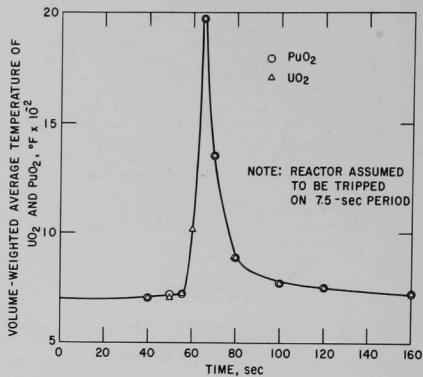


Fig. I.D.12. Calculated Transient Average Temperature for a Power Excursion Following a Postulated Insertion of a Central Driver-fuel Sub-assembly into a Just-critical EBR-II Core

c. Development of the MELT-II Code (R. Shum)

Compilation of the MELT-II code for the IBM-360/75 system has been completed, and further testing of the program is under way. The FORTRAN V language, such as the "reducing do loop," has been changed back into the FORTRAN-IV version. The name-list input used in adapting the original code to the UNIVAC 1108 caused problems with the 360/75 because of the ambiguity of the IBM system/360 FORTRAN-IV language manual. However, that name-list input now has been adapted successfully into the IBM 360/75 system. The input for MELT-II code in the IBM 360 system consists of four different card types:

- Card 1: 80 columns of Hollerith information, which will appear as the run title at the top of each page of output.
- Card 2: &NAM (starting in column 2).
- DATA CARDS: All data are input in the name-list format. Each card will be started in column 2, and commas will be placed between all entries.
- CARD N: &END (column 2).

Name-list input appears to be a very convenient way of reading in data. Changes in a standard data deck can be accomplished by simply naming, in any order.

Conversion to the IBM 360 system is more difficult than conversion to any CDC computer system. Even though the IBM 360/75 version of MELT-II is compiled, all subroutines encounter a lot of system errors such as OC4 and divide-check. These system errors can be detected only one at a time; therefore, cleanup effort has to be done in a step-by-step manner and from subroutine to subroutine. Two machine-language subroutines in the UNIVAC 1108 system that were used as drum storage for temperatures in the original MELT code still have to be modified for the IBM 360 disk-storage divide operation system. It appears that the MELT-II code will be productive in IBM 360/75 systems as soon as those two subroutines can be modified.

d. Current-collapsed Transport Cross Sections (D. Meneghetti and K. E. Phillips)

The collapse of fine-group transport cross sections at spatial mesh intervals to obtain sets of coarse-group, spatially dependent transport cross sections can in some cases result in negative values near the locale of interfaces.* This occurs because the fine-current solutions used as the weighting factors can be both inwardly and outwardly directed within a coarse-group energy interval. For example, this phenomenon can occur in the coarse-group energy interval from 40.7 to 67.0 keV for the case of an EBR-II type core surrounded radially by a nickel-rich reflector. In this case, negative values of coarse-group transport cross sections occur in the reflector within a distance of about 2 cm from the interface. This coarse-energy interval comprised 29 of the fine-energy intervals of the collapsing fine-group solutions.

To determine whether the negative coarse-group transport cross sections at the intervals of interest could be circumvented, this coarse group was subdivided into two and four smaller coarse intervals having approximately equal lethargies. For this example, it was found that division of the coarse-energy interval into four smaller coarse-energy intervals resulted in removal of the negative transport cross sections for the mesh intervals concerned. At one of these mesh points, for example, the four values are 2.03, 0.28, 0.49, and 0.52 cm^{-1} , respectively, when moving from high to low energy through the reference coarse-energy interval. For comparison, the negative value for the coarse-energy interval was -0.16 cm^{-1} .

e. Flow Calibration of Experimental Subassemblies Using Argon as the Modeling Fluid (A. Gopalakrishnan)

Water has been the only modeling fluid used so far in EBR-II for calibrating a single subassembly. The data from the water calibration can

* Meneghetti, D., and Phillips, K. E., Fine-spectral Interface Effects of Resonance Scattering upon Multigroup Cross-section Averaging, Trans. Am. Nucl. Soc. 11, 205 (1968).

be translated easily into equivalent sodium data valid under reactor operating conditions, and the availability of adequate coolant-flow rates for the subassembly thus can be verified prior to loading.

Some experimental subassemblies are disassembled for interim examination at regular intervals of irradiation. After inspection, they are reassembled and returned to the reactor. Under such circumstances, it is highly desirable that provision be made for flow testing the subassembly before each reloading to confirm that adequate sodium flow will be available to it during the ensuing irradiation period. Because of the residual radioactivity of the subassembly, such tests are made in shielded areas within the Fuel Cycle Facility where introduction of water loops is undesirable. Therefore, it has become necessary to investigate the applicability of an inert gas such as argon as the modeling fluid.

In applying the calibration data based on water to predict sodium flow rates, both water and sodium justifiably are assumed to be incompressible. Under this assumption, the frictional pressure drop in both systems can be shown to have similar power-law dependencies on the mass flow rate of the fluid. Preliminary calculations relating to flow modeling with gas had shown that variation of gas density from inlet to outlet could cause appreciable changes in this relationship, especially at low system pressures and high mass flow rates. Any residual heating that may be present in the subassembly tends to increase this effect.

A complete analysis of flow modeling with gas is possible only through the solution of the coupled conservation equations of continuity, momentum, and energy and of the equation of state. For one-dimensional flow of argon through a heat-generating subassembly, this set of equations has been solved with the IBM/360 Continuous System Modeling Program (CSMP). Results show that approximately 95% of the total pressure drop is due to friction and that most of the remaining 5% is due to acceleration of the gas stream. It is also found that in the range $2 \times 10^4 \leq Re \leq 6 \times 10^4$ for Reynolds numbers and for inlet gas pressures higher than 100 psia, the frictional pressure drop still has a single power-law dependence on the mass flow rate, very much similar to that obtained for the case of water. Thus, it seems possible that argon at $P_{in} \geq 100$ psia can be used as modeling fluid to predict the flow rates of sodium through experimental subassemblies.

Experiments are planned to obtain test data using argon and water and the same subassembly. The validity of the present analysis can be ascertained by noting how closely the analysis will predict the water data when the argon test data is used as input information.

f. Thermal-Hydraulics Code for*EBR-II (J. L. Gillette)

An additional orificing option has been added to the SNAFU code. This option allows a specified coolant mass flow rate for each subassembly

to be read into the code and the system temperatures to be determined accordingly. With this option it is now possible to analyze a greater number of conditions within the reactor, including that of partially blocked flow within a subassembly. With the three orificing options now in SNAFU (i.e., orificing to a uniform coolant-outlet temperature, orificing to a uniform maximum cladding temperature, and orificing to a specified flow distribution) along with the method of power allocation described in the Progress Report for November 1969 (ANL-7640, pp. 65-66), all the significant steady-state thermal-hydraulic conditions occurring in the reactor can be analyzed through the use of this code.

g. BOW-V Program (D. Mohr)

The problem of BOW-V nonconvergence at certain power levels apparently has been eliminated. Several test runs are being made for verification.

h. Two-dimensional Analysis of ZPR-3 Assembly 5 (B. R. Sehgal and J. E. Sullivan)

This work is an extension of that reported earlier in the Progress Report for September 1969 (ANL-7618, pp. 51-54), where results of calculations with three different cross-section sets for a one-dimensional spherical model of ZPR-3 Assembly 5 were compared.

The spherical model of an actual cylindrical assembly is based on the shape-factor correction derived from a correlation of shape factor versus the core L/D ratio and size. This correlation, based on some calculations* and some experiments with cores with depleted-uranium blankets,** is not a function of either the core composition or the blanket composition. ZPR-3 Assembly 5 has a lower-density blanket sandwiched between the core and the depleted-uranium blanket. A two-dimensional analysis for this assembly has been made.

The dimensions and compositions for this assembly were obtained from some early unpublished ZPR-3 memoranda. The composition and geometry used in calculations for the three-region cylindrical reactor are shown, respectively, in Table I.D.4 and Fig. I.D.13. The equivalent core radius was increased by ≈ 0.23 cm to account for heterogeneity, center-gap, and irregular-boundary corrections, respectively, of +4.1, -0.65, and -0.1 kg to the measured critical mass.

*Loewenstein, W. B., and Main, G. W., Fast Reactor Shape Factors and Shape-dependent Variables, ANL-6403 (Nov 1961).

**Davey, W. G., k Calculations for 22 ZPR-3 Fast Reactor Assemblies Using ANL Cross-section Set 635, ANL-6570 (May 1962).

TABLE I.D.4. Composition for ZPR-3 Assembly 5 (atoms/barn-cm)

Isotope	Region 1 (core)	Region 2 (light blanket)	Region 3 (depleted-U blanket)
^{235}U	0.006727	0.0000384	0.000089
^{238}U	0.007576	0.019056	0.040026
^{234}U	0.000069	None	None
Al	0.0190190	0.014658	0.001359
Fe	0.007712	0.004539	0.004539
Cr	0.001918	0.001129	0.001129
Ni	0.000839	0.000494	0.000494
Mn	0.000080	0.000047	0.000047

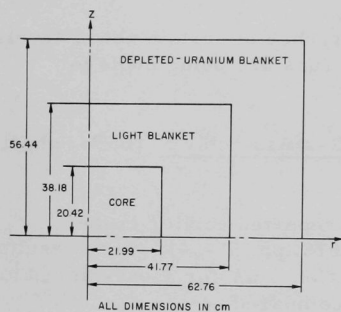


Fig. I.D.13. Geometry for R-Z Calculation of ZPR-3 Assembly 5

The 26 broad-group isotope cross sections for the three regions were derived from separate runs with the MC² code,* using the ENDF/B data and the actual compositions of the regions. The cross sections for the core region were calculated at the critical buckling, and those for the light blanket and the depleted-uranium blanket were calculated for $B_m^2 = 0.02 \text{ cm}^{-2}$.

The reactivity calculations were made in R-Z geometry with the DOT transport code** in the S₂ and S₄ approximations, and with the Argonne code DIF2D,[†] which does a diffusion-theory calculation.

Table I.D.5 gives the calculated values for k_{eff} . Diffusion theory gives a value of $k_{\text{eff}} \approx 2.95\%$ lower than that given by the transport S₄ calculation; the S₂ k_{eff} value is higher by $\approx 1.35\%$ than the S₄ value. The calculated value with the S₄ approximation is $\approx 1.27\%$ higher than the measurement. A similar difference was obtained for the calculated reactivity of ZPR-3 Assembly 6F, using the ENDF/B cross sections.

TABLE I.D.5. Calculated Values of k_{eff} for ZPR-3 Assembly 5

Type of Calculation	k_{eff}	% Δk with Respect to Value Calculated by Transport S ₄
Transport 2D R-Z S ₄ Approximation	1.01266	0.0
Transport 2D R-Z S ₂ Approximation	1.02617	+1.351
Diffusion 2D R-Z	0.98320	-2.946

*Toppel, B. J., Rago, A. L., and O'Shea, D. M., MC², A Code to Calculate Multigroup Cross Sections, ANL-7318 (1967).

**Mynatt, F. R., DOT, A Two Dimensional Discrete Ordinate Code, Report K-1694, Radiating Shielding Information Center, Oak Ridge National Laboratory. Also see ANL-7513, p. 50 (Oct 1968).

[†]Toppel, B. J., Argonne Reactor Computation System, ANL-7332 (1967).

Table I.D.6 shows the calculated and measured results for the ratio of ^{238}U fission and capture and of ^{234}U fission and ^{239}Pu fission to that of ^{235}U fission at the core center. The calculated results are in fair agreement with the measurements except for the ^{234}U fis/ ^{235}U fission ratio. This disagreement may be either due to errors in the ENDF/B ^{234}U fission cross sections or to discrepancies in the experiment.

TABLE I.D.6. Calculated and Measured Fission and Capture Ratios for ZPR-3 Assembly 5

Ratio to ^{235}U Fission	Calculated	Measured
^{238}U Fission	0.0714	0.0741 ± 0.0015
^{238}U Capture	0.1089	0.107 ± 0.004
^{234}U Fission ^a	0.4499	0.56 ± 0.01
^{239}Pu Fission	1.1952	1.243 ± 0.015

^aAnother measurement with an absolute counter gave a value of 0.40 for the ^{234}U fis/ ^{235}U fission ratio.

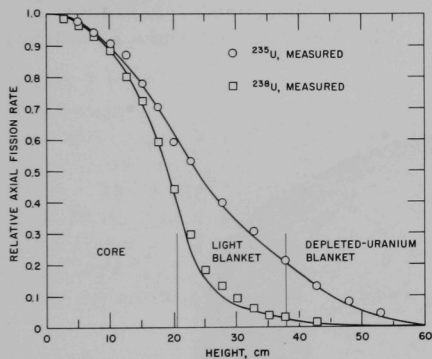


Fig. I.D.14. Relative ^{235}U and ^{238}U Axial Fission Rates for ZPR-3 Assembly 5

change is in the calculated ^{238}U fission distribution in the blanket regions; the results of the two-dimensional calculations show lower rather than higher values in comparison with the measurements. This behavior is consistent with the suspicion that the ^{238}U inelastic cross sections in the ENDF/B data file are high.**

Figure I.D.14 shows the ^{235}U and ^{238}U fission-activity distributions along the Z axis of the assembly calculated in the S_4 problem and compares them with the measured values as reported by Long *et al.** The general agreement is encouraging. However, the measurements for the ^{238}U fission are higher by 10 to 30% in the region of the light blanket.

A comparison of the two-dimensional calculations described here with the one-dimensional calculations reported earlier in ANL-7618 shows little change in the k_{eff} and the fission and capture ratios. The major

* Long, J. K., *et al.*, "Fast Neutron Power Reactor Studies with ZPR-III," *Proceedings of the Second Geneva Conference* 12, 119 (1958).

** Zolotar, B. A., Sehgal, B. R., and Kallfelz, J. M., *Fast Reactor Integral Studies of Modifications to ENDF/B ^{238}U Inelastic Scattering*, *Trans. Am. Nucl. Soc.* 12, 743 (1969).

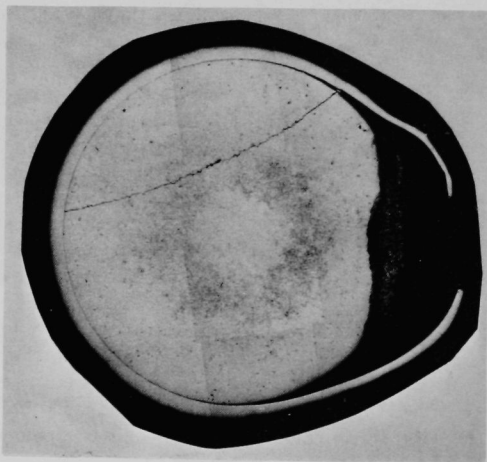
9. Driver Fuel Development (C. M. Walter)

a. High Burnup Encapsulated Irradiations (W. N. Beck)

Last Reported: ANL-7640, pp. 68-70 (Nov 1969).

(i) Postirradiation Annealing Tests of Encapsulated Mark-IA Elements BF02 and BF03. Elements BF02 and BF03 were irradiated to a calculated 3.7 at. % burnup at maximum cladding temperatures of 494°C. They are being subjected to postirradiation tests and destructive examinations. Element BF02 was postirradiation annealed at 500°C, and Element BF03 at 450°C. Both exhibited cladding failure during the anneals. The failures were longitudinal splits in the cladding, each $\sim 1/4$ in. long and located axially $\sim 1/4$ in. below the fuel restrainers. They tentatively are attributed to excessive plenum pressures due to a higher effective plenum temperature during the postirradiation test than that experienced during irradiation.

A transverse metallographic section through the failure in Element BF03, as seen in Fig. I.D.15, shows the cladding separated from the fuel. The thinning of the cladding indicates that the Type 304L stainless steel has retained a degree of ductility. The fuel does not show a tendency to expand in the direction of the break.



15X

Fig. I.D.15. Transverse Section of Element BF03
Showing Cladding Fracture Experienced
during Postirradiation Annealing Test

b. Fuel and Cladding Surveillance

Last Reported: ANL-7640, pp. 70-73 (Nov 1969).

- (i) Postirradiation Analysis of EBR-II Fuel (J. P. Bacca, A. K. Chakraborty, and G. C. McClellan)

AEC-RDT approved the ANL proposal to increase the maximum allowable burnup limit of low-swelling (high-silicon) EBR-II driver fuel from 1.5 to 1.8 at. %. This higher-burnup limitation became effective for the fuel at the start of reactor Run 39.

- (ii) Metallographic Examination of Irradiated Types 304 and 304L Stainless Steel (R. V. Strain)

Samples of Type 304 stainless steel capsule tubing from several experiments and of Type 304 stainless steel cladding from several driver-fuel subassemblies were examined metallographically to determine if the microstructure of the materials had been affected as a result of residence in the reactor or postirradiation sodium-removal operations.

Samples of capsule material which had been irradiated to about 3×10^{22} nvt (total fluence) in two incremental steps were examined. These capsules also had been subjected to two sodium-removal operations, one after each increment of irradiation. The samples of driver-fuel cladding were from controlled-flow, 70%-enriched, and extended-burnup subassemblies. The samples from the extended-burnup subassembly had been irradiated to the highest fluence to date for a driver-fuel subassembly (2.3×10^{22} nvt total fluence). The other samples were from driver-fuel elements which had been irradiated to ~1.5 at. % (1.8×10^{22} nvt total fluence) burnup under conditions simulating 62.5-MWt reactor operation.

None of the samples examined exhibited any evidence of grain-boundary attack or cracking. The samples, however, did exhibit the usual sensitization (precipitation of carbides at the grain boundaries). As expected, the sensitization was most severe in the regions of maximum temperature and fluence. The regions near the bottoms of the capsules and elements (the regions of low temperature and low fluence) exhibited little or no sensitization.

The double sodium removal from the sensitized capsule tubing caused no observable changes in microstructure which could be attributed to the reactor coolant sodium or to the sodium-removal operation. The microstructures of the driver-fuel cladding which had been irradiated at the higher temperature and fluence were very similar to those observed previously of normal driver elements. Again, there were no effects that could be attributed to the reactor coolant sodium or to the sodium-removal operation.

E. EBR-II--Fuel Fabrication

1. Cold Line Operations (D. L. Mitchell)

Last Reported: ANL-7640, pp. 78-80 (Nov 1969).*

a. Cold-line Production and Assembly

Cold-line production of Mark-IA fuel elements was concluded at the end of December, and production equipment was placed on a standby basis. However, the cold line will continue to fabricate nonirradiated sub-assemblies and will complete the impact bonding of the unbonded vendor elements. Future plans include the post-bonding reclamation heat treatment of vendor-fabricated elements. Table I.E.1 summarizes the production activities for November 16 through December 15, 1969, and for the year.

TABLE I.E.1. Production Summary for FCF Cold Line

	11/16/69 through 12/15/69		Total This Year	
	Mark IA	Mark II	Mark IA	Mark II
Alloy-preparation runs				
New fuel	0	0	11	8
Remelts	0	0	18	3
Total	0	0	29	11
Injection-casting runs	7	0	46	10
Pins processed				
Accepted	693	0	4,452	941
Rejected	43	0	162	53
Elements welded	266	0	4,599	884
Elements rewelded	0	0	0	69 ^a
Elements leaktested				
Accepted	264	0	4,470	804
Rejected	3	0	97	21
Elements bondtested				
Accepted	265	0	4,288	934
Rejected	11	0	423	9
Subassemblies fabricated (cold-line fuel)	0	0	37	6
Bonded elements received from vendor	0		24,313 ^b	
Inspected and accepted	0		23,621 ^{b,c}	
Inspected and rejected	0		1,251 ^b	
Unbonded elements received from vendor	2,649		11,853 ^d	
Impact bonded, inspected, and accepted by ANL	0		1,979	
Impact bonded, inspected, and rejected by ANL	0		190	
Subassemblies fabricated (vendor fuel)	1 ^e		17 ^f	
Total elements available for subassembly fabrication as of 12/15/69				
Cold-line fuel				
Mark IA	1,624			
Mark II	234			
Vendor fuel (Mark IA)	22,523 ^g			

^aIncludes 64 elements in which visual examination of welds indicated that they were not acceptable for potentially high-burnup experiments.

^bTotal includes figures for 1968.

^cIncludes fuel elements which were returned to vendor for rework to correct voids in sodium bond and after rework sent back to ANL for reinspection.

^dTen unbonded vendor elements were set aside for historical samples.

^eSubassembly contains mixture of ANL-impact-bonded vendor elements and cold-line elements.

^fIncludes subassemblies made up of a mixture of vendor and cold-line fuel elements.

^gThis figure does not include vendor elements that were impact bonded by ANL.

* This activity previously was reported under Operations--Fuel Cycle Facility.

One Mark-IA subassembly containing a mixture of ANL impact-bonded vendor fuel elements and of cold-line-produced fuel elements was fabricated in the cold line during the month.

An additional 2649 unbonded fuel elements were received this month from the Aerojet-General Corporation (AGC) for impact bonding; none of these were impact bonded during the month. All the unbonded elements (11,853) now have been received. Data relating to their receipt, impact bonding, and acceptance are summarized in Table I.E.1.

All as-fabricated fuel elements to be procured from AGC have been received and inspected by ANL. The current number (as of December 15, 1969) of AGC elements available after verification inspection is 22,523 (this figure does not include the ANL-impact-bonded vendor elements). A summary of the data relating to receipt and acceptance of the fuel produced by AGC is included in Table I.E.1.

F. EBR-II--Operations

1. Reactor Plant (G. E. Deegan)

Last Reported: ANL-7640, p. 78 (Nov 1969).

After the test-2 instrumented subassembly was inserted in the reactor [see Sect. I.D.3.a.(i)], its operation was functionally checked. The steam system was hydrostatically tested, and the primary tank was cooled to 350°F in preparation for filling the secondary system. Checks were made of the test-2 instrumentation at 350°F.

The secondary and steam systems were heated to 350°F, the secondary system was filled, and all systems then were heated to 580°F. The flow instrumentation of the secondary system was calibrated with all systems isothermal. A load test of the 100- and 400-kW diesel generators was conducted. After heating the primary-tank bulk sodium to 700°F, flow calibrations of the primary system and tests of the pump controller were completed. All protective interlocks were checked, and fuel handling for Run 39A was begun. During preparations for fuel handling, control rod No. 9 could not be released from its drive. The drive was partially disassembled, and the necessary adjustments of the jaw drive were made.

When fuel handling was finished, there was a test of timed rod drops and a further check of the instrumented-subassembly instrumentation. During the heatup, the indication from one of the outlet coolant thermocouples of the test-2 subassembly was lost.

The reactor was started up on December 15, but was shut down again for a reactivity adjustment. After the reactor had been restarted, the control

rods were calibrated. Rod-drop experiments then were performed at 500 kW, and reactor power was increased incrementally with extensive monitoring of the test-2 instrumented subassembly at each 5-MWt power level between 10 and 50 MWt. The test-2 instrumentation responded normally except that temperatures were lower than predicted.

A rapid shutdown of the reactor was required when the steam seal regulator for the main turbine apparently failed to function normally. The regulator problem was corrected, and the reactor was returned to 50 MWt.

Fuel handling during this period consisted of the installation of the test-2 instrumented subassembly and the loading changes for Run 39A. These changes involved experimental subassemblies, as reported under Section I.D.5.a, and also included the following:

Three spent driver subassemblies were replaced, and the three core dummies which had been installed in the grid at the beginning of the maintenance period were replaced with driver subassemblies. Five of these six driver subassemblies contained vendor fuel which had been impact bonded. One of the five was a controlled-flow subassembly. One Mark-II surveillance subassembly, the 70%-enriched surveillance subassembly, and the upper-leaky-weld-test subassembly were removed to the storage basket.

The reactor was operated for 170 MWd between startup for Run 39A through December 20, bringing its cumulative operational total to 30,210 MWd.

2. Fuel Cycle Facility (M. J. Feldman)

a. Fuel Handling and Transfer (P. Fineman)

Last Reported: ANL-7632, p. 93 (Oct 1969).

A summary of fuel-handling operations is included in Table I.F.1, and is for the period since operations in the air cell and argon cell were resumed following completion of the work program in the air cell [see Section I.F.2.c.(i), below].

TABLE I.F.1. Summary of FCF Fuel Handling

	12/9/69 through 12/15/69	Total This Year
<u>Subassembly Handling</u>		
Subassemblies received from reactor		
Driver fuel (all types)	1	120
Experimental	1	21
Other (blanket)	0	5
Subassemblies dismantled for surveillance, examination, or shipment to experimenter		
Driver fuel	0	113
Experimental	1	20
Other (blanket)	0	3
Driver-fuel elements to surveillance	0	5,472
Number from subassemblies	0	113
Subassemblies transferred to reactor		
Driver fuel	0	57
Experimental	0	9

TABLE I.F.1 (Contd.)

	12/9/69 through 12/15/69	Total This Year
<u>Fuel-alloy and Waste Shipments</u>		
Cans to burial ground	0	27
Skull oxide and glass scrap to ICPP	1	3
Recoverable fuel alloy to ICPP		
Fuel elements	1 (17.59 kg of alloy)	33 (557.29 kg of alloy)
Subassemblies	0	17 (88.75 kg of alloy)
Nonspecification material	0	5 (84.3 kg of alloy)

- b. Experimental Support (J. P. Bacca, N. R. Grant, V. G. Eschen, R. V. Strain, J. W. Rizzie, and C. L. Meyers)

Last Reported: ANL-7640, pp. 81-84 (Nov 1969).

The following experimental-irradiation subassemblies were fabricated during the month and were made up of new capsules or elements:

<u>Subassembly No.</u>	<u>Type of Irradiation Subassembly</u>	<u>Capsule or Element Content (and number)</u>
XO72	Mark A19	ANL mixed U-Pu oxides (18) and structural (1); all capsules
XO73	Mark H37	PNL Series 6 mixed U-Pu oxides (37); all elements
XO74	Mark H37	PNL Series 8 mixed U-Pu oxides (37); all elements

- c. Reactor Support

Last Reported: ANL-7640, pp. 84-85 (Nov 1969).

- (i) Air-cell Entry (N. R. Grant)

The entry to the air cell of the Fuel Cycle Facility to perform contact maintenance and repairs of remotely inaccessible equipment and to install new in-cell examination equipment and services was successfully completed during the month. Completion of all scheduled items as well as several contingency items was accomplished. All work, including direct cleanup, was completed in 30 working days, mostly on a two-shift basis. No personnel accidents or injuries were sustained, and no one received gamma-radiation dosages in excess of the maximum specified for a calendar-quarter period.

The main entry door to the air cell was closed on December 9, and work immediately returned to normal, remote-handling operations. Operations within the argon cell also were begun.

PUBLICATIONS

Economics of Desalting Water and Generating Electricity in Singapore

W. R. Bohl,* J. L. Gillette, and M. W. Carbon*

Nucl. Appl. Technol. 8(1), 45-51 (Jan 1970)

Detection System for Super-Heavy Cosmic Rays

R. Gold and K. Porges

Bull. Am. Phys. Soc. 14, 1210 (Dec 1969) Abstract

Modifications to Fissile Element Cross Sections and Their Influence on Calculated Fast Reactor Parameters

J. M. Kallfelz, B. A. Zolotar, and B. R. Sehgal

Report EACRP L-77, European American Committee on Reactor Physics, Paris, France (1969)

Resonance-scattering Spectral-effects of a Structural-subassembly Heterogeneity in EBR-II

D. Meneghetti and K. E. Phillips

Report EACRP A-117, European American Committee on Reactor Physics, Paris, France (1969)

MATDIAG, A Program for Computing Multilevel S-matrix Resonance Parameters

Peter A. Moldauer, Richard N. Hwang, and Burton S. Garbow

ANL-7590 (July 1969)

Effects of Sodium and Sodium Removal on the Microstructure of Type 304L Stainless Steel Tubing

R. V. Strain

ANL/EBR-006** (Aug 1969)

The following appeared as Abstracts in Trans. Am. Nucl. Soc. 12(2) (Nov 1969):

Anomalous Irradiation Performance of Centrifugally Bonded EBR-II Driver Fuel

J. P. Bacca, M. J. Feldman, G. C. McClellan, C. M. Walter, and S. T. Zegler

p. 555

Transient Analysis of EBR-II with a Predominantly Oxide Fuel Loading

A. V. Campise

p. 915

*The University of Wisconsin.

**One of a series of "blueback" topical reports prepared by the EBR-II Project.

β_{eff} Ratio Measurements

S. G. Carpenter and S. Ramchandran
p. 650

A Physical Random-Number Generator

C. E. Cohn
p. 725

Performance of EBR-II Driver Fuel at 62.5-MW(th) Conditions

R. A. Cushman, J. P. Bacca, F. D. McGinnis, and R. R. Smith
p. 556

Neutron Radiography Experience with an Isotopic Source in the EBR-II Fuel Cycle Facility

D. C. Cutforth
p. 467

Central Reactivity Worth Measurements and Calculations

K. D. Dance, R. A. Karam, J. E. Marshall, and R. B. Pond
p. 647

Uranium Doppler Measurements in Oxide Core Critical Assemblies

J. W. Daughtry and R. A. Lewis
p. 720

Validity of Fast-Critical Experiments as Integral Tests of ENDF/B

W. G. Davey and A. L. Hess
p. 717

An Absolute Measurement of $\nu(^{252}\text{Cf})$ and Its Relationship to the Neutron Yield for Fissionable Materials

A. DeVolpi and K. G. Porges
p. 759

Determination of Burnup in EBR-II

E. R. Ebersole and F. S. Kirn
p. 690

Gastight Shielding Window Design for the Hot Fuel Examination Facility

T. W. Eckels and D. P. Mingesz
p. 859

Integration of the Multimode Kinetics Equations by the Method of Undetermined Parameters

E. L. Fuller, D. A. Meneley, and D. L. Hetrick*
p. 710

Thermal-Hydraulic and Doppler Characteristics of Some Oxide Cores for EBR-II

G. H. Golden and B. R. Sehgal
p. 916

The Influence of Neutron Energy Group Structure on Fuel Cycle Analysis of Fast Breeder Reactors

L. J. Hoover and D. A. Meneley
p. 441

Critical Mass Sensitivity to the Treatment of Heterogeneity Effects in a Large UC Fast Core, Assembly 5 of ZPR-6

R. A. Karam and J. E. Marshall
p. 718

Performance of the EBR-II Steam Generators and Intermediate Heat Exchanger

J. F. Koenig
p. 773

Design of the Hot Fuel Examination Facility Argon System

E. W. Landow and P. R. Hirsch
p. 860

The Argonne Variable-Temperature Rodded-Zone Facility

R. A. Lewis, K. D. Dance, E. F. Groh, F. H. Martens, J. F. Meyer,
and T. W. Johnson
p. 696

Prompt Feedback Reactivity in EBR-II

J. K. Long and R. W. Hyndman
p. 690

Analysis of Recent Dosimetry Experiments in EBR-II

J. R. Madell, N. D. Dudey, R. R. Heinrich, and R. E. Jarka
p. 939

Reactivity Effects in Critical Facilities due to Fissile Isotope Decay

R. G. Matlock, R. E. Kaiser, and J. M. Gasidlo
p. 652

Comparison of Multiple Foil and Time-of-Flight Neutron Flux Spectra in a Bare ^{235}U Assembly

W. N. McElroy,* R. J. Armani, and E. Tochilin**
p. 757

Resonance-Scattering Effects in Nickel- and Steel-Reflected EBR-II Type Systems

D. Meneghetti and K. E. Phillips
p. 692

Spectral Effects in Liquid Metal Fast Breeder Reactor Transients

D. A. Meneley and K. O. Ott†
p. 706

*Battelle Northwest Laboratory.

**U.S. Naval Radiological Defense Laboratory.

†Purdue University.

Measured Fast-Neutron Spectra after Reflection of Fission Source
Neutrons from a Six-Inch-Thick Steel Slab

W. Meyer* and G. G. Simons

p. 960

Asymmetry and Local Distortions of the Flux due to Gross Hetero-
geneities in EBR-II

L. B. Miller and R. E. Jarka

p. 772

Bilinear Weighting of Cross Sections for Group Collapsing and Cell
Homogenization in Transport Calculations

R. B. Nicholson

p. 731

Neutron Energy Spectra for Fast Reactor Irradiation Effects

D. Okrent, J. M. Kallfelz, W. B. Loewenstein, A. D. Rossin,
A. B. Smith, and B. A. Zolotar

p. 701

Calculation of Heterogeneity Effects in ZPR-Type Reactors

A. P. Olson and J. M. Stevenson

p. 625

An Improved Definition of the Breeding Ratio for Fast Reactors

K. O. Ott

p. 719

Extended Equivalence between Homogeneous and Heterogeneous
Resonance Integrals in Slabs

J. P. Plummer and R. G. Palmer

p. 625

Comparison of Proton-Recoil Proportional Counter and Time-of-Flight
Neutron Spectrum Measurements in a ^{235}U -Fueled Fast Reactor

J. E. Powell

p. 712

Analysis of Graphite Density Reactivity Measurements in ZPR-3,
Assembly 53

S. Ramchandran and R. G. Palmer

p. 691

Nuclear Manpower for the Utilities

A. D. Rossin and K. L. Voigt**

p. 801

A Vertical Assembler-Dismantler for the Fuel Cycle Facility

W. L. Sales, D. L. Mitchell, J. R. White, and J. P. Simon†

p. 843

*Kansas State University.

**American Nuclear Society, Hinsdale, Illinois.

†National Accelerator Laboratory.

A Simple Analytic Representation of Fast Reactor Spectra

M. Segev
p. 640

Core Components Test Loop (CCTL) Operating Experience

F. Smith, R. H. Armstrong, R. A. Jaross, E. L. Kimont, and
L. H. Bohne
p. 609

Measuring Reaction Rates in Heterogeneous Fast-Reactor Cells

G. S. Stanford, C. E. Till, and W. R. Robinson
p. 715

Preliminary Design of the Hot Fuel Examination Facility (HFEF)

N. J. Swanson, K. R. Ferguson, J. F. Lindberg, D. P. Mingesz,
R. C. Watson, and J. R. White
p. 853

EBR-II Subassembly Coolant-Outlet Temperature Measurement

W. R. Wallin, F. D. McGinnis, J. F. Koenig, and V. G. Eschen
p. 806

Prediction of Wall and End Effects in Proton-Recoil Spectrometers

T. J. Yule and E. F. Bennett
p. 517

Fast Reactor Integral Studies of Modifications to ENDF/B ^{238}U Inelastic Scattering

B. A. Zolotar, B. R. Sehgal, and J. M. Kallfelz
p. 743

II. OTHER FAST REACTORS--OTHER FAST BREEDER REACTORS--FUEL DEVELOPMENT

A. Irradiation Effects, Mechanical Properties and Fabrication

1. Mechanical Properties of Cladding Materials (F. L. Yaggee)

Not previously reported.

The hardware necessary for performing creep experiments with austenitic stainless steel specimens during cyclotron irradiation is nearing completion. The design is a modification of similar equipment used to perform creep tests in flowing sodium. This equipment will be assembled and proof-tested by establishing creep curves for austenitic stainless steel at temperatures and stresses that will be used in the cyclotron experiments.

Fifty, 0.007-in.-thick, austenitic stainless steel (Type 304) specimens have been completed for use in the cyclotron creep experiments. The specimen material came from the same source as that used in the EBR-II control-rod thimble recently given a postirradiation examination.*

2. Void-formation Modeling (S. D. Harkness)

Last Reported: ANL-7595, pp. 97-100 (July 1969).

The model for void formation has been improved. A separate expression for the nucleation rate of interstitial dislocation loops has been included. In previous work the temperature dependence of loop nucleation was assumed to be the same as for void nucleation. The new derived expression permits calculation of the activation energy for loop formation in terms of the line energy of the new dislocation, the stacking-fault energy, and the energy related to the supersaturation of interstitials. For low stacking-fault energy, the activation energy E_L is expressed as

$$E_L = \frac{\mu^2 b^3}{36 RT(\rho/M \ell n \text{ Ni/NiO})}$$

This leads to a nucleation rate

$$I_L = K \exp\left[\frac{-E_L}{kT}\right] (J_{i,L} - J_{v,L}) R_L^*$$

*Carlander, R., Harkness, S. D., and Yaggee, F. L., Fast-neutron Effects on Type 304 Stainless Steel, J. Nucl. Appl. Technol. 7(1), 67-75 (July 1969).

where

I_L = loop nucleation rate, $\#/\text{cm}^3 \text{ sec}$;

k = constant;

$J_{i,L}, J_{v,L}$ = the interstitial vacancy flux to a critically sized loop.

The resulting predicted void volumes are presented as a function of temperature and fluence in Fig. II.A.1. The exact position of the temperature maximum is quite sensitive to the form of the term for loop nucleation rate. Because of the obvious crudeness involved in this calculation, the predicted temperature of maximum void volume is valid only to about $\pm 50^\circ\text{C}$.

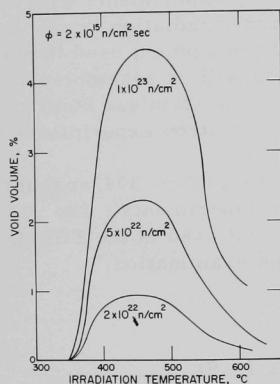


Fig. II.A.1.

The Predicted Effect of Fluence and Irradiation Temperature on the Void Volume in Type 304 Stainless Steel.

Recent work has also indicated the importance of separating the effects of neutron flux and length of exposure when experimental measurements of void number density and size are reported.

To date most experimental data on swelling in the U.S. have been gathered from the axial guide thimbles. Fluence dependence at constant temperature has been studied by using the sections of the thimble below and above the core, which are at roughly 371 and 460°C, respectively. In such a study, one is really investigating the effect of a flux profile at a constant time of exposure. For these conditions the model predicts (see Fig. II.A.2) that the void number density should increase roughly linearly with the flux, while the void size (see Fig. II.A.3) remains nearly constant for temperatures below 600°C. These predictions correlate well with results obtained at ORNL.*

For irradiation carried out at constant flux for varying lengths of time, it is predicted that the void number density saturates after rather short exposures (for irradiation temperatures in excess of 400°C), and that the average void size should show a steady increase with time. Thus, it is important to separate flux and time when experimental information on void size and number density is reported.

*Bloom, E. E., and Stiegler, J. O., Recent Observations of Irradiation Induced Void Formation in Austenitic Stainless Steel, Trans. Am. Nucl. Soc. 12(2), 589 (Dec 1969).

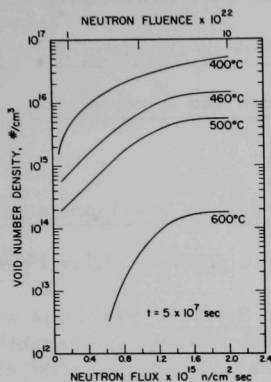


Fig. II.A.2

The Predicted Effect of Neutron Flux on the Void Number Density in Type 304 Stainless Steel for a Constant Time Exposure

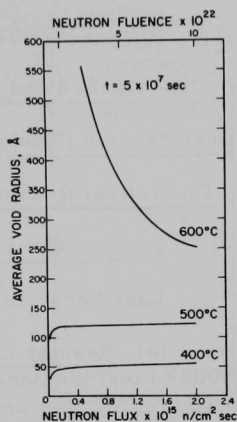


Fig. II.A.3

The Predicted Effect of Neutron Flux on the Void Size of Type 304 Stainless Steel for a Constant Time Exposure

PUBLICATION

Effect of Defects on the Rupture Ductility of Type-304 Stainless Steel Tubes under Biaxial Load

F. L. Yaggee and I.-C. Wang

Trans. Am. Nucl. Soc. 12(2), 570 (Nov 1969) Abstract

III. GENERAL REACTOR TECHNOLOGY

A. Applied and Reactor Physics Development

1. Theoretical Reactor Physics--Research and Development

a. Theoretical Reactor Physics

(i) Reactor Computations and Code Development (B. J. Toppel)

Last Reported: ANL-7640, pp. 88-91 (Nov 1969).

(a) Reactor Computation System. Problems were run with module STP006 to test the one-dimensional perturbation capability with respect to changes in isotopic cross sections and changes in the chi matrix of a composition.

One batch of problems was run with use of an isotopic cross-section set, ARC.JM31F, in which fissionable isotopes have different chi vectors. Isotopes subscripted with "B" have one chi vector while isotopes subscripted with "C" have a different chi vector, the set chi. The problems were run for a parallelepiped reactor described in Tables III.A.1 and III.A.2, and perturbations in isotopic cross sections and chi vectors were considered. Because composition 3 is composed of isotopes with different chi vectors it has a chi matrix. A criticality search resulted in a critical half-height of 92.03078 cm (the extrapolation distance was taken to be 16 cm). Thus the extrapolated critical reactor was nearly cubical.

TABLE III.A.1. Unperturbed Configuration

Region	χ_{outer} (cm)	Composition	Material ^a	Volume Fraction
1	10	1	B1	1.0
			B2	1.0
2	60	2	C1	1.0
			C2	1.0
3	80	3	B1	0.7
			B2	0.7
			C1	0.3
			C2	0.3
4	110	4	R1	1.0

^aSee Table III.A.2.

TABLE III.A.2. Isotope Makeup of Materials

Material	Isotope	Conc	Isotope	Conc	Isotope	Conc
B1	Fe	B 0.03	Ni	B 0.003	Cr	B 0.006
	Na	B 0.006				
B2	U-235	B 0.000025	U-238	B 0.01		
C1	Fe	C 0.03	Ni	C 0.003	Cr	C 0.006
	Na	C 0.008				
C2	U-235	C 0.00004	U-238	C 0.008	Pu-239	C 0.0013
R1	Fe	R 0.04	Ni	R 0.004	Cr	R 0.008
	Na	R 0.01				

The description of the problem and the comparison of the results of one-dimensional perturbation, two-dimensional perturbation, and one-dimensional diffusion calculations are given in Table III.A.3. The diffusion calculations were run with very tight convergence criteria so that k was computed with eight-figure accuracy. From Table III.A.3 it is seen that the agreement between the diffusion and perturbation calculations is excellent except for changes involving the transport cross section and the elastic-scattering transfer cross section. In agreement with earlier computations, there is slightly better agreement with diffusion calculation when leakage effects are calculated using $\delta D = D/D_1(D' - D)$ rather than $\delta D = D' - D$.

TABLE III.A.3. Comparison of One-dimensional Diffusion, One-dimensional Perturbation, and Two-dimensional Perturbation Calculations for Changes of Isotopic Cross Section and Chi Vector

Isotope		σ_x	Groups		Factor	$\Delta k/k^2, 10^{-4}$		
			From	To		1D Diff	1D Pert	2D Pert
U-235	B	σ_f	1	22	1.15	-1.295	-1.296	-1.296
U-235	B	σ_f	22	22	1.75	-1.790	-1.796	-1.796
U-238	B	σ_c	1	22	1.003	-1.496	-1.498	-1.497
U-238	B	σ_c	22	22	1.0075	-1.462	-1.465	-1.463
Pu-239	C	$\nu\sigma_f$	1	22	1.0002	1.739	1.739	1.739
Pu-239	C	$\nu\sigma_f$	5	5	1.1	1.304	1.304	1.304
Na	C	$\sigma_{tr}(\delta D_2)$	1	22	1.01	1.581	1.317	1.045
Na	C	$\sigma_{tr}(\delta D_1)$	1	22	1.01	1.581	1.315	1.044
Na	C	$\sigma_{tr}(\delta D_2)$	5	5	6	1.186	1.360	1.126
Na	C	$\sigma_{tr}(\delta D_1)$	5	5	6	1.186	0.974	0.809
Na	C	$\sigma_{i \rightarrow j}$	5-7	6-8	7	-1.258	-1.380	-1.380
Set Chi		χ	1	22	1.0004	3.943	3.943	3.942
Set Chi		χ	5	5	1.01	1.684	1.684	1.684
Set Chi		χ	5	7	1.004	2.824	2.824	2.824
U-235	B	χ	5	7	20	8.100	8.034	8.033
U-235	B	χ	1	22	1.1	2.029	2.028	2.028

Problems were also run to test the one-dimensional perturbation module with respect to perturbations of the neutron source induced by changes in isotopic chi matrices. For these problems the 26-group, Bonderenko, isotopic cross-section set, XS233.D1R, was used. The reactor was chosen to be a two-region sphere with compositions shown in Table III.A.4. The outer radii for criticality were obtained from a search within which the mesh was changed.

TABLE III.A.4. Description of Critical Spherical Reactor for Perturbations of Isotopic Chi Matrix

Region	Radius (cm)	Composition	Isotope	Concentration
1	22.594	1	U-235	0.006727
			U-238	0.007576
			Al	0.019019
			Ni	0.000839
			Cr	0.001918
			Fe	0.007712
2	55.094	2	U-235	0.000089
			U-238	0.040026
			Al	0.001359
			Ni	0.000049
			Cr	0.001129
			Fe	0.004539

The description of the problems and the comparison between the results of one-dimensional perturbation and one-dimensional diffusion calculations are given in Table III.A.5. The cross-section set has an energy structure such that neutrons are born in groups 1-11 and a neutron can induce fission of U-238 only when in groups 1-5. In the first four problems selected elements of the chi matrix for U-235 were multiplied by the factor f . In the fifth problem, elements of the chi matrix for U-238 for source neutrons appearing in groups 12-18 were made nonzero.

TABLE III.A.5. Comparison of the Results of Perturbation and Diffusion Computations for Changes of Isotopic Chi Matrix in a Two-region Spherical Reactor

Isotope	Matrix Perturbed for Groups		f	χ_{ij}	$\Delta k/k^2, 10^{-4}$	
	Absorption	Source			Diffusion	Perturbation
U-235	1-26	1-11	1.0005		1.707	1.708
U-235	1-26	3-6	1.0006		1.332	1.332
U-235	3-6	1-11	1.001		1.505	1.505
U-235	3-6	3-6	1.002		1.466	1.466
U-238	1-5	12-18		0.005	1.701	1.702
U-238	6-10	1-26		0.00025 ^a	1.531	1.532

^a $\nu\Sigma_f = 0.1$ was added in groups 6-10.

In the last problem, neutron-induced fission reactions for U-238 were added in groups 6-10 and the chi matrix was changed so that source neutrons appear in all groups. For all six problems the agreement between perturbation and diffusion calculations is excellent, as the discrepancies are less than 0.1%.

(b) MC^2 Capability in the ARC System. The effort to variably dimension the arrays in modules CSI001, CSC001, CSC002, and CSC003 by the incorporation of BPQINTER into their structure is almost complete. Only a small portion of module CSC003 still remains to be debugged. The reliability of these modules has been tested by problems involving both fine- and ultrafine-group calculations.

Consideration is being given to the computing time used by various areas within each of the modules representing the MC^2 capability in ARC. What is desired is to reduce the computing time without compromising the accuracy or flexibility of the current MC^2 capability. Improvement in the running time can be realized by improved program techniques in the existing code and by appropriate changes or relaxation in the rigor of the algorithms.

Examples of computing time comparisons for the various areas in MC^2 calculations in ARC are given in Table III.A.6. The timings were obtained from problems run on the current production version of the MC^2 capability in ARC. For these timing comparisons, the MC^2 calculation has been divided into four categories, each representing an ARC module, as indicated in Table III.A.6. The four modules have been broken down into calculational areas. The time in seconds is listed for each area in the module. The total time listed for each module includes the time for each area in the module plus any overhead, e.g., subroutine linkage time and printout time. The number in parentheses is the percentage of the problem run time spent in the module. The sum of the time spent in each of the four modules equals the total charge time for the calculation, e.g., CPU time plus wait time. At first glance the total run time for each problem seems large, but one must keep in mind that these problems have more materials and more Legendre treatment of materials than a "typical" problem. The times listed are for a calculation using three different options: as an all-fine-group P1 problem, as an ultrafine-group P1 problem, and as an ultrafine-group consistent P1 problem. All three problems contained eighteen materials, consisted of 27 broad energy groups, and had an energy range from 10 MeV to 22.6 eV. The fine-group problem consisted of 52 fine groups, the ultrafine problems of 1560 ultrafine groups. For the ultrafine-group calculations, oxygen, sodium, iron, nickel, chromium, and molybdenum were treated as Legendre materials.

Fifteen unresolved resonance-energy points were used for ^{149}Sm , fifteen for ^{238}U , sixteen for ^{239}Pu , fifteen for ^{181}Ta , fourteen for

^{240}Pu , and fifteen for ^{242}Pu . Of the total time in the unresolved resonance calculation, 13 sec (16%) was for ^{149}Sm , 8 sec (10%) for ^{238}U , 15 sec (19%) for ^{239}Pu , 13 sec (16%) for ^{181}Ta , 21 sec (26%) for ^{240}Pu , and 10 sec (13%) for ^{240}Pu .

TABLE III.A.6. Timing Considerations

Module	Area	P1 Fine-group Problem (Time, sec)	P1 Ultrafine-group Problem (Time, sec)	Consistent P1 Ultrafine-group Problem (Time, sec)
Input (CS1001)	Read Input, Adjust Broad-group Structure, and Make Consistency Check of All Input Data	2	2	2
	Total Time in Module CS1001	2 (<1%) ^a	2 (<1%)	2 (<1%)
Calculate Unresolved and Resolved Resonance Cross Sections (CSC001)	Reading Unresolved and Resolved Data and W Table from ENDF/B Library	10	10	10
	Unresolved Calculation	80	80	80
	Resolved Calculation	631	708	708
	Total Time in Module CSC001	721 (87%)	798 (47%)	798 (44%)
Calculate Nonresonant Cross Sections, Calculate Fundamental Mode Fluxes, and Iterate on Buckling to Critical (CSC002)	(Subroutine FIGERØ) Calculate Fine-group Effective Cross Sections for Nonresonant Quantities	44	49	49
	(Subroutine INSCAT) Calculate Inelastic and n,2n Cross Sections	12	12	12
	(Subroutine SOURCE) Calculate Fine- and Ultrafine-group Fission Spectrum	<1	3	3
	Input/OUTPUT Operations	3	15	15
	Buffer Legendre Data from ENDF/B Library	-	69	69
	Calculation in Subroutine ALRAGØ for First Iteration	-	519	586
	Calculation in Subroutine PØNE for First Iteration	-	2	2
	Time Spent in Subroutine ALRAGØ for Iterations 2-4	-	24	37
	Time Spent in Subroutine PØNE for Iterations 2-4	-	6	6
	Total Time in Module CSC002	60 (7%)	699 (41%)	779 (43%)
Calculate Broad-group Average Macroscopic and Microscopic Cross Sections, Calculate Broad-group Fundamental Mode Fluxes (CSC003)	(Subroutine AVER) Collapse the Ultrafine- and Fine-group Cross Sections	<1	11	19
	(Subroutine AVER1) Compute Individual Material Microscopic Cross Sections	42	188	201
	(Subroutine BGØNE) Generate Homogenized Macroscopic Broad-group Cross Sections	<1	1	1
	Total Time in Module CSC003	44 (5%)	200 (11%)	221 (12%)
	Total Running Time for Problems (sec)	827	1699	1800

^aThe number in parentheses is the percentage of the problem run time spent in the module.

The long computing time taken in the resolved resonance calculation is due to the large number of calls to subroutine QUICKW* during the Romberg integration.

The elastic-scattering, elastic-removal, and elastic-transport cross sections calculated in the first iteration in subroutine ALRAGØ* are stored on a disk pack. Note the large amount of running time for this area of calculation. During subsequent iterations all the time spent

*Toppel, B. J., et al., ANL-7318 (June 1967).

in subroutine ALRAGØ is only for reading these precalculated quantities from disk into the main core of the computer, and the time spent in this area is drastically reduced.

The next effort in the revision of the MC² capability in ARC will be to precalculate the elastic-scattering matrix from the Legendre coefficients. Since the MC² capability does not allow the lethargy width of the ultrafine groups to vary, the scattering matrices for all isotopes in the library (22 materials with Legendre data at present) will be calculated; these, rather than the Legendre coefficients, will be stored in the library thereby reducing the time discrepancy between the first and subsequent iterations in subroutine ALRAGØ for an ultrafine-group calculation. The new subroutine ALRAGØ will then read the elastic-scattering matrix for each Legendre material instead of the Legendre coefficients and homogenize these matrices for the problem at hand.

(c) ENDF/B Data Management in the ARC System. The five stand-alone codes involved with ENDF/B data management have been converted to ARC system modules, with the designations shown in Table III.A.7. The modules are invoked by the standard path STP010, and a catalogued procedure ARCSP010, which invokes the standard path, has been added to the Applied Mathematics library, SYS1.AMDPRØC. Use of the procedure alleviates the difficulties of job-control language which had been associated with use of the unlinked codes.

TABLE III.A.7. ENDF/B Data Management Modules

ARC Module	Code Name	BCD Input Data Sets	Purpose
CSI002	CHECKER	A.CHECK	Check ENDF/B tape
CSI003	CRECT	A.CRECT	Correct ENDF/B tape
CSI004	DAMMET	A.DAMMET	Delete, alter mode, and merge ENDF/B tapes
CSI005	ETØE	A.ETØE	Convert binary ENDF/B tape to MC ² format
CSI006	MERMC2	A.MERMC2	Merge two MC ² tapes and delete materials as specified
STP010	-	A.STP010	ARC system standard path

BCD input to the standard path includes the data sets shown in Table III.A.7. The set A.STP010 indicates which of the modules are to be invoked on a particular run. Complete flexibility is provided. The remaining data sets are simply the input cards for the unlinked codes. In order to retain the format specifications within the codes, the ~~NOSORT~~ option must be used for these data sets. For several of these input data sets, data were required specifying the data-set reference number of various binary data sets used by the particular code. These input numbers are disregarded by the ARC modules, and the requisite data are obtained using the ARC system conventions (SNIFF).

This effort, which required less than one man-week, demonstrates the ease with which code linking may be implemented using the conventions and environment of the ARC system.

(ii) Development of an Accident Code (G. J. Fischer)

Not previously reported.

(a) Change of Delayed-neutron Fractions during Core Meltdown. In order to get a base for the investigation of the dynamic behavior of the reactor during meltdown, the decrease in the delayed-neutron concentration due to loss of fission products by separation of the precursors through vaporization from the molten core has been investigated. The chemical and physical data for groups 1-4 are shown in Table III.A.8.* Data for groups 5 and 6 are not included because the short half-life leads to neutron emission before the possible escape of the precursors.

Without a mass transport of fuel vapor from the core region into the surrounding regions no considerable decrease in the population of delayed neutrons in the core region can be expected. Even in this case, the loss in delayed neutrons is limited to groups 1-3. It cannot be expected that the boiling rate and the bubble-growth rate is high enough to remove the precursors of groups 4-6 (which represent 50-60% of the delayed neutrons) before the decay by neutron emission. Therefore, the reduction in the delayed-neutron fraction does not exceed 50%. It should be noted that information of this type should be used with considerable care when application is to be made to a nuclear burst. These data give the initial delayed-neutron precursor population only.

*Proc. IAEA Symposium on the Fission Process, Vienna, Aug 1969.

TABLE III.A.8. Distributions of Delayed-neutron Precursors for U-235 and Pu-239

Group No.	Precursor Isotope	Half-life of Precursor, Including Parents (sec)	Parents of Precursors (lifetime in sec given in brackets)	Yield per 10^4 Fissions		Yield in Percent of Total Group Yield		State of Oxidation and Possible Chemical Composition at $P > 2500^\circ\text{K}$	Boiling Point ($^\circ\text{K}$)
				^{235}U	^{239}Pu	^{235}U	^{239}Pu		
1	Br-87	55	As (1.4), Se (5.8)	5.7	1.97	98.3	98.5	Br	330
	Sn-133	55	-	0.1	0.03	1.7	1.5	Sn SnO ₂ , decomposes at low oxygen pressure	2633
2	Br-88	16	Se (2.2)	11.1	3.41	35	18.8	See Br-87	
	I-137	24	Te (1.0)	19.7	14.42	62	79	I	457
	Cs-141	25	I (0.3), Xe (1.7)	0.3	0.23	1	1.3	Cs CsI, CsBr	943 1200
	Sb-134	11		0.2	0.07	0.5	0.4	Sb	1713
	Sn-134	2		0.5	0.09	1.5	0.5	See Sn-133	
3	Se-87	6	As (1.4)	0.4	0.10	1.3	1.0	Se	961
	Br-89	4.5	Se (?)	16.9	3.52	54.0	35.0	See Br-87	
	Rb-92	4.5	Br (0.8), Kr (1.9)	0.06	0.03	1.9	0.3	Rb	1266
	Rb-93	6	Br (?), Kr (1.2)	7.2	2.90	23.0	28.7	Affinity to O, I and Br, decomposition at elevated temperatures	
								See I-137	
	I-138	6	Te (?)	6.7	3.36	21.4	33.3		
4	Ge-84	?	-	0.8		1.0		GeO ₂	3100
	As-84-86	?, 2, ?	Ge, Ge (2); -	14.0		18.5		As	1000
	Se-88	2	-	4.16		5.5		Se	1012
	Br-90-92	1.6, ?	Se, -	22.4		29.7		See Br-87	
	Kr-92-93	1.9, 1.3	Br (0.8); Se; Br	1.82		2.4		Kr	120
	Rb-94	2.7	Kr (0.2)	14.2		18.9		See Rb-92	
	Y-98	2.0	Rb (3); Sr (?)	2.3	Not well known	3.0		Y	3200
	Sb-135	1.7	-	3.9		5.2		See Sb-134	
	Te-137	?	-	0.6		0.8		Te	1663
	I-139-140	1.7, 1.2	-	0.2		0.3		Xe	160
	Cs-142-145	2, 1.7, 1.0, ?	Xe (<1)	10.65		14.1		See Cs-141	

2. Nuclear Data--Research and Development

a. Cross Section Measurements (N. D. Dudgey and C. E. Crouthamel)

(i) Yields of Low-mass Fission Products

Last Reported: ANL-7618, p. 90 (Sept 1969).

An experiment is being planned (see ANL-7618) to measure fast-neutron fission yields of tritium by a radiochemical technique. Gram quantities of fissile material will be irradiated with monoenergetic fast neutrons produced in the Dynamitron. The irradiated samples will be hydrided and dehydrided in a radiochemical separation system in which the hydrogen isotopes (including tritium) will be separated from the other fission products. The tritium in the separated gas will be counted in a low-level gas proportional counter. The number of fissions will be determined by radiochemical analysis of the fissile material for several fission-product monitors. The neutron flux will be measured by means of a fission counter.

The gas-handling system in which the tritium separation will be carried out has been designed, and construction has started. Samples of ^{239}Pu , ^{240}Pu , ^{242}Pu , ^{233}U , and ^{235}U having high isotopic purity and low lithium content* have been obtained, and fabrication of the targets has begun. It is expected that fast-neutron irradiations will begin as soon as the Dynamitron is available for our use (March-April 1970). Yields of tritium in the thermal-neutron-induced fission of ^{235}U , ^{233}U , and ^{239}Pu will be measured first to check out the method and calibrate the equipment.

Original plans for determining the fission yields of tritium and other low-mass fission products involved the use of a particle-identification system to measure the mass, charge, energy, and angular distribution of emitted low-mass particles. Work on this method has been reduced because of budget limitations. Measurements of low-mass fission yields from the spontaneous fission of ^{252}Cf are being used to set the timing of the particle-identification system and to verify its performance. This system, with the exception of a suitable scattering chamber, is expected to be ready for fast-neutron measurements by the time the Dynamitron is available for use.

b. Burnup Analysis and Fission Yields for Fast Reactors
(R. P. Larsen)

(i) Development of Analytical Procedures for Fission-Product-Burnup Monitors

Last Reported: ANL-7618, pp. 90-92 (Sept 1969).

An X-ray spectrometric method is being developed for the determination of the four principal rare earth fission products: lanthanum, cerium, praseodymium, and neodymium. The initial application of the method to the analysis of a sample of irradiated fuel (13% enriched UO_2 irradiated in MTR) was reported in ANL-7618. The results obtained were in close agreement with those calculated, on the basis of individual rare earth fission yields, from the results of a previous analysis of the sample for total rare earths (TRE) by EDTA titration (see Progress Report for January 1968, ANL-7419, p. 96). The total concentrations of the four principal rare earths determined by X-ray and TRE analyses were 0.6062 and 0.6005 $\mu\text{mol/ml}$, respectively; the neodymium concentrations were 0.2706 and 0.2722 $\mu\text{mol/ml}$, respectively.

This sample was also analyzed for uranium, total neodymium, and ^{148}Nd by B. F. Rider of the General Electric Vallecitos Atomic Power Laboratory. The analyses were performed by a mass-spectrometric isotope-dilution (MSID) method. Rider's value for the total neodymium content, namely, 0.2723 $\mu\text{mol/ml}$, is in good agreement with our neodymium value of 0.2706 $\mu\text{mol/ml}$.

*A low lithium content is necessary because tritium is produced by reactio

Burnup values for the UO_2 fuel were calculated from the data of each method and the best fission yield data available. These values are given in Table III.A.9 together with the fission yields used; good agreement among the several methods is evident.

TABLE III.A.9. Comparison of Burnup Analyses of Irradiated UO_2 by Several Methods

Rare Earths Determined	Fission Yield (%)	Method	Burnup (at. %)
TRE ^a	49.35	EDTA	6.75
La, Ce, Pr, Nd	45.20	X-Ray	6.68
Total Nd	20.52	X-Ray	6.61 ^b
Total Nd	20.52	MSID ^c	6.65 ^b
¹⁴⁸ Nd	1.70	MSID ^c	6.62

^aTRE = total rare earths.

^bThese values were corrected for the ¹⁴⁴Ce (285 days) that had not decayed to ¹⁴⁴Nd (stable).

^cMSID = mass-spectrometric isotope-dilution analysis.

(ii) Development of a New Method for the Determination of the Absolute Fast Fission Yields of Burnup Monitors for Fast Reactor Fuels

Last Reported: ANL-7618, pp. 92-93 (Sept 1969)

(a) Determination of Alpha for ²³⁹Pu, ²³³U, and ²³⁵U. An experiment is being conducted by the ANL Reactor Physics Division to measure the effective capture-to-fission ratio (alpha) for ²³⁹Pu, ²³³U, and ²³⁵U in a neutron spectrum that emphasizes the 10-keV region, where the greatest uncertainties in alpha exist. The samples were irradiated in ZPR-3 in September 1969. The number of captures is being determined mass spectrometrically; * the number of fissions is being determined by gamma spectrometry from the activity of the fission product ¹⁴⁰Ba (see Progress Report for March 1969, ANL-7561, pp. 65-67). The factor which relates the ¹⁴⁰Ba activity to the number of fissions was established in a short (83-min) calibration irradiation which preceded the long (5-day) irradiation for the determination of alpha. in the short irradiation were nanogram amounts

*This work is being performed in the Chemistry Division.

of the fissile nuclides in contact with mica fission track detectors and milligram amounts of the fissile nuclides (as metal foils) which were used for the ^{140}Ba assays. Subsequent to the irradiation, the ^{140}Ba activity-to-fission factors were calculated from the ^{140}Ba counts, the number of fission tracks, and the weight of the fissile nuclides.

The fission-track counting* of the ^{239}Pu samples and the ^{140}Ba counting of the ^{239}Pu and ^{235}U foils (from both the short calibration irradiation and the long irradiation for the determination of alpha) have been completed. The number of fissions per 10^9 atoms of ^{239}Pu in the long irradiation was 230 ± 5 . The principal sources of error in this measurement were the determinations of the ^{140}Ba activity in the two irradiations. Each was measured with a precision of $\pm 1\%$. It is expected that the number of fissions which occurred in the ^{233}U and ^{235}U samples will be measured with accuracies comparable to that obtained for the ^{239}Pu .

(b) Determination of Fast Fission Yields. The ^{239}Pu and ^{235}U foils from the long (5-day) irradiation are being analyzed by gamma spectrometry to determine the relative fission yields of several short-lived nuclides and the absolute fission yield of ^{137}Cs . The values obtained will be compared with the values reported by Lisman *et al.*** for the EBR-I spectrum. The relatively low integrated neutron flux in the long irradiation (the burnup was only 2.30×10^{-5} at. %) precludes determinations of the fission yields of the stable fission product burnup monitors, e.g., the rare earths.

The technique described in the preceding section will be used to determine absolute fission yields in EBR-II (see Progress Report for March 1969, ANL-7561, p. 57). Two irradiations will be carried out: one of about 2-hr duration at a reactor power level of 50 kW and the other of sufficient duration (~120 days) at full power to produce samples having burnups of 1-2%. Because the length of the latter irradiation is considerably longer than that of the alpha experiment (~120 days versus ~5 days), a longer-lived fission product, e.g., ^{144}Ce (285 days), will be used instead of ^{140}Ba (13 days) to establish the activity-to-fission calibration factor.

c. Reactor Code Center (M. Butler)

Last Reported: ANL-7640, pp. 93-94 (Nov 1969).

A total of 907 program packages were distributed in fiscal 1969. Of these, 752 were requested by U.S. organizations; the remaining 155 were sent outside the United States. No records are available on distributions of our library collection made by the ENEA Computer Programme Library to member countries under international agreement.

* This work is being performed in the Reactor Physics Division.

** Lisman, F. L., *et al.*, Burnup Determination of Nuclear Fuels, IN-1277, p. 64 (1969).

It is interesting to look at the breakdown of the U.S. distribution indicating services rendered to AEC contractors and U.S. government operations, universities, public utilities, computer manufacturers, software and consulting agencies.

Distribution of Program Package Transmittals, FY 1969

AEC Contractors and U.S. Government Operations	442
Universities	147
Public Utilities	66
Computer Manufacturers, Software and Consulting Firms	97
Total	752

Largest users of library programs among AEC contractors were Argonne National Laboratory, Babcock and Wilcox, Combustion Engineering, and the Commission itself. The University of Cincinnati, Columbia University, Kansas State University, and the University of Missouri each received more than ten program packages. The Sacramento Municipal Utility District, Sacramento, Calif., led the public utility users, followed by Public Service Electric and Gas Company of Newark, N. J.; while the IBM Scientific Center at Palo Alto, Calif., and Keane, Pomerantz, and Associates of Pittsburgh, Penna., headed the fourth requester category with 20 and 10 packages, respectively.

Of the 155 transmittals outside the United States, 62 went to the ENEA Computer Programme Library and 29 others were mailed to universities. Canada, China (Taiwan), Israel, and Japan each received more than 10 packages.

B. Reactor Fuels and Materials Development

1. Fuels and Claddings--Research and Development

a. Behavior of Reactor Materials

(i) Fuel Behavior

- (a) Studies of Fuel-element Modeling (R. W. Weeks and V. Z. Jankus)

Last Reported: ANL-7632, pp. 103-107 (Oct 1969).

The convergence problems initially encountered with the LIFE fuel-element modeling code have largely been solved and tests of the code are in progress. As might be expected, large changes in stress, strain, zone-boundary migration, or operating conditions make the strongest demands on the code-convergence capability.

To test the code at a high strain rate, a very large solid fission-product swelling and a very high clad-creep rate were input in one of the earliest code tests. Two runs were made with identical input data; the first held power constant, except for the initial rise and final reduction, and the second followed additional power cycles during the same time period. The results are shown in Fig. III.B.1.

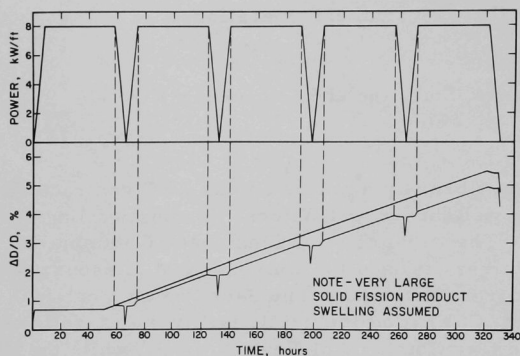


Fig. III.B.1

Results of a Preliminary Study
of LIFE Code Stability

The top curve in the cladding $\Delta D/D$ plot was the constant-power case, and the lower curve followed the power cycle. The coolant temperature history for these runs was taken proportional to the power level when the power was below 1 kW/ft, but above 1 kW/ft the coolant temperature was held constant.

The initial $\Delta D/D$ observed on the first rise to power is due only to thermal expansion of the clad. An incubation period follows until the fuel closes the fuel-clad gap, and then the assumed high solid fission-product swelling forces the clad to creep at an exaggerated rate. When the power level is lowered, the fuel contracts because of the lower temperature, and, in each case shown in Fig. III.B.1, the fuel-clad gap reopened. An initial elastic recovery of the clad (due to the reduced fuel-clad pressure) is computed, and, when the power level drops below 1 kW/ft, the clad contracts because of the lower coolant temperature. When the power increases again, the process is reversed, with the fuel contacting the clad only after reaching its full-power temperature.

The code is currently in a prove-out stage, which will include further checks on the code stability, gathering the "best available" set of materials input data, including data on fission-product and zone-boundary migration, and calibration of the code against a few "well-characterized" integral fuel-element tests to estimate materials data that are presently unavailable. The incorporation of a simplified model of fuel cracking is also being considered, along with incorporation of the U-Pu migration model (see Progress Report for April-May 1969, ANL-7577, pp. 140-142) and an updating of the clad-swelling model.

b. Oxide Fuel Studies

(i) Fuel Swelling Studies (L. C. Michels and G. M. Dragel)

Last Reported: ANL-7640, pp. 106-108 (Nov 1969).

During the preparation of replicas of irradiated oxide fuels, it was found that the insolubility of the plastic replicating tapes was caused in some cases by their exposure to irradiation rather than by too long an immersion in the acid cleaning bath. The acid bath was found to be unnecessary for cleaning the plastic replicas. Immersion of the tapes in a solution of detergent and water in an ultrasonic cleaner for a period of about 4 hr appears to be a very effective cleaning method.

A metallographic section from fuel element SOV-7 has been examined using replica electron microscopy. The specimen examined was a transverse section taken at a position 2.9 in. from the bottom of the fuel column. The fuel in this element consisted of vibratorily compacted Dynapak particles of (U,Pu)O₂. The burnup achieved was 3.6 at. %. The fuel element operated in a partially molten condition with a fuel surface temperature of approximately 1200°C.

What appear to be subgrain boundaries in the fuel were observed, starting at a position about 0.002 in. from the cladding. The subgrain size at this position was approximately 5 μ and increased toward the center of the fuel. The matrix also appeared to become "cleaner," or freer of debris, toward the center of the fuel, indicating that a sweeping process may be associated with the subgrain growth. The possibility is recognized that the observed boundaries (which are thought to be subgrain boundaries) are really high-angle grain boundaries that were initially present in the fuel particles. A study of some of the unirradiated fuel material is being conducted to determine the preirradiation grain size. This study will utilize both optical and replica electron microscopy.

(ii) Fuel-element Performance (L. A. Neimark and W. F. Murphy)

Last Reported: ANL-7640, pp. 108-110 (Nov 1969).

The Group O-3 encapsulated mixed-oxide fuel elements have been inspected and approved for irradiation in EBR-II. The 18 fuel-element capsules and the one structural materials capsule have been loaded in Subassembly XO72. The subassembly has been flow tested and accepted for irradiation and will be loaded into EBR-II in position 6E2 for Run 39.

2. Techniques of Fabrication and Testing--Research and Development

a. Nondestructive Testing Research and Development

(i) Investigation of Data-handling System (C. J. Renken)

Last Reported: ANL-7527, pp. 106-110 (Dec 1968).

With the development of a six-aperture electromagnetic transducer for the inspection of jacket tubing (see Progress Report for September 1969, ANL-7618, pp. 99-101), it has become necessary to investigate signal-processing methods to process effectively the increased information available from this type of transducer. With six apertures and two sampling points per aperture, a twelve-dimensional signal must be processed.

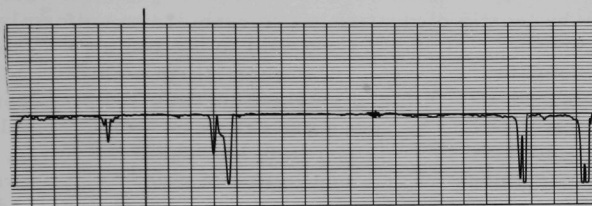
Preprocessing of the signals is accomplished in the following manner: The amplified signal from each pickup coil (each aperture has a pickup) is sampled at two points. One sampling point is chosen for maximum sensitivity to inner-surface defect signals and minimum sensitivity to lift-off. At least one of these so-called lift-off crossing points is always available. The other sample point is chosen for minimum sensitivity to inner-surface defects and maximum sensitivity to lift-off. This sampling point is always located at an early time during the duration of the signal from the pickup. The demodulated signals from each of these sample points are then linearly combined in the proper proportion to achieve minimum sensitivity to lift-off. This procedure is repeated for each of the channels associated with the six apertures. Each of these combined signals is then linearly combined with the signal from the aperture directly across from it or with the signal from the adjacent aperture, depending upon the type of extraneous noise most prevalent in the tubing under inspection. For instance, the signal-to-noise ratio in tubing that contains light, spiral markings from a final straightening operation can usually be dramatically improved by using the opposite-aperture technique. In any case, the three signals remaining after the second combination process are then each filtered by a transducer-broadbanding filter, filtered again through one or more slot filters to remove any other strongly periodic extraneous noise signals, and then fed to a circuit that adds the absolute values of the signals from each of the three pairs of apertures. Figure III.B.2 shows the filtered signals before and after being summed.

One of the defects shown in these recordings is an electromachined notch, 6.36 mm in length, in the outer surface of the tube. With an ideal broadbanding filter, that is, one whose transfer function was just the inverse of the spectral response function of the transducer, this notch would have appeared on the recording as a rectangle. Since the ideal broadbanding

filter is not physically realizable, the consequence of the departure of the broadbanding filters now in use from the ideal is shown in the distortion of the defect signal from the long notch. We have continued to investigate methods for synthesizing broadbanding filters that are better engineering compromises between signal-to-noise ratio, on the one hand, and a more faithful reproduction of transient signals, on the other.

Chart speed: 100 mm/sec
Scan speed: 91 mm/sec

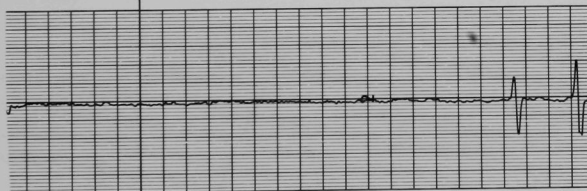
Tubing diameter: 0.230 in. (5.57 mm)
Tubing wall thickness: 0.015 in. (0.381 mm)



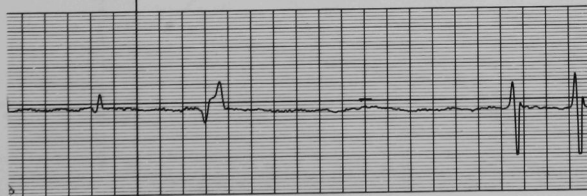
Sum of the absolute value of the signal from all apertures.



Apertures 1 and 4



Apertures 2 and 5



Apertures 3 and 6

Hole through the tube wall, 0.002 in. diameter (0.058 mm)

0.0015-in.-deep by 1/4-in.-OD notch (0.038 mm by 6.36 mm)

0.01-in.-diameter holes (0.25 mm)

FIG. III.B.2. Recordings of Signals from Defects in Type 316 Stainless Steel Tubing

b. NDT Measurement of Effective Cold Work in Cladding Tubes
(C. J. Renken)

Not previously reported.

Preliminary experiments to check the feasibility of using measurements of magnetic retentivity as a method for measuring non-destructively the amount of cold work in Type 316 stainless steel were undertaken. A series of seven rods, which has been subjected to various amounts of reduction by tensile elongation, were each drawn uniformly through a direct-current field of 20,000 G normal to the rod axis. The field retained in the rods appeared to have at least short-term stability and was surprisingly low compared with the field retained in Type 304 stainless steel under similar conditions. The rods were demagnetized as completely as possible, remagnetized, and the retained field was again measured. No systematic change in the amount of retained field at a given location was observed when this cycle was repeated several times. There appeared to be a reasonable correlation between the retained field and the percentage reduction of area of the tensile rods for reductions above 20% (see Figs. III.B.3 and III.B.4).

For reductions below 15%, no field could be detected by our magnetometer. Magnetometers that have an order of magnitude greater sensitivity are available, but the next logical step would seem to be to identify the constituent of the stainless steel that is contributing the magnetic effect. Diffraction experiments under way are expected to determine whether the magnetic effect is contributed by martensite.

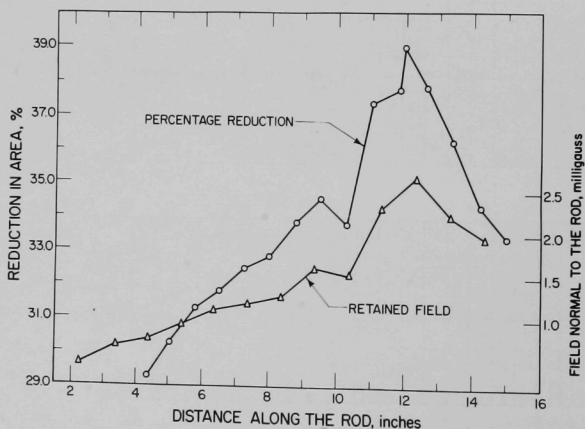


Fig. III.B.3. Percent Reduction and the Field Normal to the Rod as a Function of Distance along the Rod. Results from tensile rod 3.

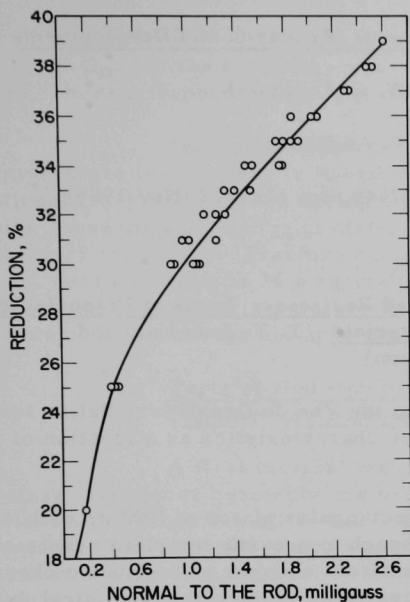


Fig. III.B.4

The Relationship between Percent Reduction and the Retaining Field Normal to the Rod. Results from 7 rods.

It would then be desirable to determine the effect of variations in the constituents of different heats of steel, with the Type-316 designation, on a possible nondestructive method for measuring cold work based on retentivity.

Equipment that will be able to make continuously scanned measurements of tensile-rod resistivity without interference from minor variations of the rod diameter is nearly complete. When complete, the equipment will be used to check the variation of resistivity with percentage reduction.

C. Engineering Development--Research and Development

1. Instrumentation and Control (W. C. Lipinski)

a. Boiling Detector (T. T. Anderson)

Last Reported: ANL-7640, pp. 116-117 (Nov 1969).

(i) Acoustic Method

(a) Irradiation and Resistance Tests of Piezoelectric and Insulator Materials (T. T. Anderson and S. L. Halverson)

The data from the Van de Graaff irradiation tests are being analyzed to obtain transducer characteristics as a function of irradiation conditions.

In addition, rectangular plates of lithium niobate have been irradiated at energies low enough to prevent complete penetration of the crystals by electrons. No significant changes of resonance characteristics were observed before or after irradiation, although optical examination showed evidence of internal stress through a change from a uniaxial to a biaxial optic axis. X-ray diffraction alignment of the plates showed one set of crystals, previously unused, to be X-cut rather than the specified Y-cut. Resonance measurements confirmed the absence of longitudinal modes, as expected for X-cut lithium niobate.

(b) Development of High-temperature Detector (T. T. Anderson and A. P. Gavin)

In fastening a lithium-niobate transducer assembly onto the end of a stainless steel bar, clamping pressure is used to couple the bar to the lithium niobate crystal acoustically. As clamping pressure is increased, acoustic sensitivity was observed to go through a maximum, while the mechanical quality factor (Q_m) decreased continually. For a perfect fit of the lithium niobate crystal to a stainless steel surface, the theoretical value of Q_m should be about unity. This excellent acoustic coupling is the result of a near match of lithium niobate acoustic impedance ($3.17\text{--}3.4 \times 10^6 \text{ g/cm}^2\text{-sec}$) to that of steel ($3.9 \times 10^6 \text{ g/cm}^2\text{-sec}$). However, for a freely vibrating crystal, Q_m is quite large ($\sim 10^6$).

The change of Q_m with compressive load has been observed for Y-cut lithium niobate in a screw-loaded transducer assembly and in a static-loaded fixture. The changes fit the empirical relationship $Q_m/Q_0 = \ln(\sigma_{22}/\sigma_0)$, where the constants for the two tests are, respectively,

$Q_0 = 10$ and 20 , and $\sigma_0 = 100$ and 400 kg/cm^2 . These results might explain variations in Q_m for the electron irradiations involving accelerator bombardment, where a trapped charge can induce significant internal stresses.

Another problem involving use of lithium niobate in high-temperature transducers is the tendency of crystals to fracture. An unintentional fracture occurred during edge-loading of a Y-cut crystal to determine cross-mode coupling of diametral resonances to the useful longitudinal axial resonance. Fracture occurred when the force was increased to 11.5 kg , corresponding to 14.6 kg/cm^2 had the force been applied across the thickness of the cylindrical wafer. Significantly, this is the compressive stress recently selected for clamped-transducer operation.

(c) Tests of High-temperature Detectors in Water, Furnace, and Sodium (A. P. Gavin)

A first thermal test of the screw-loaded high-temperature transducer assembly has been performed. Relative acoustic sensitivity (in the range $0\text{--}1 \text{ MHz}$) and impedance near resonance (3.4 MHz) were measured as the temperature was gradually raised to 1200°F in 100°F increments. The mechanical quality factor Q_m increased with temperature, indicating that the acoustic coupling was decreasing. At 900°F , there was a sudden degradation of acoustic response to the ultrasonic vibrations. Subsequent disassembly of the fixture showed that the crystal had fractured.

Cause of the fracture is unknown, but two possibilities are an applied shear stress at the crystal-steel interface or anisotropic thermal strains in the crystal. To eliminate the first of these, a new high-temperature transducer is being fabricated in which a pneumatic piston will apply a constant compressive force through a point-contact pivot to the optically flat stainless steel crystal holder. Furnace tests are planned for the new transducer.

b. Vibration Sensor (T. P. Mulcahey)

Last Reported: ANL-7618, pp. 106-107 (Sept 1969).

(i) Out-of-pile Tests of Sodium-immersible Commercial Transducers (T. T. Anderson and A. P. Gavin)

One of three sodium-immersible accelerometers will be selected for installation on an FFTF flow subassembly early in 1970. Impedance measurements have shown the mechanical quality factors (Q_m) to be about 400 , a factor of 4 above similar accelerometers without the integral sheathed cable, indicating a freer mechanical suspension. The manufacturer is calibrating the accelerometers as a function of temperature.

2. Heat Transfer and Fluid Flow (M. Petrick)

a. LMFBR Burnout Limitations (R. J. Schiltz and R. Rohde)

Last Reported: ANL-7640, p. 118 (Nov 1969).

(i) Preparation of Apparatus. A safety document package has been prepared and is being reviewed. The report describes details of the loop enclosure, piping, components, and the air-duct system; it also provides design details for review of the mechanical and structural aspects of the facility.

The main piping system assembly is ~50% complete. Part of the piping has been suspended from the piping hangers within the loop enclosure.

The piping for the 2-ft-dia air duct and the transition piece have been received and inspected. System installation is ~50% complete.

Operation of the heat-exchanger coil with maximum air flow showed a small amount of vibration, which has been eliminated by providing a damping device.

The head of the plenum was reworked to provide a thermal-transition piece at its center for the bypass flow. The plenum has been received and is ready for installation.

The core of the electromagnetic helical induction pump is ready for use.

The vacuum-pump support system that facilitates connection of the unit to the vacuum chamber has been completed. The vacuum pump has been connected to the vacuum chamber.

Fabrication of the oil cooling system for the pump is ~90% complete.

b. Nonboiling Transient Heat Transfer (R. P. Stein)

Last Reported: ANL-7632, p. 116 (Oct 1969).

(i) Analyses of Heat-flux Transients. The sodium-sodium heat exchanger loop (see Progress Report for February 1968, ANL-7427, p. 114) will be used in the transient heat flux experiment. However, the loop must be modified to accommodate the transient heat source, which will be an electron bombardment heater (EBH). Redesign of the loop and preliminary

drawings of the EBH have been completed. The costs of modifying the loop and fabricating the heater are being estimated.

The coefficients pertaining to the pin-bundle approximation have been computed (see Progress Report for August 1969, ANL-7606, p. 105) and are being checked.

c. Liquid-Metal Heat Transfer in Pin Bundles (T. Ginsberg)

Last Reported: ANL-7618, pp. 107-108 (Sept 1969).

Several available computer codes make use of the lumped-parameter approach to calculate temperature distributions in a pin bundle. The utility and accuracy of these codes depend, to a large degree, on the available data and correlations for interchannel mixing.

Interchannel mixing may be caused by: (1) natural turbulence, in a rod bundle with no spacers; or (2) flow sweeping, in bundles with helical spacers. The first of these mixing processes is considered below.

Although Rogers and Todreas* discussed the turbulent-mixing correlations that have been proposed, however, they did not present the correlations in graphic form. Figure III.C.1 shows the mixing rates predicted by the correlations. The following nomenclature is used: P is rod pitch, d is rod diameter, d_{ei} is hydraulic diameter (of subchannel i), c is rod-to-rod spacing, U_i is fluid velocity, μ is viscosity, ν is kinematic viscosity, $w_{i,k}$ is turbulent mixing rate between subchannels i and k , and $y_{i,k}$ is distance between centroids of channels i and k . The correlations are presented for mixing between adjacent subchannels with identical geometric configurations.

Rather large discrepancies between the mixing rates are predicted by the various correlations. The discrepancies are greatest for small P/d , which is the range of interest for liquid-metal reactors. A question arises as to what uncertainty is introduced into the lumped-parameter calculations of pin-bundle heat-transfer characteristics as a result of uncertainties in predictions of turbulent mixing rates.

Figure III.C.2 is a plot of the maximum surface-temperature difference around a rod adjacent to the hexagonal-can wall in a 19-pin fuel bundle versus the thermal mixing factor YEDH. HECTIC-III (a modified version of HECTIC-II)** was used to calculate the pin-bundle heat-transfer

*Rogers, J. T., and Todreas, N. E., Coolant Interchannel Mixing in Reactor Fuel Rod Bundles: Single-phase Coolants, Symposium on Heat Transfer in Rod Bundles, ASME (December 3, 1968).

**Katchee, N., and Reynolds, W. C., HECTIC-II, An IBM 7090 Fortran Computer Program for Heat Transfer Analysis of Gas or Liquid Coolant Reactor Passages, IDO-28595 (Dec 1966).

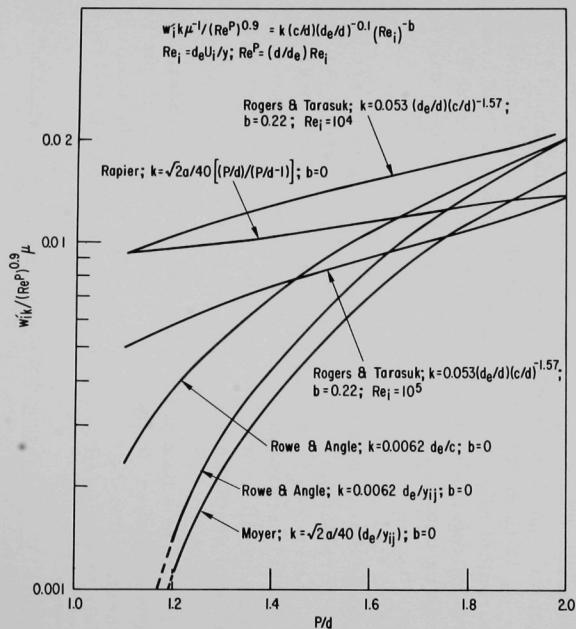


Fig. III.C.1. Mixing Correlations

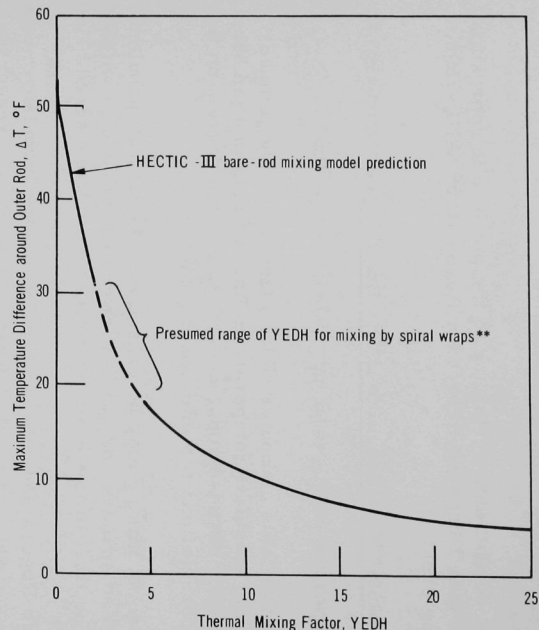


Fig. III.C.2. Effect of Thermal Mixing on Surface Temperature Variation around an Outer Rod in 19-pin Array (at bundle exit)

characteristics with input data of sodium, $P/d = 1.2$, $d = 0.303$ in., $q = 10$ kW/ft, $U = 27$ ft/sec, and $T_0 = 780^\circ\text{F}$. For a spacer-free rod bundle, YEDH is small, of order 1. In this portion of the curve, an uncertainty in YEDH of a factor of 2-3 leads to an uncertainty in ΔT of 25-40%.

Such results point to the need for evaluating the accuracy of the lumped-parameter calculations. Experimental subchannel temperature data are required for this evaluation, and such data have not yet been found in the literature.

d. Heat Transfer in Liquid-Metal Heat Exchangers (R. P. Stein)

Last Reported: ANL-7632, p. 120 (Oct 1969).

Additional computations have been performed with the data obtained from the sodium-to-sodium heat-exchanger experiments. The experiments were designed to investigate the effect of eccentric placement of the inner pipe of a double-pipe heat exchanger on the overall heat-transfer rate (heat-exchanger effectiveness). The effect of eccentric placement on heat-transfer rates was very small even though the outer-wall-temperature distributions were strongly affected.

The additional computations determined the circumferential distribution of local heat-transfer coefficients and average heat-transfer coefficients in the fully developed heat-transfer regions for an experiment with full eccentric placement (eccentricity = 1). The tube- and annulus-side Peclet numbers were 675 and 248. The heat-exchanger effectiveness was 0.48, which was only about 13% less than the value for concentric placement.

Calculated temperature and heat-flux distributions at the inner wall of the eccentric annular space are shown in Fig. III.C.3, where t denotes the temperature of the inner wall of the annular space, $t_{1,0}$ the tube-side-fluid inlet temperature, and q''

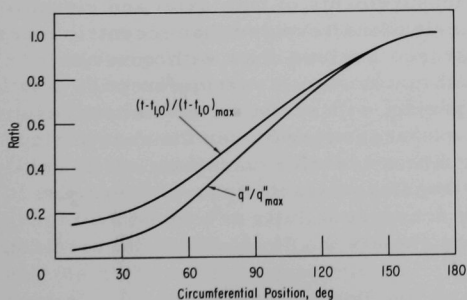


Fig. III.C.3. Calculated Inner-pipe Temperatures and Heat Fluxes vs Circumferential Position

the local heat flux. A circumferential position of 0 corresponds to the location where, for an eccentricity of unity, the inner and outer pipes were in contact; 180° corresponds to the position of maximum annular space. Local coefficients were based on the local heat flux, local wall temperature, and duct average fluid bulk temperature. Average coefficients were based on the average heat flux, the average wall temperature, and the fluid bulk temperature.

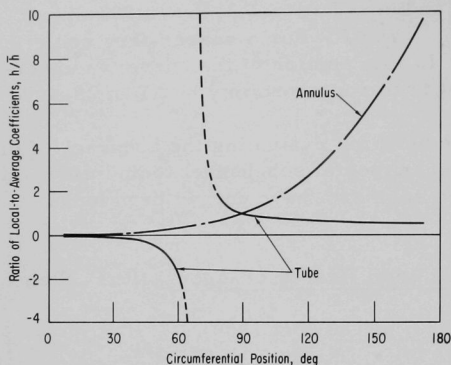


Fig. III.C.4. Calculated Local Heat-transfer Coefficient Ratio (h/\bar{h}) vs Circumferential Position

direction of the local heat fluxes is from the annulus side to the tube side. As a result, tube-side coefficients are negative in this region and exhibit an infinite discontinuity at a circumferential position of 70° , where wall and bulk temperature are equal. For circumferential positions larger than 70° , wall temperatures are larger than the bulk temperature; coefficients are positive and are nearly uniform over most of the remainder of the circumference. Annulus-side coefficients increase monotonically with circumferential position and become large when compared to the average value, but remain finite.

The average tube-side coefficient was found to be 25% less than the value computed from the Lyon-Martinelli equation. The average annulus-side coefficient was found to be 80% less than the value for concentric placement. Because of the small thermal resistance of the wall, these low values of the average coefficients would have a large influence on the fully developed overall heat-transfer coefficient. Measurements of both axial and circumferential outer-wall temperature distributions revealed that eccentric placement results in larger thermal-entrance regions than with concentric placement. Apparently, the additional mechanism of circumferential heat transfer, and larger local annular spacing, with eccentric placement results in a requirement of additional heat-exchanger length over the concentric case in order to attain fully developed heat-transfer conditions. It is concluded that the higher rates of heat-transfer characteristic of thermal-entrance regions compensate for the decrease in fully developed average heat-transfer coefficients and thereby explain the small effect of eccentricity on heat-exchanger effectiveness.

The report describing these investigations has been completed.*

*Bump, T. R., Stein, R. P., Featherstone, M. J., and Kimont, E. L., Effect of Eccentricity on Effectiveness of a Sodium-to-Sodium Double-Pipe Heat Exchanger, accepted for presentation at and publication in the Proceedings of the Fourth International Heat Transfer Conference, Versailles, France, August 31-September 5, 1970.

The ratios of local-to-average coefficients (h/\bar{h}) as functions of circumferential position are shown in Fig. III.C.4 for both the tube and annulus sides of the heat exchanger.

The tube- and annulus-side coefficients approach zero as the circumferential position approaches the region where the inner and outer tubes are in contact. Coefficients are small in magnitude because heat fluxes are very small near this region. For circumferential positions between 0 and 70° , tube-side wall temperatures are smaller than the tube-side bulk temperature, even though the

3. Engineering Mechanics (G. S. Rosenberg)

a. Advanced Thermoelasticity (R. A. Valentin)

Last Reported: ANL-7632, p. 121 (Oct 1969).

(i) Solution of End-effect Problems Involving Nonplane Stress Fields in Short Cylinders and Contact Stresses between Cladding and Fuel.
The mathematical analysis of the symmetric deformation of a finite cylinder having a perfectly bonded cladding has been completed. The associated computer programs are being debugged.

(ii) Techniques of Numerical Approximation

Not previously reported.

A survey of available finite-element codes applicable to the class of thermoelasticity problems of interest is being completed. Initial reprogramming of one such code is in progress; various test problems are being formulated. Consideration is being given to the use of a form of general-purpose orthonormalization code to supplement the finite-element method in handling those problems for which an analytical approach would not be justified due to the excessive time necessary for solution.

D. Chemistry and Chemical Separations

1. Fuel Cycle Technology--Research and Development

a. Adaptation of Centrifugal Contactors to LMFBR Processing (G. J. Bernstein)

Not previously reported.

A new program has been instituted to extend centrifugal mixer-settler design to a configuration suitable for solvent extraction of LMFBR fuels. The advantages sought are geometric control of criticality, reduced radiation damage to solvent (as a result of reduced residence time in the contactor), and increased ease of operation (including rapid flushouts). The scope of the program includes review studies of the design and performance of existing centrifugal mixer-settlers, particularly the Savannah River units, and correlation of performance with size and speed to serve as a starting point for the design and fabrication of an experimental unit of variable speed and the high length-to-diameter ratio generally necessary for criticality control. The experimental unit will have a maximum diameter of about 4.5 in. Several alternative designs of mixer-settlers will be considered, with the objective of simplifying construction and operation.

The program also includes operation of the experimental unit. Correlation and consolidation of the information obtained will allow design of a prototype that can be adopted by industry. Hydraulic capacity and mass-transfer rates will be measured with natural uranium solutions; no plutonium or fission products will be used.

Initial investigations are under way with plastic models of a simplified contactor construction. In this design, a hollow cylindrical rotor spins within a fixed, vertical cylindrical tube. The mixing chamber consists of the annular space between the rotor and the tube. The organic and aqueous phases enter at the top of the annulus and are mixed by skin friction or by means of blades on the rotor and baffles on the fixed tube as they flow downward through the annular chamber. The mixed phases leave the annulus and enter the hollow rotor (the centrifugal bowl) through an orifice in the bottom of the rotor; the organic and aqueous phases are separated by a centrifugal force as they move upward inside the rotor, and are discharged through appropriate ports at the top of the rotor. An expected advantage of the annular mixing chamber is that flow through it approximates plug flow, despite the mixing, and the chances are small that any part of the inlet streams will bypass the mixing zone. Equipment of this general type will be used to investigate phase mixing and separating performance in independent units as well as in a single unit combining both functions.

The first model was used with water to measure the mixing power input. By sealing the rotor inlet orifice, the system was made non-flowing and no power was used for pumping. The OD of the rotor was $2\frac{3}{4}$ in.; the fixed tube had an ID of $3\frac{1}{4}$ in. For this small unit with a smooth rotor and fixed tube, the mixing power input was about 1×10^{-3} hp at 800 rpm and 1.7×10^{-2} hp at 2100 rpm. Over the same range of mixing speeds, the power input with six blades and eight baffles installed was about six times the power input in their absence. On the basis of these tests, it is anticipated that the desired mixing intensities can be achieved in a full-scale unit while avoiding excessive emulsification.

Construction of a plastic unit having a 3-in.-OD rotor spinning within a $3\frac{5}{8}$ -in. stator is nearly complete. This unit has an internal ring dam which will permit measurement of flow rates of a single phase under conditions simulating actual operation. A full-scale plastic and stainless steel contactor is being designed to permit testing under two-phase flow conditions.

b. Molten Metal Decladding (R. D. Pierce)

(i) Engineering Development

Last Reported: ANL-7632, pp. 123-124 (Oct 1969).

(a) Plutonium and Uranium Recovery. A decladding process is under study in which stainless steel cladding is first dissolved in liquid zinc

having an overlying salt layer, and the resulting metal solution is then separated from the unreacted oxide fuel. (This process may also be applicable for Zircaloy cladding.) The oxide is subsequently dissolved in nitric acid in a separate vessel for feeding to an aqueous process.

Earlier, various cover salts were considered for the decladding step, and LiF-35 mole % NaF-10 mole % CaF_2 eutectic was selected for the initial experiments (ANL-7632, p. 124). A cover salt is proposed to suppress zinc vaporization. An experiment has been performed to measure the cosolubility at 750 to 850°C of powdered uranium oxide and plutonium oxide in the selected cover salt with and without zinc present. Samples taken of the final salt solutions are being analyzed for uranium and plutonium.

(ii) Process Demonstration Experiments

Last Reported: ANL-7618, pp. 114-115 (Sept 1969).

Small-scale experiments are being performed to develop experimental techniques for measuring the dissolution-disintegration rate of stainless steel in zinc as a function of several process variables, such as speed of agitation and concentration of stainless steel in zinc. These data will be used in designing experiments on a larger scale. The best procedure for determining dissolution-disintegration rates has been found to be a short exposure of a stainless steel sample to the decladding solution, followed by (1) vacuum retorting at 750°C to remove adhering zinc and (2) weighing to determine weight loss.

Four runs of 15- or 30-min duration were performed at 800°C and with 0, 50, or 100 rpm agitator speeds. Tentative conclusions are that the dissolution-disintegration rate of Type 304 stainless steel increases with agitator speed and is unaffected by concentrations of dissolved stainless steel in the melt up to 4 wt %.

Engineering-scale equipment originally intended for demonstration experiments of the salt-transport process has been completed for use in decladding studies with about 10 kg of simulated reactor fuel. Shake-down experiments are under way.

c. Continuous Conversion of U/Pu Nitrates to Oxides (N. M. Levitz)

Not previously reported.

Conversion of uranium nitrate and plutonium nitrate solutions (produced in reprocessing plants) to an oxide form is a necessary and presently expensive step in the nuclear fuel cycle. This conversion must

provide the fuel fabricator with powdered fuel oxides suitable for the fabrication of fuel shapes. In addition, conversion of fissile nitrate solutions (including plutonium nitrate solutions) to a powder form is, in itself, of interest since powder is more easily and safely shipped.

Current conversion processes consist of a number of steps, among which are precipitation, filtration, and calcination. An alternative to these processes, which offers potential economic advantage, is continuous fluid-bed denitration of uranium-plutonium nitrate solutions to a $\text{UO}_3\text{-PuO}_2$ powder form, followed by fluid-bed reduction to $\text{UO}_2\text{-PuO}_2$. This process is based on extensive fluid-bed denitration technology developed for uranyl nitrate and waste aluminum nitrate solutions.* An integrated laboratory and pilot engineering-scale experimental program has been planned.

The laboratory program is directed toward an early characterization (composition and structure) of the products from (1) denitration of U-20% Pu feed solutions and (2) hydrogen reduction. In addition, the stability toward precipitate formation of U-Pu feed solutions over a range of compositions will be studied. Laboratory-scale drop-denitration experiments are being performed to develop procedures and techniques for the denitration of uranium-plutonium nitrate solutions.

The size and type of equipment for engineering-scale denitration of uranium-plutonium nitrate solutions have been selected. Equipment being obtained or designed includes the denitrator with internal filters, a secondary filter outside the denitrator, a condenser for recovering nitric acid from the off-gas, a demister, a heater, a high-efficiency filter, and associated items (i.e., feed and product-withdrawal systems, and instrumentation). The nitric acid will be removed from the process off-gas in a condenser rather than disposed of by scrubbing with caustic or sorption on a solid. Advantages of condensing in this experimental setup are (1) the acid can be used to dissolve product urania-plutonia, allowing recycle of this material to the denitrator, (2) fewer liquid transfers out of and into the alpha box will be required, and (3) condensation appears to be simpler and cheaper than the other two methods.

Because of the broad experience with cylindrical columns in earlier denitration work, initial investigations will be done with a 4-in.-dia cylindrical fluid-bed denitrator of stainless steel construction, which is considered critically safe for feeds containing up to 20% plutonium. The denitrator will have internal filters and an external-mix spray nozzle, and will be heated by high-density Watlow heaters that are metal-bonded to the outside denitrator surface and are capable of delivering 26 kW of heat. A parallel effort will be the development of a slab-shaped column, which offers nuclear criticality advantages upon scale-up of high-plutonium systems.

*Jonke, A. A., Petkus, E. J., Loeding, J. W., and Lawroski, S., Nucl. Sci. Eng. 2, 303 (1957).

d. In-Line Analyses in Fabrication (M. J. Steindler)

Not previously reported.

The cost of fabrication represents a major portion of the total fuel-cycle cost for power reactors, and the competitive economic position of power production from nuclear reactors requires that such costs be reduced. Rigorous specifications have been set for FBR fuels. Because of the rigor of the fuel specifications, analytical methods and their application to the fabrication process and to the product have assumed great importance to the economics of the fuel cycle. The development of analytical methods capable of determining the physical and chemical properties of the fuel with the precision and accuracy required by the performance-property relationship is quite important.

Continuous in-line analytical methods are desirable for process control and product analysis in large-capacity fabrication plants that are to operate on a sound economic basis. The accuracy and precision of such analytical methods will affect the fraction of acceptable material produced, and thus influence the overall cost of the fabricated fuel. However, it may not be possible or desirable to use continuous in-line procedures always. If this is the case, more conventional methods will be considered.

The U/Pu ratio is an important fuel property, and its determination will be a part of any conceivable fabrication procedure. In-line X-ray fluorescence analysis of the U/Pu ratio may be suitable for application to this problem. X-ray fluorescence analysis is a sensitive, non-destructive method in which exciting radiation (from an X-ray tube or radioactive source) impinges on the sample and causes the emission of radiation that is characteristic of the elements present; by this method, uranium and plutonium concentrations can be determined rapidly and accurately.

The relationship of the appropriate emission peaks for thorium and uranium is similar to that for uranium and plutonium. Hence results for urania-thoria should be applicable to urania-plutonia fuel mixtures without the plutonium hazards. Preliminary analyses on 2.5% UO_2 -97.5% ThO_2 pellets have been carried out by X-ray fluorescence methods to demonstrate the analytical method. Preliminary results indicate the feasibility of this method for analysis.

2. General Chemistry and Chemical Engineering--Research and Development

a. Thermophysical Properties

- (i) Partial Pressures of Vapor Species in the U-Pu-O System and in the U-Pu-O System Containing Fission Products
(J. E. Battles and P. E. Blackburn)

Last Reported: ANL-7618, pp. 115-116 (Sept 1969).

Mass-spectrometric studies of the vaporization of the uranium-plutonium-oxygen LMFBR fuel are being made to determine the equilibrium pressures of the vapor species as functions of temperature and oxygen concentration. These data are required (i) to establish whether migration occurs within the fuel by vapor transport and (ii) to determine metal and oxygen activities of the fuel. These activities are important in determining the nature of fission products (i.e., their presence as oxides, alloys, or elements), particularly those corrosive to cladding or those contributing to fuel swelling. The data will be used to establish methods for controlling cladding attack and some aspects of fuel swelling. The program will first concentrate on the pure fuel, i.e., $U_{0.8}Pu_{0.2}O_{2\pm x}$, corresponding to zero irradiation. Studies will then be made of simulated irradiated fuel with fission products.

A traverse experiment (similar to that reported in the Progress Report for June 1969, ANL-7581, p. 113) using an iridium effusion cell has been completed. The sample (0.7 g of $^{235}UO_2$ -20 wt % PuO_2) was heated at $\sim 2264^\circ K$ for 13 hr while monitoring the ion intensities resulting

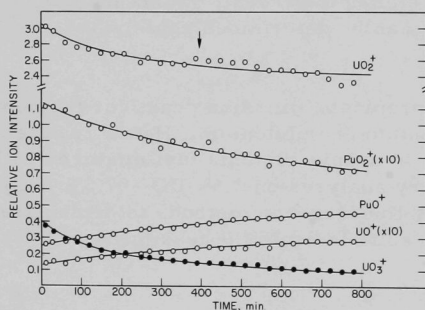
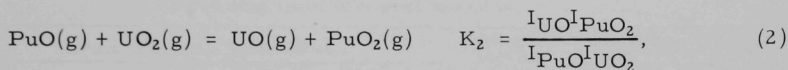


Fig. III.D.1. Variations of the Intensities of UO_2^+ , UO_3^+ , PuO_2^+ , and PuO^+ as a Function of Time at Constant Temperature ($\sim 2264^\circ K$). (The O/M atom ratio was 1.973 at start of experiment and 1.945 at conclusion.)

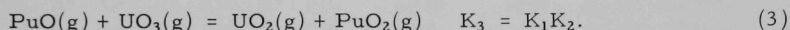
from ionization of the vapor species UO , UO_2 , UO_3 , PuO , and PuO_2 --the only species detected. The variation of the measured ion intensities as a function of time is shown in Fig. III.D.1. The ion intensities were determined using an ionizing electron energy of 15 eV for UO_3^+ and PuO_2^+ , and 11 eV for UO^+ , UO_2^+ , and PuO^+ . Since the electron energies (E) are 5 to 6 eV greater than the respective appearance potentials (AP), no correction for the difference between E and AP was necessary (see Progress Report for April 1968, ANL-7445, pp. 124-127). The variations of the ion intensities during the experiment, i.e., the

decrease for UO_3^+ , UO_2^+ , and PuO_2^+ and the increase for UO^+ and PuO^+ , are consistent with the observed decrease in the O/M atom ratio of the condensed material from 1.97₃ to 1.94₅. The arrow in Fig. III.D.1 indicates the point at which the sample was cooled to room temperature overnight.

Since the vapor and condensed phases were undergoing gradual changes, an indication of equilibrium or nonequilibrium behavior can be obtained by determining the equilibrium constants for the vapor-phase reactions



and



The equilibrium constants calculated for the above reactions were constant when plotted as a function of time, thereby increasing the confidence in the reliability of the measurements of temperature dependency and effusion rate.

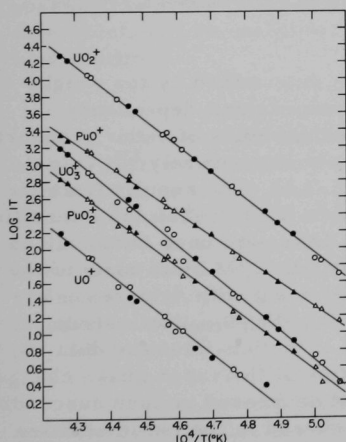


Fig. III.D.2

Variation of Intensities of UO^+ , UO_2^+ , UO_3^+ , PuO^+ , and PuO_2^+ Observed over UO_2 - PuO_2 as a Function of Reciprocal Temperature. (O/M = 1.96₄) Run IUP-4A-5.

The temperature dependency of the vapor species over the mixed oxide material ($^{235}\text{UO}_2$ -20 wt% PuO_2) was determined in a series of experiments using an iridium effusion cell and a large sample (~1.5 g initially). The variation of the ion intensity as a function of reciprocal temperature (log IT versus $1/T$) for a typical experiment is shown in Fig. III.D.2. The experimental procedure was the same as previously reported (see Progress Report for October 1968, ANL-7513, pp. 127-130). The partial enthalpies of sublimation were determined from the slope of a least-squares fit of the data. The values are summarized in Table III.D.1. The compositions (O/M atom ratios) shown in Table III.D.1 for the solid phase were determined prior to the temperature-dependency measurements. As discussed above, the ion intensities of the several species changed considerably as the O/M atom ratio of the solid phase decreased

from 1.97₃ to 1.94₅. Similarly, the composition of the vapor and solid phases underwent small changes during the temperature-dependency measurements, which resulted in considerable scatter in the measured ion intensities, particularly for the minor species. Consequently, the standard deviations in the measured enthalpies are larger than normal. Also, the low intensity of UO^+ (over most of the temperature range) leads to considerable uncertainty in the accuracy of the enthalpy obtained for this species. Since the composition of the solid phase changed continuously during this series of measurements, a similar variation might be expected in the enthalpies for the several species. The data in Table III.D.1 indicate such a trend in the enthalpy of UO_2^+ , whereas the trend is not apparent in the data for the other species (UO^+ excluded).

TABLE III.D.1. Mass Spectrometrically Determined Partial Enthalpies of Sublimation for the Vapor Species in the Ternary System U-Pu-O.

Run No.	Temperature Range (°K)	Composition of Solid Phase (O/M)	Partial Enthalpy ^a of Sublimation (kcal/mol)				
			PuO	PuO ₂	UO	UO ₂	UO ₃
IUP-4A-1	1959-2299	1.97 ₃ -2.00 ₄	125.87 ± 2.84	130.72 ± 2.09		148.15 ± 1.79	159.14 ± 3.43
IUP-4A-3	1938-2263	1.97 ₃	126.10 ± 2.23	137.41 ± 2.08	132.38 ± 4.57	149.06 ± 0.67	162.07 ± 1.82
IUP-4A-5	1928-2290	1.96 ₄	123.06 ± 1.34	140.35 ± 1.25	138.36 ± 2.87	148.05 ± 0.86	160.49 ± 1.89
IUP-4A-7	1971-2350	1.96 ₂	126.73 ± 1.27	140.05 ± 1.64	143.13 ± 3.87	146.34 ± 0.99	154.83 ± 1.70
IUP-4A-9	1994-2387	1.90 ₉ ^b	122.61 ± 1.57	138.70 ± 2.25	154.54 ± 5.40	144.60 ± 1.30	157.66 ± 2.48
IUP-4A-11	2093-2370	1.93 ₄	120.25 ± 2.42	138.14 ± 2.12	126.47 ± 3.67	143.79 ± 1.63	155.77 ± 2.22

^aThe errors listed are standard deviations; an ionizing electron energy of 11 eV was used for measurements of PuO^+ , UO^+ , and UO_2^+ , whereas 15 eV was used for measurements of PuO_2^+ and UO_3^+ .

^bThe oxygen analysis for this sample is believed to be incorrect.

The rate of mass effusion was determined by the weight-loss method in an alternate series* with the temperature-dependency measurements. From the rates of mass effusion, values of vapor pressure were calculated on the basis that the vapor phase was entirely $^{235}\text{UO}_2(\text{g})$; $\text{UO}_2(\text{g})$ is the major vapor species (see Fig. III.D.2). The results from the several measurements are summarized in Table III.D.2. The ion intensities determined during the effusion measurements have also been included. In the series of measurements concluded thus far, the O/M atom ratio of the solid phase decreased in each succeeding experiment with a decrease in the total vapor pressure. The pressure over $\text{Pu}_{0.2}\text{U}_{0.8}\text{O}_{1.938}$ was about one half of that over $\text{Pu}_{0.2}\text{U}_{0.8}\text{O}_{1.973}$. Analysis of the ion-intensity data (see Table III.D.2) indicates that the composition of the vapor phase changed appreciably as the O/M atom ratio of the solid decreased in each succeeding experiment. The most significant changes occurred in the ion intensities of PuO^+ , UO^+ , and UO_3^+ .

*Using the same sample, IUP-4A, the even and odd numbered experiments are vapor pressure and temperature-dependency measurements, respectively.

TABLE III.D.2. Total Vapor Pressure and Ion Intensities
for the Vapor Species in the Ternary System U-Pu-O

Run No.	Temp (°K)	Composition ^a of Solid Phase (O/M)	Pressure (atm)	Ion Intensity ^b				
				PuO ⁺	PuO ₂ ⁺	UO ⁺	UO ₂ ⁺	UO ₃ ⁺
IUP-4A-2	2241	1.97 ₃	1.45 × 10 ⁻⁵	0.057	0.034	0.003	0.777	0.130
IUP-4A-4	2242	1.96 ₄	1.15 × 10 ⁻⁵	0.076	0.029	0.003	0.799	0.095
IUP-4A-6	2239	1.96 ₂	9.78 × 10 ⁻⁶	0.095	0.027	0.005	0.803	0.070
IUP-4A-8	2240	1.95 ₂	8.18 × 10 ⁻⁶	0.142	0.025	0.006	0.786	0.041
IUP-4A-10	2240	1.909 ^c	7.45 × 10 ⁻⁶	0.175	0.024	0.008	0.765	0.028
IUP-4A-12	2239	1.934	7.031 × 10 ⁻⁶	0.196	0.022	0.010	0.751	0.021

^aThe O/M atom ratio was determined from samples taken at the conclusion of the experiment.

^bThese values represent the fraction of the total ion current. The ion currents were corrected for isotopic composition. Corrections for ionization cross sections and multiplier efficiency were not made.

^cThe oxygen analysis for this sample is believed to be incorrect.

- (ii) Phase Diagram of the U-Pu-O System Containing Fission Products (Nonradioactive) (H. Chen, I. Johnson, and P. E. Blackburn)

Last Reported: ANL-7618, pp. 117-118 (Sept 1969).

Among the many factors possibly related to the failure of fuel in fast-breeder reactors are chemical reactions between the fuel matrix, the fission product elements, and the cladding materials. The purpose of this study is to obtain for these chemical processes thermodynamic data which will be useful for the design of fuel systems having a suitably long lifetime.

Analyses of irradiated oxide fuel suggest that iodine and cesium, which can penetrate the grain boundaries of stainless steel, have a close relation to the corrosion of the cladding. The possibility of transport of iron by iodine from the stainless steel cladding into the fuel by a Van Arkel-de Boer type of process is under study. As previously reported (ANL-7618), it has been experimentally observed that at 900°C free iodine is released from CsI + UO_{2+x} when $x \geq 0.18$, and the free iodine will attack stainless steel, giving intergranular corrosion similar to that observed in irradiated fuel (see Progress Report for April-May 1969, ANL-7577, pp. 144-149).

In a further investigation of the nature of the chemical reaction between CsI and UO_{2+x}, mixtures of the two compounds were heated to 825°C in fused silica tubes. The tubes had small capillary openings at one end to permit the escape of the iodine product and the unreacted CsI. The samples of UO_{2+x} that were used had values of x between 0.002 and 0.667. The extent of reaction, as determined from the gain in weight of the uranium oxide, was nearly linearly proportional to the value of x . For the experiments in which < 5 at. % cesium was retained in the oxide

matrix, X-ray examination of the reaction product indicated the presence of only the uranium oxide phases (UO_{2+x} , U_4O_9 , or U_3O_8) which would be expected from the value of x . However, when 5 at. % or more of cesium was retained in the oxide matrix ($x \geq 0.3$), several weak X-ray lines were observed which could not be attributed to these uranium oxides. These lines were found to correspond to the strong lines reported* for the product formed by the calcination of Cs_2UO_4 at 1000°C in air. The structure and composition of this decomposition product have not been established; however, it is apparently more stable than Cs_2UO_4 with respect to the reaction with iodine and is capable of retaining significant quantities of cesium at high temperature even at a relatively high iodine activity. Thermodynamic analysis indicates that cladding corrosion by a Van Arkel-de Boer transport process as proposed is very likely to occur for a fuel system with an initial O/M ratio very close to 2. Further experiments are planned to establish the stability of this Cs-U-O ternary compound at the low oxygen partial pressures characteristic of reactor fuel systems.

PUBLICATIONS

Your Own Personal Neutron Radiography Set?

J. P. Barton and M. F. Klozar

Mater. Eval. 27, 12A (Dec 1969) Tech. Note

A Model for Void Formation in Metals Irradiated in a Fast-neutron Environment

Samuel D. Harkness and Che-Yu Li

ANL-7588 (Aug 1969)

A Method for the Purification of Molten Chloride Salts

T. R. Johnson, F. G. Teats, and R. D. Pierce

ANL-7603 (Aug 1969)

The Reduction of Time-of-Flight Errors in Pulsed Neutron Measurements

J. W. Meadows

Nucl. Instr. Methods 75, 163 (1969)

Fast Neutrons Incident on Vanadium

Alan B. Smith, James F. Whalen, and Kenji Takeuchi

ANL-7564 (May 1969)

Preliminary Analysis of Defects in Metals

D. L. Waidelich

ANL-7587 (July 1969)

*Spitsyn, V. I., Ippolitova, E. A., Efremova, K. M., and Simanov, Yu. P., Investigations in the Field of Uranium Chemistry, ANL-Trans-33, pp. 142-147 (1961).

The Elastic Interaction between a Straight Dislocation and a Bubble or a Particle

R. W. Weeks, S. R. Pati, M. F. Ashby,* and P. Barrand**

Acta. Met. 17, 1403-1410 (Dec 1969)

A Fast Neutron Automated Data Acquisition System

J. F. Whalen

Proc. Skytop Conf. on Computer Systems in Experimental Nuclear Physics. USAEC Report CONF-690301 (Oct 1969), pp. 77-89

Compatibility of Uranium-5 w/o Fission Alloy with Types 304L and 316 Stainless Steel

S. Thomas Zegler, Howard V. Rhude, Jr., and John A. Lahti

ANL-7596 (Sept 1969)

A Conceptual Design Study of a Fluoride-volatility Plant for Reprocessing LMFBF Fuels

ANL-7583 (July 1969)

The following appeared as Abstracts in Trans. Am. Nucl. Soc. 12(2) (Nov 1969):

Reprocessing of Simulated Fast Breeder Fuel (UO_2 -20 wt % PuO_2) Using Fluoride Volatility Methods

L. J. Anastasia and M. J. Steindler

p. 446

Hydraulic Impedance: A Tool for Predicting Boiling Loop Stability

T. T. Anderson

p. 833

Thermal-Neutron Radiography with ^{252}Cf and Other Small Sources

J. P. Barton and M. F. Klozar

p. 465

Properties and Irradiation Behavior of Th-U-Pu Alloys

B. Blumenthal, D. R. O'Boyle, and W. N. Beck

p. 558

Explosive Technique for Pressure Pulse Testing of Reactor Components

B. L. Boers

p. 828

Mechanical and Thermal Analysis of Cylindrical Fuel Elements during Off-Normal Conditions after Extended Burnup

T. R. Bump

p. 534

* Harvard University.

** University of Manchester, England.

Glove Box Facility for Pyrochemical Research and Development
Work with ^{238}Pu

Jack Fischer
p. 848

Theories of Swelling and Gas Retention in Ceramic Fuels

B. R. T. Frost
p. 528

An Analysis of Fast-Neutron Effects on Void Formation and Creep
in Metals

S. D. Harkness, R. B. Poeppel, J. A. Tesk, and C.-Y. Li
p. 523

Studies in Mixed-Oxide Irradiated Fuels: Transport of Cladding
Components

C. E. Johnson, C. E. Crouthamel, H. Chen, and P. E. Blackburn
p. 565

A Titanium Gettering System for Purification of Glove Box Atmospheres

M. L. Kyle, R. D. Pierce, and K. R. Tobias
p. 859

Compatibility of Carbide Fuels with Potential LMFBR Claddings

T. W. Latimer, L. A. Neimark, C. E. Johnson, and C. E. Crouthamel
p. 594

Some Considerations of the Behavior of Fission-Gas Bubbles in Mixed-
Oxide Fuels

C.-Y. Li, S. R. Pati, R. B. Poeppel, R. O. Scattergood, and
R. W. Weeks
p. 531

Theory of Neutron Cross Sections for Shielding

P. A. Moldauer
p. 921

Neutron Energy Spectra for Fast Reactor Irradiation Effects

D. Okrent, J. M. Kallfelz, W. B. Loewenstein, A. D. Rossin,
A. B. Smith, and B. A. Zolotar
p. 701

The Fission Cross Section Ratio of ^{239}Pu and ^{235}U in the Neutron Energy
Range 150 to 1400 keV

W. P. Poenitz
p. 742

Irradiation Behavior of U-Pu-Zr Fuel Elements in EBR-II

H. V. Rhude, W. M. Murphy, and R. Natesh
p. 557

High-Temperature Stress Relaxation in UO_2

J. T. A. Roberts

p. 552

Liquid-Metal Decladding Processes for Fast Breeder Fuel Reprocessing

W. J. Walsh, R. D. Pierce, and R. K. Steunenberg

p. 445

Flow-Velocity-Dependence of Damping in Parallel-Flow-Induced
Vibration

M. W. Wambsganss and P. L. Zaleski

p. 839

IV. NUCLEAR SAFETY RESEARCH AND DEVELOPMENT

A. LMFBR Safety--Research and Development

1. Accident Analysis and Safety Evaluation

a. Disassembly Accidents and Post-burst Events (G. J. Fischer)

Last Reported: ANL-7606, pp. 123-124 (Aug 1969).

(i) Criticality of the FFTF during Meltdown. Calculations have been made to determine the amount of supercriticality of the FFTF reactor core through slumping induced by decay heat of fission products. Two-dimensional calculations were performed using 29 groups, averaged by heterogeneous MC² calculations for the FFTF spectrum. The following configurations were investigated:

1. Complete meltdown of the core, with homogeneous mixing of the inner and outer core fuel zones, as well as the upper and lower nickel reflectors. Responding to the increase in the density of the core, the reactivity increases by approximately 7% on collapsing approximately 15 cm.

2. Complete meltdown and separation of steel and fuel (e.g., by gravitational forces and/or by boiling of steel) would cause a reactivity increase of approximately 30%.

3. Substitution of the nickel in the upper and lower reflector by depleted UO₂ showed a less severe reactivity increase (18% instead of 30%) during meltdown, since no separation of the core from blanket materials can be expected. This form of mixing could be exceptionally important for reactors of sizes appropriate to 1000-MWe designs as a potential way to prevent supercriticality on slumping.

2. Coolant Dynamics (J. F. Marchaterre)

a. Sodium Simulations (M. A. Grolmes and H. K. Fauske)

Last Reported: ANL-7618, pp. 124-125 (Sept 1969).

(i) Expulsion of Nonmetallic Fluids from Single-tube Geometries (Static Tests). Our previously described expulsion experiments employed nonmetallic fluids to simulate the transient flashing behavior of liquid metals in confined geometries. The main reason for using nonmetallic fluids was to observe the flow patterns. With the appropriate flow regimes determined, analytical models can be formulated to predict the rate of void growth and collapse within the coolant channel, and the models can be tested with liquid-metal data.

In the selection of simulation criteria for liquid metals at low pressures, at least the effects of high thermal diffusivities, superheating, and large liquid-to-vapor density ratios should be considered.

The ratio of liquid to vapor density,

$$\left(\frac{\rho_l}{\rho_g}\right)_{LM} / \left(\frac{\rho_l}{\rho_g}\right)_{NM} \approx 1, \quad (1)$$

is an important parameter in modeling any two-phase flow regime. To obtain similarity of density ratio with liquid metals (LM) at atmospheric pressure, common nonmetallic fluids (NM) must be compared at sub-atmospheric pressures.

The ability of the alkali liquid metals to sustain large superheats before nucleation results from their intense wettability and physiochemical interactions with the heating surface (cleaning action), as well as thermophysical properties. From the formula expressing the excess vapor pressure in a cavity required for nucleation, the following criterion can be considered to contribute to the similarity of liquid metal and non-metallic fluid:

$$\left(\frac{\sigma T_{sat}}{h_{fg} \rho_g}\right)_{LM} / \left(\frac{\sigma T_{sat}}{h_{fg} \rho_g}\right)_{NM} \approx 1. \quad (2)$$

For liquid-to-vapor density ratios characteristic of sodium for 1-3 atm, it can be shown that Freon-11 or Freon-113 come very close to satisfying relation (2). In addition, experience has shown that Freon-11 wets and cleans glass surfaces extremely well. Superheats up to 150°F have been obtained readily after only modest cleansing of the glass beforehand; similar results can be obtained with water only after extensive degassing and cleansing of surfaces with chromic acid.

The large thermal diffusivities of liquid metals result in rather shallow radial-temperature gradients in the coolant channel before nucleation and rapid vapor growth immediately after nucleation. With substantial superheating, the former effect will lead to net boiling (saturated boiling) for a liquid metal, but a nonmetallic fluid subjected to an equivalent heat flux* and less superheat incurs subcooled boiling and different flow patterns. That situation can be avoided in nonmetallic fluids if depressurization (rapid or slow) is employed to superheat the fluid with no radial

*Heat flux similarity is assured by the criterion

$$\left(\frac{q}{h_{fg} \rho_g}\right)_{LM} / \left(\frac{q}{h_{fg} \rho_g}\right)_{NM} = 1.$$

temperature gradients. The inertia-limited vapor growth associated with superheated liquid metals at low pressures causes local pressurization that tends to deactivate other potential nucleation sites, and therefore favors the growth of a single bubble. On the other hand, a fluid of low thermal conductivity might experience considerably slower vapor growth, so that little or no pressurization occurs, resulting perhaps in the nucleation of many bubbles. Thus the simulation of the early vapor growth rate appears necessary to model correctly the flow pattern in a superheated liquid metal. With the equation of motion of a liquid column of height L_0 in a confined channel of equivalent diameter D_0 (the motion of the column being due to a growing bubble), together with the Plesset-Zwick equation for bubble growth rate (asymptotic conduction solution), the criterion

$$\left(\frac{Ja^2 \alpha \rho_\ell L_0}{D_0^2 (P_{\text{sat}} - P_0)} \right)_{\text{LM}} \bigg/ \left(\frac{Ja^2 \alpha \rho_\ell L_0}{D_0^2 (P_{\text{sat}} - P_0)} \right)_{\text{NM}} \approx 1 \quad (3)$$

indicates a similar initial vapor growth rate. Thus, with liquid-to-vapor density ratio, superheat, and geometric similarity, Table IV.A.1 illustrates to what degree some common nonmetallic fluids satisfy Eq. (3). As a result of the previous characteristics cited, together with the excellent vapor growth simulation illustrated in Table IV.A.1, Freon-11 and Freon-113 have been used as the principal simulants in our ongoing experiments.

TABLE IV.A.1. Illustration of Simulation
of Vapor Growth Rate

Na/NM	$\left(\frac{Ja^2 \alpha \rho_\ell}{P_{\text{sat}} - P_0} \right)_{Na} \bigg/ \left(\frac{Ja^2 \alpha \rho_\ell}{P_{\text{sat}} - P_0} \right)_{NM}$
$Na/F-11^a$	≈ 1
Na/H_2O	≈ 20
Na/CH_3OH	≈ 14

^aF-113 is equally suitable.

Experimental data, ranging in initial superheats from 50 to 130°F, were obtained recently for the slug expulsion of Freon-113 from a constant-diameter channel. The energy and momentum equations are coupled numerically in analyses of the expulsion problem. The energy equation accounts for not only the energy transported across the upper and lower liquid-vapor interfaces, but also that transported across the wall film-vapor interface. In calculating the energy contribution of the wall film, a thin thermal boundary layer was assumed to exist. The variation in the thickness of the thermal boundary layer as a function of exposure time and position along the vapor space was taken into account. The good agreement

between the experimental data and the coupled solution is indicated in Fig. IV.A.1, in which the uncoupled energy and momentum solutions are presented for comparison.

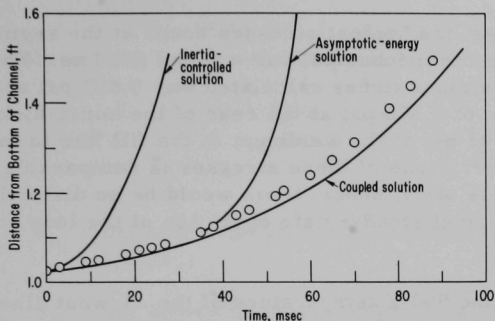


Fig. IV.A.1

Comparison of Measured and
Calculated Vapor-slug Growth.
Initial Superheat = 59°F.

3. Fuel Meltdown Studies with TREAT

a. Experimental Support (C. E. Dickerman)

Last Reported: ANL-7640, pp. 130-136 (Nov 1969).

(i) Stress Analysis of Mark-II TREAT Loop with Dump Tank.

The "B-3" Mark-II TREAT loop, to be used for the first loop experiment on mixed-oxide-fuel meltdown in TREAT, is the first of the Mark-II loops to be equipped with a dump tank. A stress analysis has been performed to show that the loop design with dump-tank piping is acceptable from the standpoint of thermal stresses in both normal operation and in the event the loop rupture disk breaks, dumping hot sodium into the blowout line.

The analysis of the dump piping, comprised of the blowout line from loop proper to safety tank, safety tank, and the fill and overflow lines from tank to loop proper, results in a conservative estimate of the system stresses, since the model used was two-dimensional, while the actual loop is three-dimensional and more flexible. The smaller, 5-ft-long overflow tube was neglected, because of its high flexibility. Throughout the analysis, the rectangular valve bodies and their weldable port projections were considered to be essentially rigid, because of their massive geometry.

Two cases were considered for analysis. Case I corresponds to the steady-state pretransient operational condition of the Mark-II loop, with the blowout line maintained at 400°F, the mechanical valve and lower fill line at 125°F, and the burst disk intact. This distribution of temperature in the auxiliary loop is reasonable, because of the heavy thermal insulation covering the entire system, and of the thermal isolation of the mechanical valve, lower fill line, and safety tank from the hot loop by the liquid-cooled freeze plug.

Case II serves as a limiting calculation, with the blowout line at 900°F, and the temperatures of the remainder of the auxiliary loop unchanged.

In both cases, the highest stresses occur at the segment of the auxiliary loop containing the mechanical valve in the fill line. For the steady-state Case I, the maximum stress calculated was 9,407 psi at the fill-line valve, with a stress of 6,370 psi at the rear of the burst-disk housing, and a stress of 3,401 psi at the weldment of the fill line to the lower bend of the loop proper. None of these stresses is comparable to the yield strength of the stainless steel; hence, there would be no distortion in the system as a result of normal steady-state operation of the loop at temperature.

In Case II, the 900°F temperature of the blowout line corresponds to the limiting condition to be realized in the event that an overpressure ruptures the burst disk and discharges the molten sodium from the loop proper into the safety tank. The resultant stresses calculated were: 33,317 psi at the fill-line valve, 21,563 psi at the burst-disk housing, and 11,510 psi at the fill line-loop weldment.

Although these calculated stress values seem high, we believe that they are acceptable for safe operation of the Mark-II loop in experiments which might result in the overpressure rupture of the calibrated burst disk. The stresses realized in the auxiliary system are secondary stresses resulting from the thermal expansion of the blowout line during a thermal excursion, from 400°F to the temperature of the loop sodium. Since the valve releasing the sodium from the loop into the blowout line is a simple rupture disk, the excursion must be considered to be a single-time event; any analysis related to cyclic operation of the blowout line would be meaningless.

The ASME B & PV Code* for cases not requiring analysis for cyclic operation specifies that the limit of stress intensity for secondary stresses plus bending is to be defined as $3S_m$, where

$$\begin{aligned} S_m &= \frac{(S_m @ 400^\circ\text{F}) + (S_m @ 900^\circ\text{F})}{2} \\ &= \frac{19,400 + 14,000}{2} = 16,700 \text{ psi.} \end{aligned}$$

*ASME Boiler & Pressure Vessel Code, 1968 Ed., Section III "Nuclear Vessels," Article 4, Paragraphs N-412-i, N-412-m, N-414.4, and Figure N-414.

By this,

$$3S_m = 50,100 \text{ psi.}$$

The USAS B31.1.0 Power Piping Code* specifies that the allowable stress, S_A , for cyclic operation must not exceed

$$S_A = f(1.25S_c + 0.25S_h),$$

where

S_c = the allowable stress as tabulated at the minimum temperature (100°F);

S_h = the allowable stress at the maximum temperature (1000°F);

f = stress range reduction factor for cyclic operation ($f = 1$, for less than 7000 full temperature cycles).

This yields

$$\begin{aligned} S_A &= (1.25)(18,750) + (.25)(14,000) \\ &= 23,438 + 3500 = 27,000 \text{ psi.} \end{aligned}$$

Hence, the stress at the burst-disk housing ($\sigma_H = 21,563$ psi) is well below the limiting stresses allowed for thermal-expansion stresses and is far below the stress limit defined by the ASME Code

(ii) Shipping Cask. A revised set of vendor shop drawings has been received at Argonne and has been approved for submittal to the AEC, subject to incorporation of minor changes. These changes are being made simultaneously by the vendor and ANL so that no delay will result. The design analysis report is complete, and the ANL quality-assurance plan is under final review by the Procurement Services Division. The approval package consisting of the design analysis, vendor shop drawings, ANL drawings of parts fabricated by ANL, and the quality-assurance plan will be forwarded to the AEC for approval of cask procurement.

(iii) Thermal-neutron Shield for Mark-II Loop. A $1/v$ thermal-neutron-absorbing shield was fabricated as an inner liner for the outer containment can to the Mark-II TREAT loop. The lined outer containment can was provided as interchangeable hardware to be used both with the calibration and first two test loops for the mixed-oxide prototype fast reactor (PFR) pin tests (Series LI).

*USAS B31.1.0 Power Piping Code, 1967, Chapter II, Sections 102.3.2c and 119.6.4.

The shield was constructed by coating a substrate, consisting of a 16 mesh, 20-mil wire screen spot welded to the 25-mil stainless steel liner can, with a 50-50 mixture of B_6Si and Pyromark paint. Several coatings were applied. After the last coating, the surface was polished evenly down to the grid wires (which served both as a reference marker and a mechanical reinforcement for the B_6Si). The shield was then baked and coated with a protective surface layer of Pyromark paint.

Measurements of epithermal-neutron transmission, both on preliminary small samples as well as the completed shield, were used to determine the "effective B_6Si thickness" at an assumed density of 1.7 g/cm^3 (70% theoretical density). The small samples had an "effective B_6Si thickness" of 22.4 mils, while the completed liner had an "effective thickness" of 19 mils. Transport calculations indicated that such a Mark-II TREAT loop liner would yield a radial variation in sample power of $\pm 15\text{-}20\%$. The ratio of sample center-liner to maximum TREAT power density would be about 65 to 1. Measurements of thermal-neutron transmission indicated uniform surface coatings for the samples as well as for the completed shield.

A PFR pin, with enriched uranium surface foils welded to a concentric stainless steel tube in the sample holder, was provided for the calibration mockup. Analyses were performed to determine the in-pile thermal heating of the shield under various conservative assumptions. The heating from the n, α reaction is small in light of the high-temperature stabilities of the B_6Si and the Pyromark binder.

b. TREAT Operations (J. F. Boland)

Neutron radiographs were made of a group of EBR-II melt-wire assemblies and one EBR-II experimental subassembly.

The contractor has assembled the hydraulic control-rod-drive system on a test stand and is checking out the system. Delivery in January is still expected.

4. Materials Behavior and Energy Transfer

a. High-temperature Physical Properties (M. G. Chasanov)

Last Reported: ANL-7618, pp. 132-133 (Sept 1969).

(i) Total Pressure over Liquid UO_2 . An important input parameter for equation-of-state calculations for reactor fuels is vapor pressure of the fuel. Presently available data must be extrapolated over many orders of magnitude to obtain vapor-pressure values at the temperatures of interest in reactor-safety calculations. Consequently, a program was initiated (see Progress Report for June 1969, ANL-7581, p. 127) to

measure vapor pressures over liquid reactor fuels by means of transpiration techniques, so as to reduce the extent of the extrapolation. The data to be obtained will allow the calculations to be made with greater confidence.

A number of preliminary vapor-pressure measurements have been made with urania by means of the transpiration technique. These measurements have served to evaluate such factors as inert carrier-gas flow rates, choice of operating techniques, and hot-zone geometry, as well as the effect of the vaporization on sample stoichiometry. Two sets of measurements were made with solid urania, one at 2615°K, the other at 2860°K. From these preliminary measurements, the total pressures of uranium-bearing species obtained were 4.45×10^{-4} and 6.55×10^{-3} atm, respectively.

Work is presently under way to carry out test measurements over liquid urania at temperatures up to approximately 3525°K. The first of these preliminary measurements on the liquid, at 3175°K, gave a tentative value of 7.1×10^{-2} atm.

5. Violent Boiling (R. O. Ivins)

a. Mathematical Models of Fuel-Coolant Dynamics (D. R. Armstrong)

Last Reported: ANL-7632, p. 143 (Oct 1969).

(i) Fuel-failure Model (K. A. Varteressian and J. C. Hesson)

Not previously reported.

As part of the development of mathematical models for describing fuel-coolant interaction in accident situations, an analysis has been made of a hypothetical accident involving a sudden complete loss of coolant. This analysis is part of a broad study of accident situations involving the complete or partial loss of capabilities for cooling a reactor. In this analysis, a single fuel rod (unirradiated stainless steel-clad UO_2 -20% PuO_2 , helium bonded), cooled by sodium and operating at steady-state power, was subjected to a loss of coolant, and the time to cladding failure was determined. Two operating conditions were considered: (1) fuel power density of 304 cal/sec-cm^3 and sodium coolant at 400°C, and (2) power density of 696 cal/sec-cm^3 and sodium coolant at 645°C. It was assumed that the fuel rod would continue to operate at the same power after the accident, and that there was no heat loss from the rod. Radial temperature profiles across the fuel, gas gap, and cladding, in addition to gas pressure within the cladding, were calculated at various time increments after the loss of coolant.

The calculations for the first case showed that failure would occur ~2.2 sec after loss of coolant by virtue of loss of strength of the cladding. The cladding temperature at failure was ~1330°C; the yield strength of stainless steel at that temperature is not sufficient to sustain the internal gas pressure. The fuel-centerline temperature increased from ~1690 to ~1850°C.

In the second case, failure of the fuel rod occurred ~0.36 sec after loss of coolant by the same mechanism as in the first case; the cladding temperature at the moment of failure was ~1150°C.

The calculations show the principal cause of failure to be elevated cladding temperatures (and concomitant loss of strength). The internal gas pressure at failure was not much different from the steady-state value.

B. Effluent Control--Environmental Studies-- Research and Development

1. Thermal-Plume Transport in the Great Lakes (J. J. Roberts)

Not previously reported.

A computerized analytical procedure is being developed for predicting the dispersion characteristics, temperature field, and gross behavior of thermal plumes produced by a lakeshore power plant. The model will be based on a numerical solution to the fundamental equations governing the conservation of mass, momentum, and energy. The inputs required by the model are fundamental quantities, such as viscosity, vertical density profiles, and large-scale lake-current velocities.

A thermal plume passes through three distinct regimes of flow. In the "channel" or "jet" regime, inertial forces dominate and the jet core persists for some distance downstream, with little mixing with the cooler water that surrounds the jet; however, the jet flow is influenced by the lake bottom. In the "transition" regime, the plume is bent by lake currents and spreads rapidly due to buoyancy of the plume and to turbulent entrainment. The final "diffusion" regime is dominated by the mean lake current and the turbulent motions caused by wind and convection. Theoretical models with sufficient generality are not available, so considerable study and experimental calculation will be needed to develop a useful theoretical model.

Several numerical experiments are planned with two-dimensional forms of the Navier-Stokes and energy-conservation equations. The first study will approximate the horizontal motion of the plume in the jet phase as it enters the lake and is bent by a cross current. Figure IV.B.1 shows our first crude model of a thermal discharge into a crossflow current,

indicates the nomenclature employed in the mathematical description of flow in the plane of the discharge, and shows some of the simplified boundary conditions. The temperature is T , the x component of velocity is u , and the y component is v . A second calculation will study a vertical cross section of the plume as it enters the lake, separates from the bottom, and rises to form a warm surface layer (see Fig. IV.B.2). A third study will concern methods of handling the diffusion regime. Although these preliminary models will have simple boundary conditions, the results of the calculations will describe the essential features of a thermal plume, and should permit significant comparisons with experiments and earlier theories. These two-dimensional studies will provide experience needed to produce the required three-dimensional model with realistic topography.

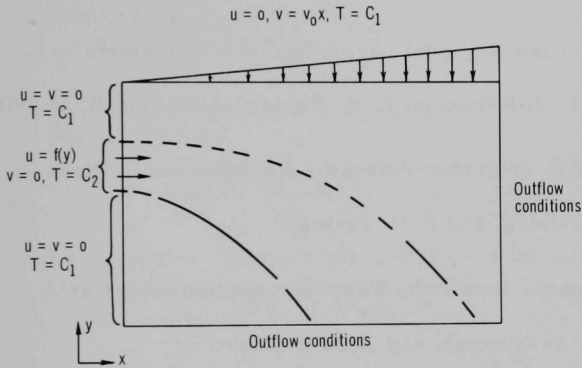


Fig. IV.B.1

Schematic for the x-y Numerical Model of the Jet and Transition Regimes.

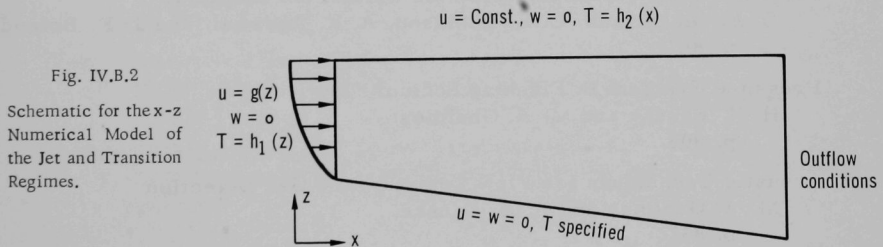


Fig. IV.B.2

Schematic for the x-z Numerical Model of the Jet and Transition Regimes.

a. Code and Evaluate x-z Models.

Coding of the two-dimensional horizontal model of the jet has begun. The first use of the code will be to study a laminar two-dimensional jet without cross flow. The numerical results will be compared with published laboratory experiments as well as with analytical expressions giving the velocity profile and spreading rate at large distances from the source.

PUBLICATIONS

The following appeared as Abstracts in Trans. Am. Nucl. Soc. 12(2)
(Nov 1969):

On the Analyses of the Fuel Meltdown Studies with TREAT

A. K. Agrawal
p. 865

Fuel-Failure Behavior during Transient Meltdown in the Sodium-Filled Piston Autoclave

J. J. Barghusen, D. R. Armstrong, J. F. Boland, R. W. Mouring,
and J. C. Hesson
p. 863

Behavior of Zircaloy-Clad UO_2 Fuel during Nuclear Transients in TREAT

J. J. Barghusen, L. J. Harrison, K. A. Varteressian, and R. O. Ivins
p. 862

Hydrodynamic Response of Primary Reactor Containment to High-Energy Excursions

Y. W. Chang, J. Gvildys, and S. H. Fistedis
p. 826

Preliminary Performance Data from Fast Neutron Hodoscope at TREAT

A. DeVolpi, C. E. Dickerman, and J. F. Boland
p. 868

First TREAT Loop Experiments on Oxide Fuel Meltdown

C. E. Dickerman, L. E. Robinson, A. K. Agrawal, and J. F. Boland
p. 867

Pressure Gradient in Flashing Sodium Flow

H. K. Fauske and M. A. Grolmes
p. 908

Acoustic Techniques for Flow Regime--and Gas Detection

M. A. Grolmes and H. K. Fauske
p. 832

Superheat Expulsion in Single and Multipin Channels--Simulation of Blocked Subassembly Voiding

M. A. Grolmes, H. K. Fauske, and G. A. Lambert
p. 907

Heat Removal and Containment Following Meltdown of an LMFBR Core

M. A. Grolmes, J. C. Hesson, R. O. Ivins, and J. F. Marchaterre
p. 864

The Use of Quasilinearization for the Solution of Nonlinear Space-Dependent Reactor Equations

L. J. Habegger and C. Hsu
p. 830

Experimental Study of Simulated Fission Gas Release in a Heated Channel

B. M. Hoglund, R. P. Anderson, and T. J. Marciniak
p. 901

Incipient Boiling Conditions in a Blocked LMFBR Subassembly

R. E. Holtz and R. M. Singer
p. 912

Hybrid Solution of Energy Equations in Porous Fuel

W. W. Marr and M. M. El Wakil*
p. 623

Transient Behavior of Pre-Irradiated "High-Swelling" EBR-II Driver Fuel in TREAT

A. B. Rothman, C. J. Renken, R. R. Stewart, G. G. Dewey,
D. R. Hutchinson, and C. E. Dickerman
p. 867

Fast Reactor Disassembly Calculation Utilizing a Temperature-Density-Dependent Equation of State

W. T. Sha and A. E. Waltar**
p. 825

A Compressible Model for Transient Sodium Boiling

E. R. Siegmann
p. 904

Vaporization and Expulsion Measurements with Superheated Sodium

R. M. Singer, R. E. Holtz, and H. R. Niemoth
p. 911

Sodium Bubble Collapse and Pressure Generation

T. G. Theofanous, H. S. Isbin,[†] and H. K. Fauske
p. 909

*The University of Wisconsin.

**Battelle Northwest Laboratory.

[†]University of Minnesota.

ARGONNE NATIONAL LAB WEST



3 4444 00008282 6

7

